

# A Geometry-Adapting Methodology for the Numerical Investigation on Flow-Driven Erosion Processes

Zur Erlangung des akademischen Grades eines  
DOKTORS DER INGENIEURWISSENSCHAFTEN (Dr.-Ing.)

von der KIT-Fakultät für Maschinenbau des  
Karlsruher Instituts für Technologie (KIT)  
angenommene

## **DISSERTATION**

von

**M. Sc. Moritz Schenk**

Tag der mündlichen Prüfung: 17.12.2021

Hauptreferent: Prof. Dr.-Ing. X. Cheng

Korreferent: Prof. Dr.-Ing. T. Schulenberg





# Declaration

Ich versichere wahrheitsgemäß, die Arbeit selbstständig angefertigt, alle benutzten Hilfsmittel vollständig und genau angegeben und alles kenntlich gemacht zu haben, was aus Arbeiten anderer unverändert oder mit Abänderungen entnommen wurde.

**Karlsruhe, January 12, 2022**

.....

**(Moritz Schenk)**



# Acknowledgements

An dieser Stelle möchte ich mich bei all jenen bedanken, die mich während meiner Arbeit fachlich und persönlich unterstützt haben.

Ich bedanke mich bei Herrn Prof. Dr.-Ing. Xu Cheng, der mir nicht nur die Möglichkeit gegeben hat, diese Arbeit zu schreiben, sondern auch für die hervorragende Betreuung und kollegialen Diskussionen während der Erstellung dieser Arbeit. Des Weiteren danke ich Herrn Prof. Dr.-Ing Thomas Schulenberg für die Übernahme des Zweitgutachtens und seine hilfreichen Diskussionsbeiträge, sowie Herrn Prof.Dr.-Ing Dieter-Heinz Hellmann von der KSB Stiftung, die meine wissenschaftlichen Tätigkeiten hier am KIT finanziert hat.

Auch bedanke ich mich bei allen früheren und jetzigen Kollegen des IATFs für ein angenehmes Arbeitsklima, eine stets freundliche Zusammenarbeit, fruchtbare Diskussionen und schöne Erlebnisse. Herausstellen möchte ich dabei besonders Fabian Wiltschko für seine hilfreichen fachlichen Diskussionen und seine Unterstützung. Auch bei Ludwig Köckert, als langjähriger Bürokollege, möchte ich mich gesondert bedanken.

Ein Weiterer Dank gebührt Annemarie Schmidt und Markus Hanke für das kritische Korrekturlesen dieser Arbeit. Des Weiteren half mir Markus auch bei der Umsetzung des 3D-Drucks.

Abschließend möchte ich mich bei meiner Familie und insbesondere bei meiner Mutter bedanken, die mir das Studium ermöglicht und die mich mit ihrer Erziehung zu einem wissbegierigen Menschen gemacht hat.



# Abstract

Erosion can cause failures in piping systems and equipment in all types of facilities, often in fossil or nuclear power plants. These kinds of failures are a dangerous hazard, and additionally, they are an unwanted and unplanned interruption of an operating system. Reducing the risk for everyone involved and, at the same time, reducing the maintenance time, is a typical engineering task. Therefore, reliable tools for predicting erosion locations and their magnitude are necessary to achieve the engineering target.

In this work, a methodology is presented and tested which aim is to predict and model flow-driven erosion processes over time. The prediction over time happens in an iterative workflow, where the geometry is adjusted at each time step in accordance with the simulated erosion rate. Hence, erosion over time can be simulated, and possible self-reinforcing or dilution processes, due to a geometry change, can be investigated. The erosion processes in question are particle erosion and Flow Accelerated Corrosion (FAC). FAC was investigated in water systems but also heavy liquid metals. These fluids are promising working fluids because of their high heat conduction capacity, feasibility for high temperatures at atmospheric pressure, and their favorable neutron physics in the nuclear field, but they have a high erosion potential.

With the proposed methodology, the modeling of the FAC is able to predict the magnitude and the location of the highest wall loss to a satisfactory degree. Possible reasons for differences of the predicted and measured distribution of the wall loss are discussed.

The heavy liquid metal investigation gave good predictions of the wall loss by using the proposed methodology. It overpredicted the measured wall loss by a factor of only 1.4, whereas prediction from the literature overpredicted the wall loss by a factor of 2.4.

Additionally to the FAC investigation in piping systems, this work also studies FAC minimization in pump impellers. A numerical pump investigation set-up was established and validated. As working fluids, water and the heavy liquid metal lead-bismuth eutectic (LBE) were compared. The Wall Shear Stress (WSS) was taken as an indicator for enhanced FAC. Compared to water, the calculated WSS distribution was shifted by a factor of ten in LBE. The influence of different geometry parameters on the WSS distribution was also discussed. The parameters in question were the number of impeller blades and the outlet angle of the impeller blade. It could be shown that for higher outlet angles and fewer blades,

the averaged WSS of a single blade could be reduced significantly. This change of the geometry has to be done carefully because both arrangements lead to a flatter pump characteristic. Impellers with flatter characteristic curves have often problems of recirculations near the design points. Recirculation phenomena were investigated with the given numerical set-up.

Particle erosion was also investigated in a 90° elbow geometry with the proposed methodology. In contrast to the FAC investigations, where the overall erosion is diluted by itself over time, a self-reinforcing process could be depicted. In the geometry adapting process, a pocket is formed at the location of the highest erosion. With this pocket, the magnitude of the erosion rate was predicted accurately in comparison to the measured erosion rate.

# Kurzfassung

Erosion kann zum Versagen von Rohrleitungen und anderen Apparaturen in verschiedenen Anlagen wie Kraftwerken, nuklear oder fossil, führen. Diese Art von Unfällen sind gefährliche Zwischenfälle und zusätzlich ungeplante und ungewollte Unterbrechungen des Betriebes der betroffenen Anlagen. Eine typische Ingenieuraufgabe ist, das davon ausgehende Gefahrenpotential zu minimieren und gleichzeitig die Wartungszeit zu reduzieren. Aus diesem Grund sind zuverlässige Hilfsmittel für die Vorhersage von Erosionsarten und die Größenordnung der auftretenden Erosion notwendig.

In dieser Arbeit wird eine Methode vorgestellt und getestet, deren Ziel es ist, strömungsbedingte Erosionsphänomene über die Zeit vorherzusehen und zu modellieren. Der zeitliche Verlauf der Vorhersage erfolgt über einen iterativen Prozess. In jedem Iterationsschritt wird die Geometrie der berechneten Erosion gemäß neu angepasst. Dadurch wird der zeitliche Verlauf der Erosion modelliert und mögliche selbstverstärkende Effekte oder sich abschwächende Effekte können damit untersucht werden. Die in Frage kommenden Erosionsphänomene sind Partikel Erosion (Abrasion) und Flow Accelerated Corrosion (FAC).

FAC wurde mit Wasser und flüssigen Schwermetallen modelliert und untersucht. Flüssige Schwermetalle sind aufgrund ihrer hohen Wärmeleitfähigkeit, hohen möglichen Einsatztemperaturen bei Atmosphärendruck und ihrer vorteilhaften Neutronenphysik bei Kernkraftanwendungen vielversprechende Arbeitsfluide der Zukunft. Nachteilig ist jedoch das hohe Erosionspotential. Mit der vorgeschlagenen Methode kann die Größenordnung der FAC-Rate und der Ort der höchsten Erosionsrate zu einem zufriedenstellenden Maß bestimmt werden. Mögliche Abweichungen zwischen modellierten Ergebnissen und gemessenen Verteilungen werden diskutiert.

Die Schwermetalluntersuchungen mit der vorgeschlagenen Methode ergaben gute Übereinstimmungen bei der Vorhersage des Wandverlustes. Die vorgeschlagene Methode überschätzt den gemessenen Wandverlust um den Faktor 1,4, wohingegen die Vorhersage aus der Literatur den Wandverlust um einen Faktor 2,4 überschätzt.

Zusätzlich zu den FAC Untersuchungen in Rohrsystemen untersucht diese Arbeit noch die FAC Minimierung im Flügelrad von Kreiselpumpen. Eine numerische Pumpenuntersuchung wurde vorgestellt und validiert. Als Arbeitsfluide wurden

Wasser und Blei-Bismut-Eutektikum (LBE) verglichen. Die Wandschubspannung (WSS) wurde als Indikator für eine verstärkte FAC verwendet. Verglichen mit Wasser ist die berechnete WSS-Verteilung um einen Faktor zehn höher als bei LBE. Der Einfluss verschiedener geometrischer Faktoren wurde ebenfalls diskutiert. Die geometrischen Faktoren sind Schaufelanzahl und Austrittswinkel der Schaufel. Es kann gezeigt werden, dass für höhere Austrittswinkel und weniger Schaufeln die durchschnittlich wirkende WSS auf eine einzelne Schaufel signifikant reduziert wird. Die Änderung der Geometrie führt jedoch gleichzeitig zu einer flacheren Pumpencharakteristik. Flügelräder mit flacheren charakteristischen Kurven haben häufig Probleme mit Rezirkulationen nahe am Auslegungspunkt. Rezirkulationen können ebenfalls mit den numerischen Untersuchungen beobachtet werden.

Abrasion wurde in einer 90° Rohrkrümmergeometrie mit der entwickelnden Methode untersucht. Im Gegensatz zu den FAC Untersuchungen, bei denen die Gesamterosion mit der Zeit abgeschwächt wurde, konnte hier ein sich selbstverstärkender Effekt beobachtet werden. Eine Tasche bildet sich am Ort der höchsten Erosion im Zuge der Geometrieanpassung aus. Mit dieser Tasche kann die Größenordnung der Erosionsrate in guter Übereinstimmung mit der gemessenen Erosionsrate berechnet werden.



# Contents

<b>Declaration</b>	<b>iii</b>
<b>Acknowledgements</b>	<b>v</b>
<b>Abstract</b>	<b>vii</b>
<b>Kurzfassung</b>	<b>ix</b>
<b>List of Abbreviations</b>	<b>xv</b>
<b>List of Symbols</b>	<b>xvii</b>
<b>1 Introduction</b>	<b>1</b>
1.1 Scientific Motivation . . . . .	1
1.2 Objective . . . . .	3
1.3 Structure of the Thesis . . . . .	4
<b>2 Fundamentals</b>	<b>7</b>
2.1 Erosion . . . . .	7
2.1.1 Mass Transfer Coefficient . . . . .	10
2.1.2 Concentration of the Eroded Material . . . . .	11
2.2 Liquid Metals . . . . .	15
2.2.1 Requirements for Heat Transfer Fluids and resulting LM and their properties . . . . .	15
2.2.2 LBE and Lead . . . . .	18
2.2.3 Erosion in LBE . . . . .	21
2.3 Basic Knowledge of Centrifugal Pumps . . . . .	22
2.3.1 Principles . . . . .	22
2.3.2 Performance Characteristics . . . . .	23
2.3.3 Specific Speed . . . . .	24
2.4 Previous and Related Work . . . . .	25
2.4.1 Overview of Numerical Investigations of FAC . . . . .	26
2.4.2 Overview of Numerical Investigations of Abrasion . . . . .	34
2.4.3 Heavy Liquid Metal Erosion . . . . .	36
2.4.4 Centrifugal Pumps with Liquid Metal as a Working Fluid . . . . .	38

<b>3</b>	<b>General Strategy for a Trustworthy CFD Simulation</b>	<b>41</b>
3.1	Computational Model . . . . .	41
3.1.1	Particle Calculation . . . . .	42
3.1.2	Pump Calculation . . . . .	43
3.2	CFD Simulations in Pipes . . . . .	44
3.2.1	Preconditioning . . . . .	44
3.2.2	Mesh Sensitivity Study . . . . .	44
3.3	Erosion in Pumps . . . . .	49
<b>4</b>	<b>Erosion Modeling in a Mesh Adapting Framework</b>	<b>51</b>
4.1	Description of the Method . . . . .	51
4.1.1	CFD Calculation as Initial Step . . . . .	51
4.1.2	Erosion calculation . . . . .	52
4.1.3	Mesh Deformation . . . . .	53
4.1.4	Time Iteration . . . . .	57
<b>5</b>	<b>Application of the Method and Its Validation</b>	<b>59</b>
5.1	Flow Accelerated Corrosion in a 58° Elbow . . . . .	59
5.1.1	Summary of the Experiment . . . . .	59
5.1.2	CFD Calculations and Modelling of the Erosion . . . . .	60
5.1.3	Comparison of the Experiment with the CFD Modelling . . . . .	66
5.2	Flow Accelerated Corrosion Erosion in Heavy Liquid Metals . . . . .	71
5.3	Particle erosion in a 90° Elbow . . . . .	75
5.3.1	Summary of the Experiment . . . . .	75
5.3.2	CFD Calculations and Modelling of the Erosion . . . . .	76
5.3.3	Comparison of the Experiment with the CFD Modelling . . . . .	79
<b>6</b>	<b>Pump Investigation in Regards of Erosion Minimization</b>	<b>81</b>
6.1	Pump Characteristic . . . . .	81
6.2	Validation of the Numerical Method . . . . .	83
6.3	Geometry Design . . . . .	84
6.3.1	Verification of the Geometry Design . . . . .	86
6.4	Recirculation at Off-Design Flow Rates . . . . .	88
6.5	Influence of the Kinematic Viscosity on the Pump Parameters . . . . .	88
6.6	Impeller Performance with Different Blade Number and/or Outlet Angle . . . . .	92
6.7	Influence on the Wall Shear Stress . . . . .	92
6.7.1	Fluid Properties . . . . .	94
6.7.2	Influence of the Blade Number on the Wall Shear Stress . . . . .	94
6.7.3	Influence of the Outlet Angle on Wall Shear Stress . . . . .	96
<b>7</b>	<b>Conclusion and Outlook</b>	<b>99</b>
7.1	Conclusion . . . . .	99
7.1.1	Flow Accelerated Corrosion . . . . .	99
7.1.2	Particle erosion . . . . .	101
7.1.3	Pump Investigation . . . . .	101
7.2	Outlook . . . . .	103

**Bibliography**

**105**



# List of Abbreviations

ALFRED	Advanced Lead Fast Reactor European Demonstrator
CANDU	CANada Deuterium Uranium
CFD	Computational Fluid Dynamics
EFPY	Effective Full Power Year
FAC	Flow Accelerated Corrosion
HLM	Heavy Liquid Metal
LBE	Lead-bismuth eutectic
LFR	Lead cooled Fast Reactor
LM	Liquid Metal
MRF	Multiple Reference Method
MTC	Mass transfer coefficient
RANS	Reynolds averaged Navier Stokes
SIMPLE	Semi Implicit Method for Pressure Linked Equation
SST	Shear Stress Transport model (k- $\omega$ -SST)
USNRC	The United States Nuclear Regulatory Commission Office of Inspection and Enforcement
WSS	Wall Shear Stress



# List of Symbols

Sign	Description	Unit
A	Area	m <sup>2</sup>
c	absolute velocity	m/s
C <sub>b</sub>	concentration in the bulk	kg/m <sup>3</sup>
C <sub>D</sub>	drag coefficient	-
C <sub>e</sub>	concentration at equilibrium	kg/m <sup>3</sup>
c <sub>p</sub>	heat capacity	$\frac{\text{kJ}}{\text{kg}\cdot\text{K}}$
C <sub>w</sub>	concentration at the wall	kg/m <sup>3</sup>
D	diffusion coefficient	m/s
D <sub>i</sub>	inner diameter	mm
D <sub>o</sub>	outer diameter	mm
R <sub>b</sub>	bend radius	mm
E	erosion	$\frac{\text{kg}(\text{ConstructionMaterial})}{\text{kg}(\text{Particle})}$
e <sub>n</sub>	restitution coefficients normal to the wall	-
e <sub>t</sub>	restitution coefficients tangential to the wall	-
F	Force	N
f	fraction of iron which is oxidized or Fanning factor	-
g	acceleration due to gravity	$\frac{\text{m}}{\text{s}^2}$
H	pump head	m

<b>Sign</b>	<b>Description</b>	<b>Unit</b>
$H_{opt}$	pump head at the design point	m
K	equilibrium constant	depends
$k_B$	Boltzmann's constant	J/K
$K_d$	Time dependent part of the MTC	m/s
$K_g$	geometric factor of the MTC	-
$K_r$	Reaction rate	m/s
L	characteristic length	m
$L_H$	hydrodynamic developing length	m
M	molecular weight	g/mol
m	mass	kg
$\dot{m}$	mass flow	kg/s
MTC	mass transfer coefficient	$\frac{m}{s}$
n	rotational speed	$\frac{1}{min}$
$n_q$	specific speed	$\frac{1}{min}$
Nu	Nusselt number	-
P	Power	W
p	static pressure	Pa
$\phi$	association factor	-
$p_p$	pressure on the pressure side	Pa
$P_Q$	pump output power	W
Pr	Prandtl number	-
$p_s$	pressure on the suction side	Pa
$p_{sat}$	saturation pressure	Pa
$P_t$	total pressure divided by density	$m^2/s^2$
Q	volume flow	$\frac{m^3}{s}$
$Q_{opt}$	volume flow at the design point	$\frac{m^3}{s}$
R	universal gas constant	$\frac{J}{molK}$



Sign	Description	Unit
$r$	radius or volume fraction	m or -
$R_C$	corrosion rate	$\frac{\text{kg}}{\text{m}^2 \cdot \text{s}}$
Re	Reynolds number	-
$R_0$	Stoke radius	m
s	stretch factor	-
Sc	Schmidt number	-
Sh	Sherwood number	-
T	temperature	K or °C
t	time	s
u	velocity	m/s
$u^+$	dimensionless velocity	-
$u_p$	velocity on the pressure side	$\frac{\text{m}}{\text{s}}$
$u_s$	velocity on the suction side	$\frac{\text{m}}{\text{s}}$
$u_\tau$	friction velocity	m/s
$\vec{U}$	Velocity vector for the directions in space	m/s
V	molecular volume	$\text{cm}^3/\text{mol}$
x	location	m
y	distance to the nearest wall	m
$y^+$	dimensionless wall distance	-
$z_p$	height coordinate on the pressure side	m
$z_s$	height coordinate on the suction side	m
$\delta$	Thickness of the oxidation layer	m
$\varepsilon$	Surface roughness	m
$\eta$	efficiency	-
$\lambda$	thermal conductivity	$\frac{\text{W}}{\text{m} \cdot \text{K}}$

<b>Sign</b>	<b>Description</b>	<b>Unit</b>
$\mu$	dynamic viscosity	Pa · s
$\nu$	kinematic viscosity	$\frac{\text{m}^2}{\text{s}}$
$\omega$	angular rotor velocity	1/s
$\rho$	density	$\frac{\text{kg}}{\text{m}^3}$
$\tau_w$	wall shear stress	N/m
$\theta$	Porosity of the oxide layer	-
$\theta$	particle impact angle	°
$\zeta$	Hydraulic resistance coefficient	-

# 1. Introduction

*"On Tuesday, December 9, 1986, at 2:20 p.m., both units at the Surry Power Station were operating at full power when the 18-inch suction line to the main feedwater pump A for Unit 2 failed catastrophically. Eight workers who were replacing thermal insulation on a nearby line were burned by flashing feedwater. All were transported to area hospitals. Two workers were treated and released. Four other workers subsequently died."*

This abstract from Jordan (1986) describes an outcome of an accident in a nuclear power plant caused by erosion. The erosion led to a drastic and unexpected wall thinning. The piping system was not able to withstand the hydrodynamic forces anymore and broke. To avoid these kinds of accidents, efforts were made in the last decades to understand the different wall thinning mechanisms. The investigations in this field can have different approaches. One approach is to reduce erosion from the beginning by optimizing the flow conditions, for example. Another approach is to understand and describe the involved mechanism, so the wall thinning can be predicted in advance and countermeasures can be taken.

Today, the most widely used technique for erosion control is the ultrasonic measurement. There, ultrasonic sound is used to measure the pipe thickness. The testing takes time and not all locations are accessible (Prasad et al., 2018). Hence, it is an advantage to know in advance where the erosion happens and to which extent to reduce the usage of the ultrasonic measurement.

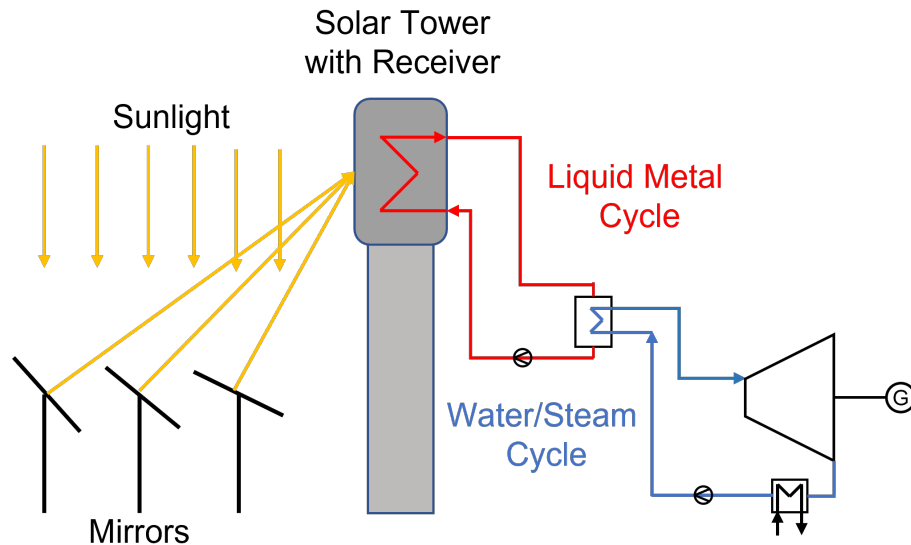
## 1.1 Scientific Motivation

Unwanted wall thinning caused many failures in piping systems and equipment in all types of facilities, often in power plants, fossil or nuclear (Kain, 2014). Not all end tragically like the described incident above, but the sudden release of high temperature steam or water is a dangerous hazard, and additionally, it is at least an unwanted and unplanned interruption of an operating system. Reducing the risk for everyone involved, and, at the same time, reducing the maintenance time is a typical engineering task. Therefore, reliable tools for predicting wall thinning locations and their magnitude are necessary to reduce the maintenance time of a facility. The aim of this work is to develop such a tool for different

kinds of erosion mechanisms. This work focuses on two types of flow-driven wall thinning mechanisms: the Flow Accelerated Corrosion (FAC) and particle erosion. Particle erosion is a pure mechanistic process: particles are carried with the stream and impinge on the wall due to sudden changes of the flow direction. The impingement leads to the degeneration of the wall at this location. To know the location and the magnitude of the erosion is the first step to find countermeasures to reduce the damage caused by the particles. The most obvious way to reduce the damage caused by the particles is to minimize the number of particles in the stream. Sources of particles could be other erosion mechanisms or pipelines, where the fluids are already contaminated with sand or other solid particles. For other applications, for example slurry pumps, the particle transportation is part of the application and for these cases it is useful to know where and to which grade the erosion happens.

FAC is the other flow driven wall thinning mechanism examined in this work. It is an interaction between hydrodynamic and chemical phenomena: the flow causes an accelerated dissolving of the construction material due to the carrying away of the corrosion products by the flow. Therefore, FAC could be minimized by reducing the flow velocity, but not in all applications the velocity can always be reduced to the necessary degree. For example, centrifugal pumps are used to raise a specific volume flow to a certain pressure level. The needed energy is transferred from the pump to the fluid by hydrodynamic processes. In this process, the fluid needs to be accelerated and hence, pumps are vulnerable to FAC. Flow velocity, Wall Shear Stress (WSS) and FAC are closely linked to each other (Kain, Roychowdhury, Mathew, et al., 2008). In cases, where reducing the velocity is not an option, optimizing the flow to the effect that the WSS is minimized, is crucial. Therefore, a numerical parameter study was done in this work in regards to minimizing the WSS in pump impellers that use Heavy Liquid Metals (HLMs) as a working fluid.

Liquid Metals (LMs) could become a new category of working fluids in the near future. These fluids are interesting for several applications because of their high thermal conductivity and their tolerance for high temperatures at atmospheric pressure (Pacio et al., 2013). HLMs, namely lead and lead-bismuth eutectic (LBE), are LMs, which could be used for example as heat transfer fluids in nuclear applications and in concentrated solar power plants. The Generation IV International Forum was founded in 2001 by a group of nations with the aim to develop the next generation of nuclear power plants (Generation IV). One of the proposed reactors is the so called Lead cooled Fast Reactor (LFR). As the name already suggest, it is a reactor cooled by lead or LBE, and has a fast-neutron spectrum. It operates at low-pressure, has good thermodynamic properties, and lead or LBE is relatively inert in regards to reactions with air or water (U.S. Nuclear Energy Research Advisory Committee (NERAC) and the Generation IV International Forum (GIF), 2002). These advantages make the LFR an interesting HLM application. Besides the favorable neutron physics, the advantages of these fluids could be also useful in concentrated solar power plants. An oversimplified scheme of the concentrated solar power plant is shown in Figure 1.1. In these power plants, the sunlight is concentrated on a central receiver by a field of mirrors. In the first cycle, fluids, which can withstand high temperatures and have a high thermal conductivity, are

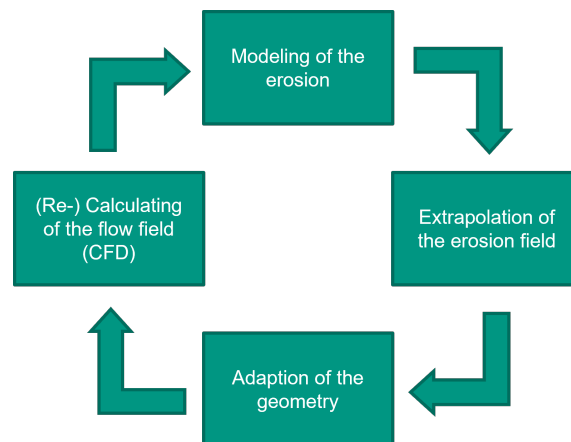


**Figure 1.1:** Scheme of a concentrated solar power plant based on Fritsch et al. (2015).

needed. Due to that, recent research focuses on HLMs as candidates for this first cycle (Pacio et al., 2013). If lead or LBE is used in the liquid metal cycle, temperatures of more than 900 °C could be reached under atmospheric pressure. The shown scheme is without any heat storage system. In Fritsch et al. (2015) more detailed concentrated solar power plant concepts can be seen. Besides the described positive aspects of HLMs in these applications, the high erosion potential is a disadvantage of HLM. To use these fluids safely in the new upcoming technologies, like the LFR or concentrated solar power plants, the erosion behavior has to be studied to avoid accidents like the one described at the beginning. Furthermore, the flow has to be optimized in the different applications like pump impellers in a way that FAC is minimized.

## 1.2 Objective

The aim of this thesis is to develop a method for modeling the so called FAC and particle erosion. The two erosion processes are defined by flowing fluids. Hence, Computational Fluid Dynamics (CFD) can be used as a powerful tool for investigating these kinds of phenomena. It is already confirmed by former studies that CFD is able to predict reliably the regions where erosion happens, and empirical correlations made for simple geometries are able to predict the magnitude of erosion. The idea is that by combining the empirical and the numerical approach in this thesis, a workflow can be established, which is able to investigate the erosion progression over time in a less time-consuming way than in experiments and also in more complicated geometries. A simplified version of the workflow can be seen in Figure 1.2. The main idea is that the flow field is calculated with CFD methods. These numerical results provide knowledge of local quantities like WSS distribution or impingement distribution of particles. With the help of these distributions, local erosion rate predictions can be made with empirical correlations. The local erosion



**Figure 1.2:** Simplified schematic of the workflow

rate can then be used to extrapolate the change of the geometry. By using this method iteratively, erosion could be modeled over time. Also dislocations of erosion hot spots induced by the change of the geometry and hence, a change of the flow field, could be found. This workflow is kept generic and modular; therefore, a lot of different cases can be investigated. Only the suitable modules have to be chosen for a given task, and the task can be effectively investigated. For FAC, the calculated WSS has to be combined with a correlation which predicts the wall loss as a function of the shear stress. For a particle erosion case, the particle distribution has to be coupled with the matching erosion model, and, if cases with liquid metals are of interest, the modules can also be adapted. Also more complicated geometries, like pump impellers, could be investigated.

### 1.3 Structure of the Thesis

This section gives an overview of the structure of the thesis, so the general approach becomes clearer. The first part of the thesis deals with the fundamentals of the erosion mechanisms, especially with the so called FAC in water and heavy liquid metals, and particle erosion. This should help the reader to better understand the line of reasoning of this thesis. Due to this reason, there is also a short summary chapter for fundamental terms of centrifugal pumps, so the centrifugal pump chapter later in the thesis is easier to follow. The first part of the thesis ends with an overview of the related work. There, works from other researchers, which have related approaches, are sorted and summarized. From this gathered information, the own approach is abstracted: An iterative process, where the modelled erosion is adapted to the calculation domain. With this approach, the calculation domain is changed according to the erosion, and the erosion over time can be monitored. To reduce repetitions, one chapter is dedicated solely to CFD calculations and how they were done in this thesis. Out of the same reason, the following chapter describes the proposed methodology step by step, so later chapters can refer to these chapters. After the detailed description of the methodology, the next chapter covers the application of the methodology for different erosion types, geometries, and fluids. In this chapter, the results of the erosion prediction are also

discussed and compared to experimental measurements. Then, the thesis deals with a possible future application of the methodology: an investigation of pump impellers in regard to FAC minimization in heavy liquid metal pumps. A parameter study is conducted for different geometry specifications. The aim of the study is to investigate the relationship between the examined parameters, the performance of the impeller, and the WSS distribution, the main driving force of FAC. The pump chapter is already an outlook of the future research work as a possible application of the introduced methodology. The last part of the thesis is the summary and other possible outlooks of the given research work.





## 2. Fundamentals

This chapter covers all the fundamentals which are important and necessary for a better understanding of this work. It is split into four main parts: an erosion part where the fundamentals of different kind of erosions are discussed, a Liquid Metal (LM) part with the focus on Heavy Liquid Metal (HLM), where the properties of these working fluids are discussed as well as their challenges, a centrifugal pump part, and a part which deals with an overview of related research work.

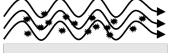

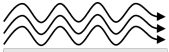
### 2.1 Erosion

In general, erosion is a degenerative process and means that something is worn away gradually. Erosion as a term is used in many different fields, but in an engineering background it is used to describe the loss of structural material or loss of wall thickness. It would be advantageous for engineers to predict this loss of material; therefore, modeling this process is of great interest. Erosion includes many different sub-processes with partly different physical and chemical mechanisms. To model this phenomenon, it is critical to know the process and the set of parameters which influence it (Levy, 1995).

Normally, erosion is a tribological stress for structural material and can be divided in three different categories (Sommer et al., 2010):

- **Erosion with abrasive particles** is characterized by the high mobility of the abrasive particles. It can be observed, for example, in dry mixing processes, gas streams, or in liquid flows with solid particles.
- **Erosion without abrasive particles** can happen, for example, from cavitation near the wall - the collapsing bubbles form micro jets that damage the surface. Another example are droplets in turbines under wet steam conditions which impinge the blades.
- **Erosion corrosion (with and without solid particles)** happens in the presence of a liquid medium. Additionally to the mechanical wear, an overlapping corrosive process takes place because of the electrochemical potential. The mechanical stress wears away the corroded protective layer.

**Table 2.1:** Selected types of wear sorted by the tribological stress according to Gesellschaft für Tribologie e.V. (2002) and Sommer et al. (2010). Only the Types which involve a liquid phase are shown.

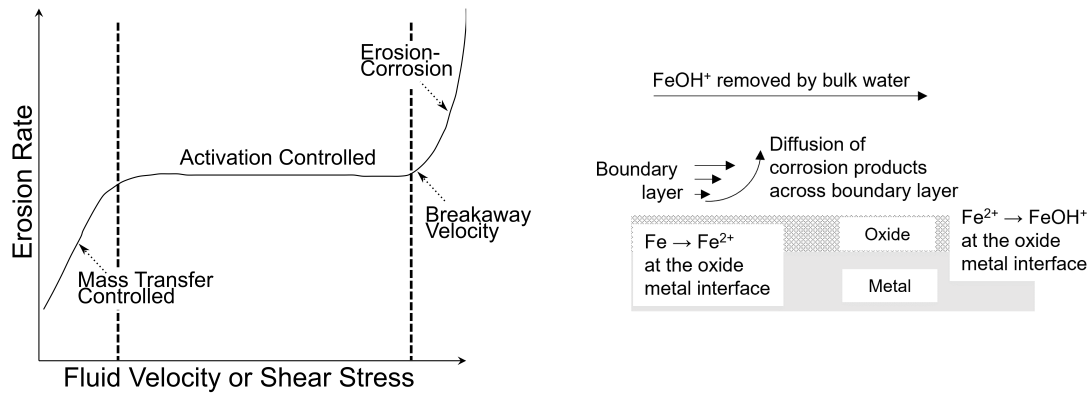
Symbol	Type of Wear	Example	Main mechanism
 Surface	Particle Erosion	Pumps, pipes	Abrasion, surface scratch
 Surface	Cavitation	Pumps, turbines, valve	Surface pitting
 Surface	Erosion Corrosion	Pumps, pipes, valves	Chemical reaction

An overview of the different processes and effective mechanisms can be seen in Table 2.1.

Additionally to this tribological dominated erosion processes, there is Flow Accelerated Corrosion (FAC), which is a process mainly dominated by a corrosion event. It results from chemical dissolution and mass transfer (Kain, 2014). Although erosion-corrosion, and FAC are dominated by two different mechanisms, which are linked to each other by the velocity of the fluid respectively by the Wall Shear Stress (WSS), the connection can be seen in Figure 2.1a: In the section with the lowest velocities, the loss of material is mainly mass transfer controlled. This means that, at the interface of solid to liquid, the dissolution is at its equilibrium. In that case, the diffusion flux of the dissolved species from the phase interface to the bulk is limiting the mass transfer rate and thereby the corrosion rate. The sublayer thickness is reliant on hydrodynamic parameters like geometry and fluid velocity. Hence, the corrosion rate increases with the velocity of the fluid. In contrast to mass transfer controlled section, the activation controlled section is independent of velocity. In this section, the dissolution reaction itself becomes the limiting factor. The rate of charge transfer at the metal surface is much slower than the mass transfer. This behavior is then called activation controlled. The mass transfer controlled and activation controlled section are both controlled in general by the chemical reactions and not by tribological effects. These sections are called FAC. At a critical velocity, the region of erosion-corrosion starts. In this region, the shear stress itself becomes high enough to strip the protective film from the surface (Balbaud-Célérier and Barbier, 2001; Chen et al., 1992). In technical applications, low corrosion rates are desired. Hence, activation controlled and especially erosion-corrosion should be avoided, and the flow velocity should be in the range of mass transfer controlled FAC.

The general mechanism for FAC in an aqueous environment can be seen in Figure 2.1b. Several chemical reactions and processes are involved in the FAC process (Kain, 2014) (Fujiwara et al., 2011):

- $\text{Fe} \longrightarrow \text{Fe}^{2+}$ : As shown in 2.1b, the reaction from elemental iron to an



(a) Erosion rate dependency on the fluid velocity and WSS, respectively (according to Chen et al. (1992)). (b) Schematic of the FAC process (according to Kain (2014)).

**Figure 2.1:** FAC and erosion-corrosion (left) and schematic of the FAC process (right).

$Fe^{2+}$ -Ion takes place at the interface of metal and oxide

- Then the  $Fe^{2+}$ -Ion has to diffuse through the layer to the phase boundary of oxide/water
- $Fe^{2+} + bH_2O \longrightarrow (Fe(OH)_b)^{(2-b)+}_{aq} + bH^+$ . At the phase interface the ion is dissolved in water ( $b=1,2$  or  $3$ ).
- This dissolved Iron(II)hydroxide diffuses through the boundary layer to the bulk flow and is carried away
- $(Fe(OH)_2)_{aq} \longrightarrow (Fe_2O_3)_s$  In the bulk, it can form solid particles of Iron(III)oxide

In the mass transfer region, the corrosion rate is governed by the concentration gradient and the mass transfer coefficient:

$$R_C = MTC (C_w - C_B) \quad (2.1)$$

where MTC is the mass transfer coefficient,  $C_w$  and  $C_b$  are the concentrations of the diffusive species at the wall and at in the bulk, respectively, and  $R_C$  is the resulting corrosion rate. The MTC is inversely dependent on the thickness of the boundary layer. A reduction of the boundary layer thickness caused by an increase of the fluid velocity (increase of the WSS) or an enhancement of local turbulence leads to an increase of the corrosion rate  $R_C$  (Kain, Roychowdhury, Ahmedabadi, et al., 2011).

The FAC rate is dependent on different parameters, like the chemistry of the working fluid, (e.g. pH value), temperature, and the used structural material (Kang et al., 2008) (Kain, Roychowdhury, Mathew, et al., 2008). These mentioned parameters uniformly affect the whole facility or at least large parts of it. Hydrodynamic factors, instead, are not uniformly distributed and therefore are responsible for local effects, i.e., for local wall thinning. Out of this reason, the hydrodynamic parameters, such as flow rate and wall shear stress, which is strongly dependent on the velocity

gradient normal to the wall, are mainly influencing local wall thinning processes because of their direct link to the mass transfer coefficient (MTC) (Kang et al., 2008).

### 2.1.1 Mass Transfer Coefficient

The MTC is a quantity for the convective mass transfer of a species in m/s. The Sherwood number  $Sh$  is the relation of the convective mass transfer to the pure diffusive mass transfer

$$Sh = \frac{MTC L}{D} \quad (2.2)$$

where  $L$  is the characteristic length and  $D$  the diffusion coefficient. The correlation for the Sherwood number is often expressed with the Reynolds number and Schmidt number:

$$Sh = a Re^b Sc^c \quad (2.3)$$

$a$ ,  $b$ , and  $c$  are identified experimentally. Reynolds number is defined

$$Re = \frac{uL}{\nu} \quad (2.4)$$

and Schmidt number

$$Sc = \frac{\nu}{D}. \quad (2.5)$$

$u$  is the mean velocity of the fluid and  $\nu$  the kinematic viscosity of the fluid. The disadvantage of the correlation 2.3 to estimate the MTC is that it does not take local effects into account. Hence, this equation is mainly suitable for straight pipes without any local change of the MTC. A more suitable correlation, which takes local effects into account, is the Chilton-Colburn equation. This equation is based on the Chilton-Colburn analogy which is a modified version of the Reynolds analogy:

$$Re \frac{f}{2} = Nu = Sh \quad (2.6)$$

where  $f$  is the Fanning factor,  $Nu$  the Nusselt Number, and  $Sh$  the Sherwood number. The Chilton Colburn analogy extends this relation to fluids with Schmidt and Prandtl numbers unequal to one. The Chilton-Colburn analogy can be used for fully developed turbulent flows. For heat transfer problems it can be used in a range of  $0.6 < Pr < 60$  and for mass transfer problems in a range of  $0.6 < Sc < 3000$  (Hewitt et al., 1994):

$$\frac{f}{2} = \frac{Sh}{Re Sc^{\frac{1}{3}}} = \frac{Nu}{Re Pr^{\frac{1}{3}}} \quad (2.7)$$

With this relation and a expression for the WSS:

$$\tau = \frac{f}{2} u^2 \rho \quad (2.8)$$

where  $u$  is the bulk velocity and  $\rho$  the density of the fluid, an equation for the MTC can be derived (Chilton et al., 1934):

$$MTC = \frac{\tau_w}{u\rho} S c^{-\frac{2}{3}}. \quad (2.9)$$

The WSS changes for different flow conditions at different positions and therefore, this correlation takes local effects into account.

### Diffusion Coefficient

For estimating the MTC, the diffusion coefficient  $D$  is needed at a given temperature. There are several equations in the literature for the calculation of the diffusion coefficient, of which some will be presented here. One of the earliest equations for diffusion in liquids is the Stoke-Einstein-equation (Einstein, 1905):

$$D = \frac{k_B T}{6\pi\mu_S R_0} \quad (2.10)$$

where  $k_B$  is the Boltzmann's constant,  $T$  the absolute temperature,  $\mu$  the dynamic viscosity of the solvent (subscript S), and  $R_0$  the Stoke radius of the diffusive species (subscript D) that can be considered spherical. This equation was adjusted by Wilke et al. (1955) with a semi-empirical relationship.

$$D = 7.4 \times 10^{-8} \frac{\sqrt{\phi_S M_S} T}{\mu_S \cdot V_D^{0.6}} \quad (2.11)$$

where  $\phi$  is the association factor of the solvent (2.6 for water),  $M$  the molecular weight of the solvent, and  $V$  is the molecular volume of the diffusive species. Madasamy et al. (2018) used the Paulson diffusion coefficient for their calculation of the MTC:

$$D = 9.4 \times 10^{-15} \frac{T}{\mu_S M_D^{\frac{1}{3}}}. \quad (2.12)$$

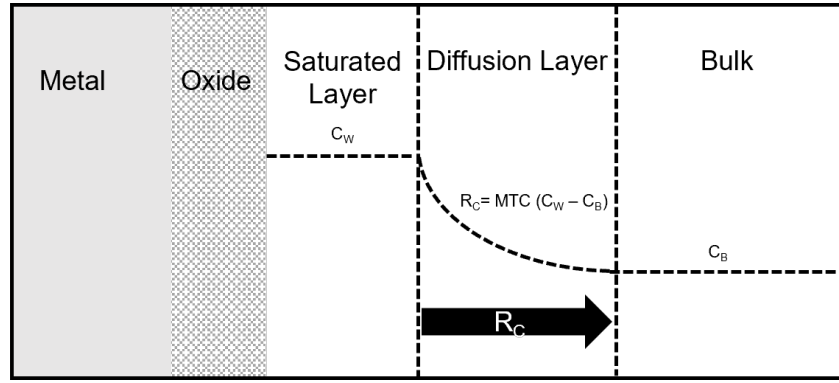
For this equation, the molecular weight of the diffusive species is needed. If the diffusion coefficient is known at a given temperature, the temperature dependence can be expressed as:

$$\frac{D_{T_1}}{D_{T_2}} = \frac{T_1 \eta_{T_2}}{T_2 \eta_{T_1}} \quad (2.13)$$

here the subscriptions  $T_1$  and  $T_2$  are the known and the unknown temperature level.

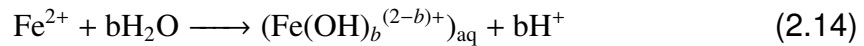
### 2.1.2 Concentration of the Eroded Material

According to equation 2.1, the MTC is the parameter which gives the distribution of the erosion rate, whereas the second term, the concentration difference, is considered as constant, and therefore, changes only the amplitude of the erosion rate and not the distribution. Estimating the concentration difference is not trivial and depends on a lot of different factors. In the mass controlled region, the



**Figure 2.2:** Scheme of the concentration gradient from the oxid layer to the bulk flow (according to Fujiwara et al. (2011))

dissolution is at its equilibrium, therefore, the assumption can be made that the concentration at the wall  $C_w$  is the equilibrium concentration  $C_e$ . Compared to the equilibrium concentration, the bulk concentration can be neglected in most cases, respectively, this assumption is conservative and a worst case scenario. Even with these simplifications, the estimation of the concentration at the wall depends on a lot of different chemical and thermodynamical parameters as well as on the used material. In Figure 2.2, a more detailed view of the dissolution process is shown. It can be seen that next to the oxide layer the concentration of the dissolved material ( $C_w$ ) is at its maximum. In case of a mass transfer controlled regime,  $C_w$  is the saturated concentration. There is a concentration gradient from the wall to the bulk. The solubility of iron is dependent on different parameters. In Fujiwara et al. (2011) temperature, pH, hydrolysis reaction of ferrous ions, the dissolution equilibria of  $Fe_3O_4$ ,  $FeO$ , and  $Fe(OH)_2$ , and the charge balance were taken into consideration and were evaluated. The hydrolysis reaction is the already above mentioned equation:



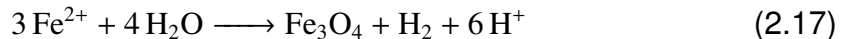
where  $b$  can be 1, 2 or 3 and every hydrolysis reaction has its own equilibrium constant.

$$K_b = \frac{[Fe(OH)_b^{(2-b)+}][H^+]^b}{[Fe^{2+}]} \quad (2.15)$$

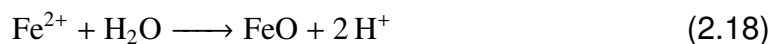
The solubility of the ferrous ions  $S_{Fe}$  is approximately

$$S_{Fe} = [Fe^{2+}] + [Fe(OH)^+] + [Fe(OH)_2] + [Fe(OH)_3^-] \quad (2.16)$$

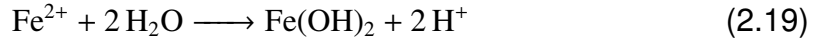
The oxide layer influences the solubility to that effect that it limits the dissolution of the aqua complex concentration of  $Fe^{2+}$ . Stable oxides, which can be formed, are  $Fe_3O_4$  (magnetite),  $FeO$ , or  $Fe(OH)_2$ . The dissolution equilibrium of magnetite ( $Fe_3O_4$ ) is:



The dissolution equilibrium of  $FeO$ :



and for Fe(OH)<sub>2</sub>:



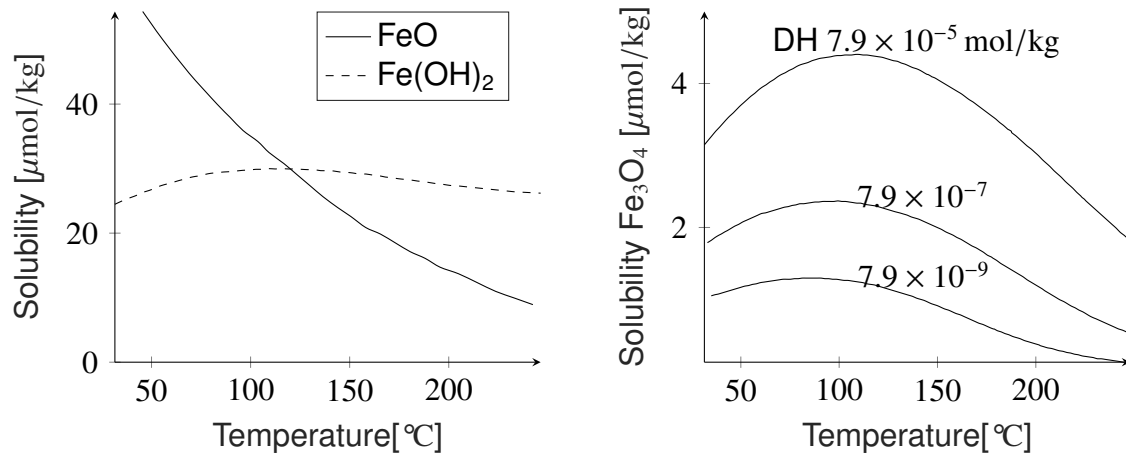
Each reaction has its own equilibrium constant. As a final step, a charge balance has to be done. In power plants, ammonia is a typical agent to control the pH, therefore, Fujiwara et al. (2011) did the charge balance with ammonia:

$$[\text{H}^+] + [\text{Fe}^{2+}] + [\text{Fe(OH)}^+] + [\text{NH}_4^+] = [\text{Fe(OH)}_3^+] + [\text{OH}]^- \quad (2.20)$$

The equilibrium constant K of all the involved reactions can be calculated with the change of the Gibbs free energy  $\Delta G^\circ$  :

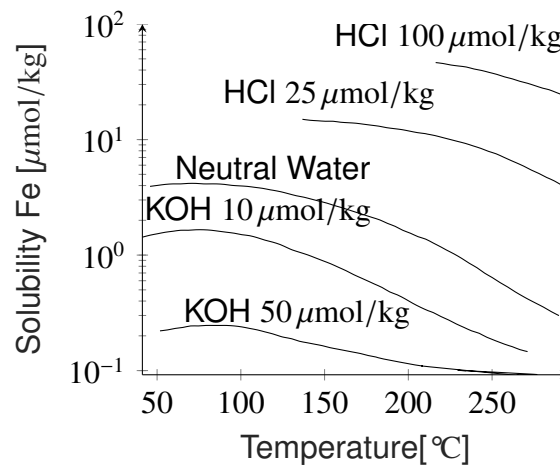
$$\Delta G^\circ = -RT \ln(K) \quad (2.21)$$

where R is the universal gas constant and T the temperature. The results of the solubility calculation can be seen in Figures 2.3a and 2.3b. In a direct comparison, it can be seen that the solubility in the presence of FeO and Fe(OH)<sub>2</sub> is significantly higher than with magnetite as the present oxide. From the dissolution equilibrium of magnetite shown in equation 2.17, it becomes clear that in this reaction elemental hydrogen is involved, which means that dissolved hydrogen will influence the balance of the chemical equilibrium. This behavior is shown additionally in Figure 2.3b, where DH means dissolved hydrogen, and more dissolved hydrogen leads to a shifting of the chemical equilibrium to the left, or in other words, to the side of dissolved Fe<sup>2+</sup>-ions. Sweeton et al. (1970) also studied the solubility of magnetite under different conditions; their results can be found in Figure 2.3c. In this work, they discussed the solubility under different pH conditions and different salts for the charge balance. It can be seen that these conditions also influence the solubility of magnetite. Summarized, it can be said that even under the assumption of a saturated layer, the chemical regime has to be known in detail to calculate the equilibrium concentration. A useful tool to assess the behavior of metals in aqueous solutions is the so called Pourbaix diagram. An example of a Pourbaix diagram is shown in Figure 2.4. It was made with the help of Uhlig et al. (2000) and it is described more detailed in the following. As it can be seen, Pourbaix diagrams are similar to phase diagrams, but, instead of pressure over temperature, they show the potential of the metal over pH-value of the fluid. It shows the thermodynamic equilibrium states of a specific metal-electrolyte system. In the case of Figure 2.4, the diagram was made for an iron-water system, where three solid species are considered (iron (Fe), magnetite (Fe<sub>3</sub>O<sub>4</sub>), and ferric oxide (Fe<sub>2</sub>O<sub>3</sub>)). Equilibrium state means that there is no information about the reaction's kinetics in the diagram, but nevertheless, correctly applied, important statements about corrosion phenomena can be made. The Pourbaix diagram in Figure 2.4 is a simplified version with only the necessary information for this work. For more detailed information about these kind of diagrams, Uhlig et al. (2000) or Pourbaix (1966) are recommended. Figure 2.4 was made for 298 K and at atmospheric pressure and with the help the equations from Uhlig et al. (2000). The dashed lines mark the thermodynamic stability of water at these conditions - above line O, water is unstable regarding to the evolution of oxygen, and below line H regarding to the evolution of hydrogen. For practical applications, it was found that a solubility



(a) Solubility of FeO and Fe(OH)<sub>2</sub> in regards to temperature (according to Fujiwara et al. (2011)).

(b) Solubility of Fe<sub>3</sub>O<sub>4</sub> in regards to temperature and dissolved hydrogen (DH) (according to Fujiwara et al. (2011)).



(c) Solubility in regards to temperature and with different pH-value (according to Sweeton et al. (1970)).

**Figure 2.3:** Solubility of iron ions under different conditions.



of  $10^{-6}$  g ion/l is considered as none corrosive conditions. In the diagram, line a represents this none corrosive condition. The colored lines represent higher concentrations ( $b=10^{-4}$ ,  $c=10^{-2}$ ,  $d=10^0$  g/l) and are the interesting lines for this work. They can be calculated with (Uhlig et al., 2000)

$$E = 0.98 - 0.2364pH - 0.0886\log([Fe^{2+}]). \quad (2.22)$$

From the equation, it becomes clear that these lines are dependent on the pH-value and the concentration of the iron ions. This relation can be used for the estimation of the saturated  $Fe^{2+}$ -concentration. As an example, the intersection point of line b and H is at a pH-value of 7.53, that means, for a pH-value of 7.53, the saturation concentration of iron ions is  $1 \times 10^{-4}$  g/l. The intersection point of H and b is crucial for this consideration because, below line H, the system is not stable. The same calculation in the other direction can be made, if the saturation concentration is wanted for a specific pH-value. To estimate the saturation concentration at pH 7, the intersection of the vertical line at pH 7, and line H has to be calculated (-0.414V). With the intersection point and equation 2.22, the saturation concentration can then be calculated (red dotted lines): At pH 7 the saturation concentration is  $1.15 \times 10^{-3}$  g/l. That means that the saturation concentration already rises by a factor of 11.5 for only a small variation of the pH-value. From this diagram, it can be also seen that there is no protective magnetite formed at this point, instead the iron is solved directly to  $Fe^{2+}$ . For this work, it helps to estimate and validate the magnitude of the saturation concentration.

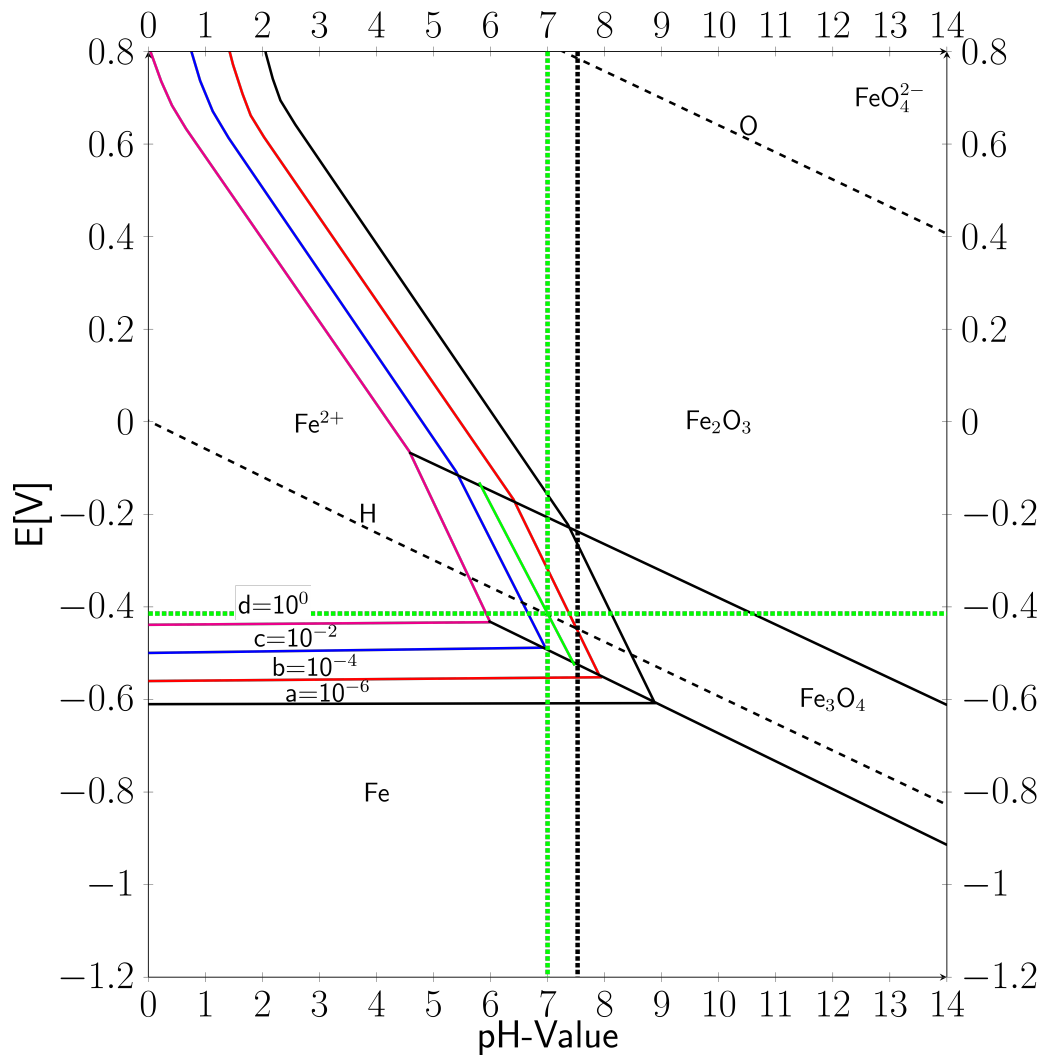
A last possibility to estimate the concentration difference is that it can be figured out indirectly with experimentally measured wall losses over time in a straight pipe. In that case, the erosion rate is known, and the MTC can be calculated with the Chilton-Colburn correlation for example. Therefore, the concentration difference can be calculated. With the assumption that the concentration difference does not change along the geometry, it can be used also for none straight geometries.

## 2.2 Liquid Metals

To be considered as a LM, metals or metal alloys should have a low melting point. It means that the liquid state is technical accessible, and therefore, economical affordable. Due to that, melting points should be in a range from room temperature up to 300 °C. In this section, a short introduction to LMs and their advantages shall be given. So it becomes clear why these working fluids could become important heat transfer fluids in the near future.

### 2.2.1 Requirements for Heat Transfer Fluids and resulting LMs and their properties

The main requirements for heat transfer fluids in the field of energy production were described by Becker (1980) and Bignon (1980) and summarized by Pacio et al. (2013):



**Figure 2.4:** Pourbaix diagram for a water iron system at 298 K and atmospheric pressure (According to Uhlig et al. (2000))

**Table 2.2:** Properties of the most important liquid metals at 600 °C and 1 bar. Water (at 20 °C). The numbers are based on Pacio et al. (2013)

Fluid	$T_{\min}$ [°C]	$T_{\max}$ [°C]	$\Delta T$ [°C]	$c_p$ [ $\frac{kJ}{kg \cdot K}$ ]	$\lambda$ [ $\frac{W}{m \cdot K}$ ]	$\rho$ [ $\frac{kg}{m^3}$ ]	$\nu$ [ $10^{-6} \frac{m^2}{s}$ ]
Sodium	98	883	785	1.25	46.0	808	2.6
LBE	125	1533	1408	0.15	12.8	9660	1.12
Lead	327	1743	1416	0.15	18.8	10324	1.18
Water	-	-	-	4.2	0.6	998	10

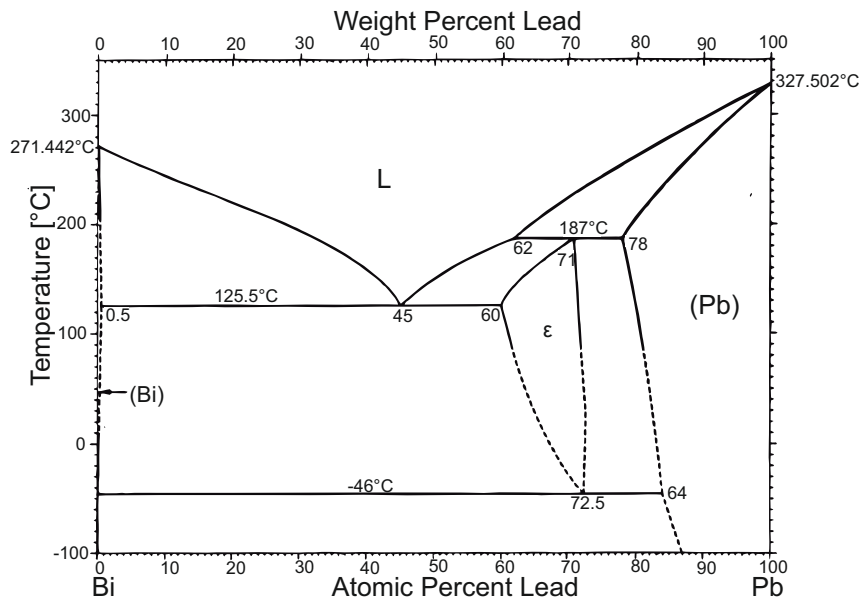
- *large temperature span* in which the fluid can be utilized which means a low melting point and a high boiling point. This permits high efficiencies.
- *high thermal conductivity* improves the heat transfer.
- A *low viscosity* reduces the pressure loss in the facility, and hence, the energy which is needed to pump the fluid
- A *high heat capacity* enables the fluid as a heat storage
- The fluid should have a *low corrosive potential*
- The fluid should have a *low risk potential*

With these aspects, LMs have advantages over other heat transfer fluids like water or solar salts. Lorenzin et al. (2016) emphasized the following advantages:

- wide range of operating temperature
- relatively low melting point
- thermal stability
- high allowable heat fluxes, due to high high thermal conductivities

Additionally in the field of nuclear power, liquid metal cooled reactors have the advantage that LMs allow a fast neutron spectrum and an operation at atmospheric pressure (Kelly, 2014). With the mentioned criteria, Lorenzin et al. (2016) chose different candidates for LMs applications, of which most promising ones are sodium, lead, and lead-bismuth eutectic (LBE). The physical properties of these fluids are shown in table 2.2 in contrast to water.

This work deals mainly with the group of HLM which are LBE and lead. Compared to sodium, they have a lower heat capacity and heat conductivity. From a thermodynamic point of view, the alkali metal should be therefore preferred as a heat transfer fluid. But they have other advantages. In contrast to sodium, they do not react with water and air in a strong exothermic reaction, their safety risk is therefore much lower, and they have a lower saturation pressure. So in general, the fluids are easier to handle. A problem occurring when using these fluids is the high erosion potential and their corrosive behavior towards structural materials. That is why this work deals with these kinds of fluids. This work deals with describing erosive processes numerically with Computational Fluid Dynamics (CFD) calculations to better understand critical parameters and to ideally reduce time-consuming experimental investigations in the future.



**Figure 2.5:** Phase diagram of lead (Pb) and bismuth (Bi) system according to Gokcen (1992)<sup>1</sup>

## 2.2.2 LBE and Lead

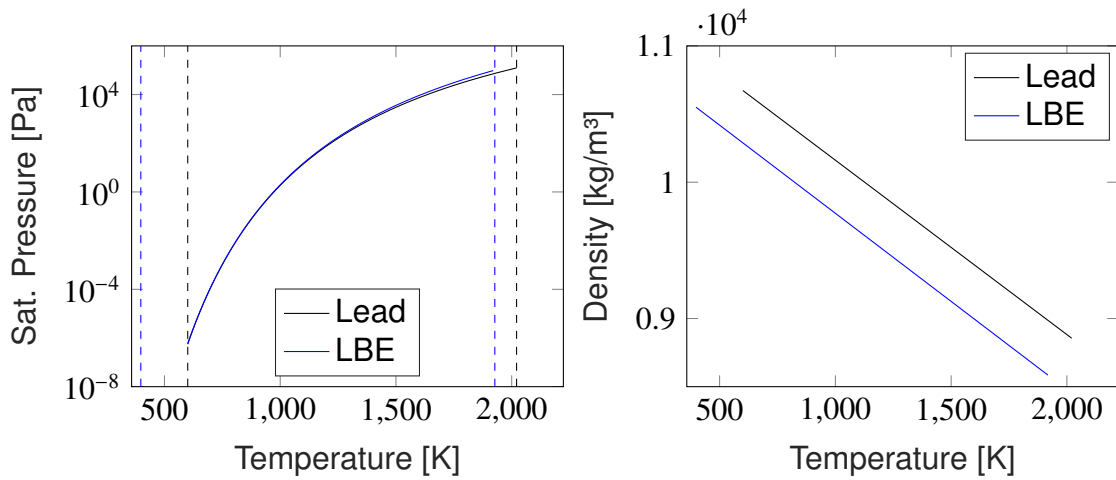
This section gives a short overview of the physical properties of LBE and lead. Lead is a pure metal whereas LBE is an eutectic alloy of lead and bismuth. The phase diagram of these two metals can be seen in Figure 2.5. This phase diagram is recommended by Fazio et al. (2015) for engineering and design calculation, and was made by Gokcen (1992). Eutectics systems are alloys which behave like pure substances, therefore it does not have, for example, a temperature melting range like ordinary mixtures. Instead, it has a melting point like pure substances. One other characteristic of an eutectic alloy is that its melting point is lower than the melting points of the involved pure metals. According to Fazio et al. (2015) and, as it can be seen in Figure 2.5, the eutectic point of the Pb-Bi system is at 45.0 atomic percent of lead and 55.0 % bismuth. In terms of weight percent, Fazio et al. (2015) mentions a recommended mixture of 44.5 weight percent lead and 55.5 weight percent bismuth. The recommended melting point at atmospheric pressure is  $398 \pm 1\text{K}$  ( $124.85\text{ °C}$ ), which differs slightly from the melting point in the given phase diagram. In contrast to LBE's melting point, bismuth melts at  $544.6 \pm 0.3\text{K}$  ( $271.45\text{ °C}$ ) and lead at  $600.6 \pm 0.1\text{K}$  ( $327.45\text{ °C}$ ).

In Figure 2.6, a few important selected physical properties of lead and LBE are shown as a function of temperature. All shown functions in these diagrams are the recommended ones from Fazio et al. (2015) and were chosen from Sobolev (2011). The saturation pressure  $p_{\text{sat}}$  is shown in Figure 2.6a and is accordingly following equations:

- Lead:

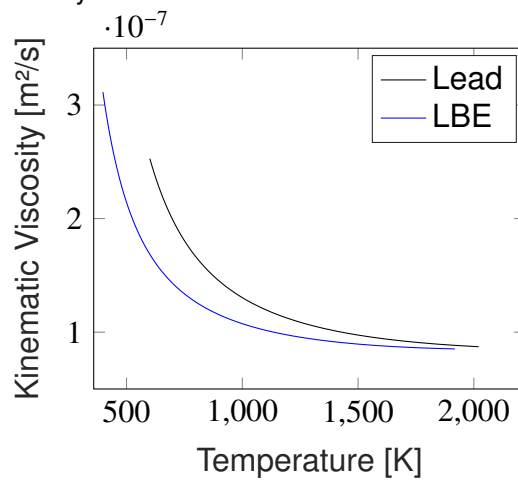
$$p_{\text{sat(Pb)}}[\text{Pa}] = 1.88 \times 10^{13} T^{-0.958} \exp\left(\frac{-23325}{T[\text{K}]}\right) \quad (2.23)$$

<sup>1</sup>Figure is reused with the permission of the rights owner



(a) Saturation pressure of lead and LBE. The dashed lines indicate the melting and boiling points of both fluids, respectively.

(b) Density of LBE and lead



(c) Kinematic viscosity of LBE and lead

**Figure 2.6:** Physical properties of LBE and lead as functions of temperature

- LBE:

$$p_{sat(LBE)}[Pa] = 1.22 \times 10^{10} \exp\left(\frac{-22552}{T[K]}\right) \quad (2.24)$$

The dashed lines in Figure 2.6 are the melting and the boiling point at normal atmospheric pressure. According to Fazio et al. (2015), the deviation for equation 2.24 is too large for lower temperatures, therefore the plot starts at 600 K. The saturation pressure is important for engineering applications because, if the saturation pressure is low at working conditions, there is no need to operate the facility higher than atmospheric pressure which makes the facility easier and cheaper to construct. Additionally, low saturation pressures reduces cavitation problems. The pressure has to fall below saturation pressure locally, so cavitation can happen. At a reasonable working temperature of 600 °C, lead and LBE have a saturation pressure of 0.75 Pa and 0.74 Pa, respectively, compared to an atmospheric pressure of 101 300 Pa. The saturation pressure is negligible in both cases, and cavitation should not be an hazard.

The density of the fluids follows a linear regression and can be seen in Figure 2.6b and are defined by equation 2.25 and 2.26:

- Lead:

$$\rho_{Pb} \left[ \frac{kg}{m^3} \right] = 11441 - 1.2795 T[K] \quad (2.25)$$

- LBE:

$$\rho_{Pb} \left[ \frac{kg}{m^3} \right] = 11065 - 1.293 T[K] \quad (2.26)$$

From the diagram, it can be seen that the density is between 9000 to 10 000 kg/m<sup>3</sup> which is around ten times higher than water. From a hydrodynamic point of view, this leads to high dynamic forces on the structural material and an high use of power to transport these fluids. These characteristics will be discussed in later chapters.

The last characteristic, which shall be presented in this chapter, is the viscosity. There are two kinds of viscosity: the dynamic viscosity  $\mu$  and the kinematic viscosity  $\nu$ . The kinematic viscosity is the ratio of dynamic viscosity and density and is more often used in the engineering field (Fazio et al., 2015). The kinematic viscosity is shown in Figure 2.6c, and the equations from Fazio et al. (2015) for the dynamic viscosity were therefore adapted.

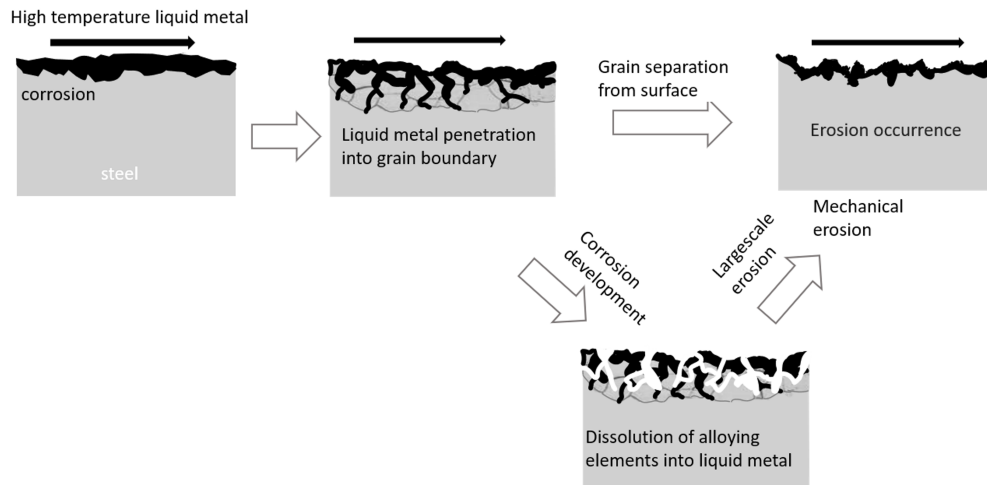
- Lead:

$$\nu_{Pb} \left[ \frac{m^2}{s} \right] = \frac{4.55 \times 10^{-4} \exp\left(\frac{1069}{T[K]}\right)}{\rho_{(Pb)}} \quad (2.27)$$

- LBE:

$$\nu_{Pb} \left[ \frac{m^2}{s} \right] = \frac{4.94 \times 10^{-4} \exp\left(\frac{754.1}{T[K]}\right)}{\rho_{(LBE)}} \quad (2.28)$$

At 600 °C, lead and LBE have at a kinematic viscosity of  $1.5 \times 10^{-7} m^2/s$  and  $1.2 \times 10^{-7} m^2/s$ , respectively, which is around eight times lower than kinematic

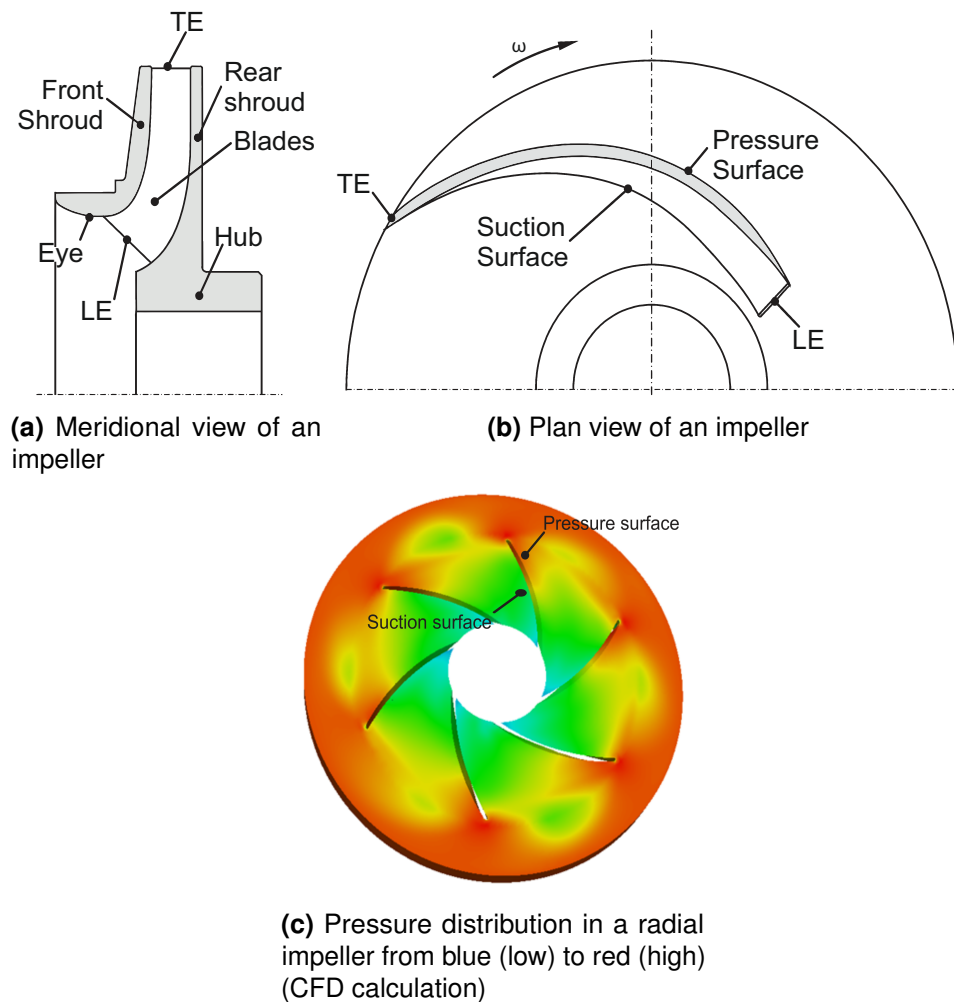


**Figure 2.7:** Erosion Scheme in LBE according to Kondo et al. (2005)

viscosity of water, which is  $1.0 \times 10^{-6} \text{ m}^2/\text{s}$  at  $20 \text{ }^\circ\text{C}$ . In numerical calculations, this becomes important because the lower kinematic viscosity demands a finer mesh at the wall, as described in a later chapter.

### 2.2.3 Erosion in LBE

In section 2.1, the general mechanism for this work's important erosion processes were discussed. In this section, the special mechanisms and problems of erosion in LBE streams will be described, but they can be transferred also to other HLM. The general behavior can be seen in Figure 2.7 by Kondo et al. (2005). In a first step, corrosion occurs on the surface of the structural material. Then the grain boundaries get penetrated by the hot LBE and are weakened. From there, two different processes can lead to large scale erosion. In the direct mechanical way, the erosion happens because of the shear forces, which act on structural material. Hence, the dynamic pressure and wall shear stress of LBE streams are around ten times higher than compared to water because of the density difference (Kondo et al., 2005). It shows the same behavior like the described process in Figure 2.1a, but for HLMS, this process occurs at much lower velocities than compared to water (Zhang et al., 2008). Therefore, it is recommended that with the current structural materials, the flow velocity should not exceed  $2 \text{ m/s}$ . With special structural materials, like silicon carbide and titanium for pump impellers, a maximum velocity of  $10 \text{ m/s}$  could be allowed (Alemberti, 2015) (Borreani et al., 2017). Alternatively, the LBE can dissolve alloying materials of the structural material which may enhance the weakness of the structural materials, and larger lumps get detached from the steel. The dissolved components can be precipitated in colder regions of the facility as crystals because of the difference in solubility (Kikuchi et al., 2003). These crystals are an additional source of particles. The lumps and particles then can be another cause of erosion as described in chapter 2.1 (Erosion with abrasive particles).



**Figure 2.8:** Impeller components and definition of key areas of an impeller blade as well as a qualitative pressure distribution in an impeller (Gülich, 2014c) <sup>2</sup>

## 2.3 Basic Knowledge of Centrifugal Pumps

In this thesis, the impeller of centrifugal pumps is used as a possible application for the presented investigation method for erosion problems. It is an example for a more complicated geometry. To understand the chapters concerning the impeller, a short overview of the basic principles, the performance characteristics, and specific speed are given in the following. More detailed information can be found in the fundamental books by Gülich (2014a) and Wesche (2016b).

### 2.3.1 Principles

Centrifugal pumps, which belong to turbo machines, are used to raise a specific volume flow to a certain pressure level. The needed energy is transferred from the pump to the fluid by hydrodynamic processes. The energy and the pressure differences are proportional to the square of the rotor speed. The main parts of a centrifugal pump are a casing, a shaft, and an impeller. The impeller is necessary

<sup>2</sup>Figure 2.8a and 2.8b are reused with the permission of the rights owner



to transfer the energy into the fluid (Gülich, 2014c). The fluid is accelerated in circumferential direction which leads to a rise of static pressure according to the following equation (Gülich, 2013):

$$\frac{dp}{dr} = \rho \frac{c^2}{r} \quad (2.29)$$

where  $p$  is the static pressure,  $r$  the radius,  $\rho$  the density of the fluid, and  $c$  the absolute velocity. From this equation, it can be seen that flows with a curved path are always linked to a pressure gradient normal to the flow's direction. The pressure rises from the momentary center towards the outside of the curvature. At the exit of the impeller, the fluid is decelerated to transform most of the hydrodynamic pressure to static pressure. The impeller consists of four main parts: The front and rear shroud, the blades, and the hub. The impeller with its components can be seen in the meridional section in Figure 2.8a. The plan view of the radial impeller is shown in Figure 2.8b. There,  $\omega$  is the angular rotor velocity, and the arrow indicates the rotating direction. The surface of the blade facing the rotational direction experiences the highest pressure for a given radius, therefore, it is called pressure side or pressure surface. The surface on the other side is called suction side or suction surface, it is the surface with the lower pressure. Also in Figure 2.8, the leading edge (LE) and trailing edge (TE) are defined. They are the edges of the blades at the inlet (LE) and at the outlet (TE) of the impeller. In Figure 2.8c, a CFD calculation of the pressure distribution is shown to visualize the previously described phenomenon. The pressure rises from the center of the impeller to the outlet, and it can be also seen that the pressure at the pressure side is higher than on the other side.

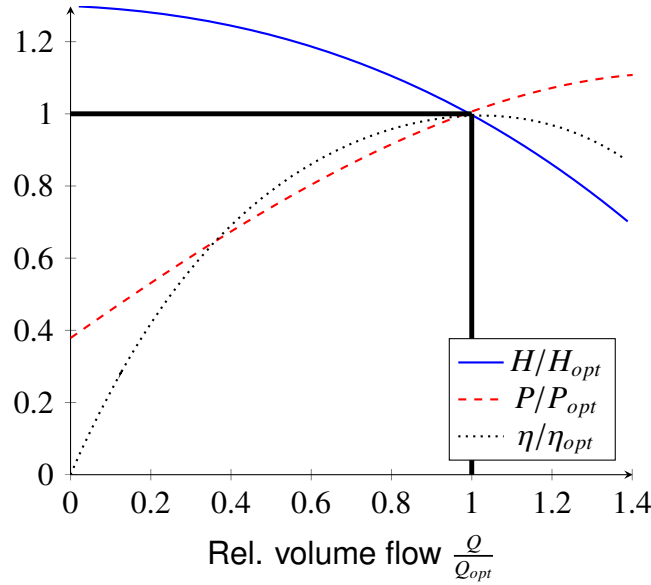
### 2.3.2 Performance Characteristics

The operational requirement for pumps often demands that they operate not always at their given design point. The design point is defined by the optimal volume flow  $Q_{opt}$ . At this point, the efficiency  $\eta$  of the pump is the highest. If the quotient of volume flow and the optimal volume flow is smaller than 1,  $\frac{Q}{Q_{opt}} < 1$ , the pump operates in the partload region, and if it is higher than 1, in the overload region. A typical behavior of a centrifugal pump for the off design regions is shown in Figure 2.9. This diagram is called pump characteristics and describes the behavior of the **head  $H$** , **pump power output  $P_Q$** , and **efficiency  $\eta$**  as a function of the volume flow  $Q$ . If the head is steadily falling with the volume flow, i.e.  $\partial H / \partial Q < 0$ , like in the diagram, it is a so called stable characteristic, otherwise an unstable. Stable curves are required in most applications (Gülich, 2014b). The head of a pump  $H$  is defined as the pump output power  $P_Q$  in relation to the term  $\rho \times g \times Q$  where  $\rho$  is the density of the fluid,  $g$  the acceleration due to gravity, and  $Q$  the volume flow (Gülich, 2014c).

- Head over volume flow:

$$H = \frac{P_Q}{\rho g Q} \quad (2.30)$$

with the help of the Bernoulli law  $P_Q$  can be calculated (Gülich, 2014c):



**Figure 2.9:** Typical characteristic curve of a centrifugal pump

- Pump power output over volume flow:

$$P_Q = \left( (p_p - p_s) + \frac{\rho(u_p^2 - u_s^2)}{2} + \rho g (z_p - z_s) \right) Q \quad (2.31)$$

where  $p$  is the static pressure on the suction side ( $p_s$ ) and on the pressure side ( $p_p$ ),  $u_s$  and  $u_p$  the velocities on the different sides, and  $z_s$  and  $z_p$  the height coordinates. By using the equation 2.31 in 2.30 the head can be calculated

$$H = \frac{p_p - p_s}{\rho g} + \frac{u_p^2 - u_s^2}{2g} + z_p - z_s. \quad (2.32)$$

The last curve is the efficiency curve of the pump and it is given by

$$\eta = \frac{P_Q}{P} \quad (2.33)$$

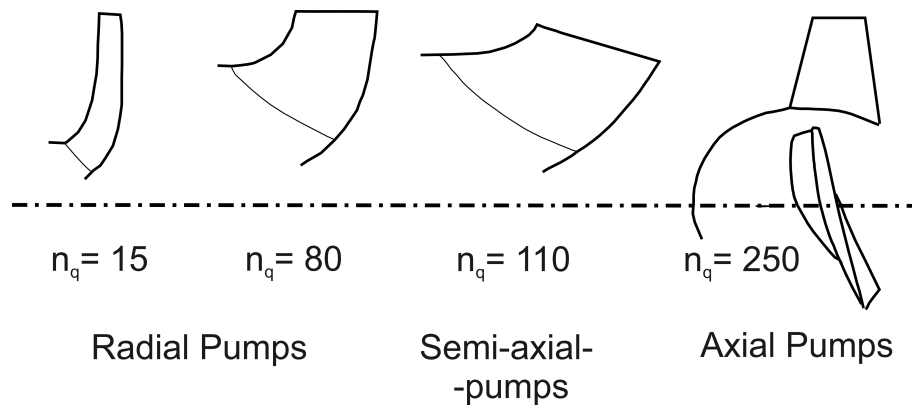
where  $P$  is the power input (Gülich, 2014c).

### 2.3.3 Specific Speed

The specific speed is an important characteristic number for impeller pumps. Impellers with the same specific speed could be designed geometrically similar. The specific speed arise from similarity law considerations. This number is the most important number to classify pump impellers. Because of this, it is described more detailed at this point.

Defined is the specific speed in Pfleiderer (1961) for example as

$$n_q = n \frac{(Q_{opt}/1 \frac{m^3}{s})^{0.5}}{(H_{opt}/1m)^{\frac{3}{4}}} [1/min]. \quad (2.34)$$



**Figure 2.10:** Different kinds of impellers as a function of the specific speed  $n_q$  (according to Wesche (2016a)).

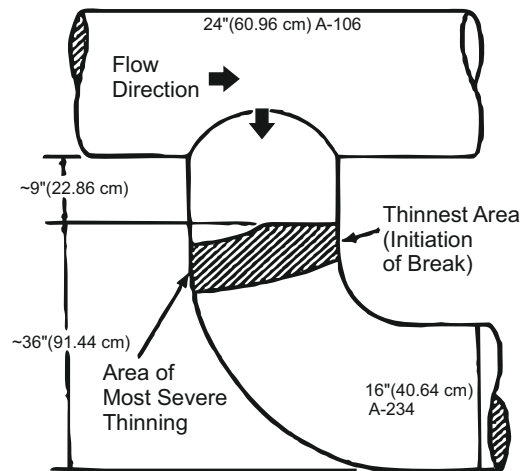
The specific speed  $n_q$  connects the volume flow  $Q$  with the head  $H$  rotational speed  $n$  at the design point. Impellers with the same specific speed can be built geometrically similar. The specific speed can be interpreted as the theoretical rotational speed of a geometrically similar impeller which has to pump a volume flow of  $1 \text{ m}^3/\text{s}$  on a head of  $1 \text{ m}$ . Strictly spoken, the specific speed introduced in equation 2.34 is not dimensionless, it has the unit rotations per minutes. There is a completely dimensionless number defined in Stepanoff (1957a):

$$n_q = n \frac{(Q_{opt})^{0.5}}{(g H_{opt})^{\frac{3}{4}}} \quad (2.35)$$

In that case, the unit of the rotational speed has to be  $1/\text{s}$  but out of historical reasons, the definition of equation 2.34 is more common, and therefore, more used. Centrifugal pumps can be built in a range of  $n_q \sim 7$  up to around 400. As it can be seen in Figure 2.10, the kind of the impeller changes with the specific speed from radial over semi-axial to axial impellers. This work deals solely with radial impellers, which means impellers with an specific speed up to  $\sim 80$  to 100 (Wesche, 2016a). The impact of the specific speed on the impeller design and general basics of the impeller design will be described in a later chapter.

## 2.4 Previous and Related Work

From the sections before, it should become clear that erosion is a term which combines many different chemical and mechanical processes in one term. These processes are important in many different fields, not only in the field of engineering. Hence, the investigation of this field has a long history and is discussed in many different forms. Because of this, this section does not have the aspiration to give an overview of all kinds of erosion processes and give the state of the art of this field. In fact, this section has the only goal to give an overview of erosion modeling which is important or linked to this work. This work mainly deals with how to establish a modeling method for the erosion process, therefore, this section has a look on how other works do the modeling. The following sections can be grouped into four subcategories: The numerical investigation of FAC and particle erosion (abrasion),



**Figure 2.11:** Schematic Situation of the Surry Unit 2 failure according to Kang et al. (2008)<sup>3</sup>

erosion behavior of heavy LM, and an overview on centrifugal pumps with liquid metals as a working fluid.

## 2.4.1 Overview of Numerical Investigations of FAC

### FAC Investigation by Comparison

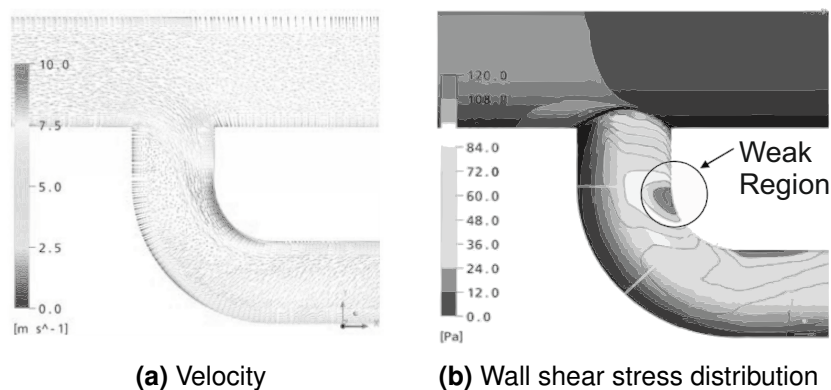
The first step of numerical investigations of the phenomenon of FAC is to calculate the flow condition in a known geometry where FAC is a known problem and leads to a severe wall loss or even to a pipe failure. As described in the previous sections, it is estimated that the WSS  $\tau_w$  is the leading cause of FAC. The works utilize this assumption to calculate the WSS and compare it with the seen FAC.

Kang et al. (2008) used this method for investigating the FAC-caused wall thinning in CANDU reactor feeder pipes. CANDU stands for CANada Deuterium Uranium. It is a pressurized water reactor which uses heavy water as the moderator in the primary coolant loop. Like most of the studies, this work assumes that the corrosion depends on the pH value, temperature of the water, structural material, and deuterium concentration. These factors affect more or less the whole system homogeneously. In contrast, the erosion depends on the flow velocity, and thus, on the shear stress, and these parameters vary with the position. With this said, additional wall loss can always be led back to hydrodynamic factors. The investigated case for testing their method was the Surry Unit 2 failure in 1986. Due to the reports of the United States Nuclear Regulatory Commission Office of Inspection and Enforcement (USNRC) (Jordan, 1986) (Jordan, 1987), it is clear that the event was caused by FAC: In general, the wall thickness decreased from 0.5 inch (1.27 cm) to 0.25 inch (0.635 cm), whereas at the breaking point the wall thickness was only 0.0625 inch (0.16 cm). The schematic of the failure can be seen in Figure 2.11. The break happened at a T-junction where the flow enters from a 24 inch pipe into an 18 inch pipe. The 18 inch pipe becomes a 90° elbow like it is shown in the Figure. The area of the severe wall loss is placed directly before

<sup>3</sup>Kang et al. (2008) published under an open access licence, which permits the reuse.

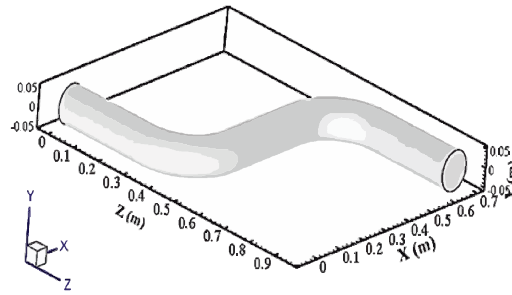
**Table 2.3:** Summary of the geometry and flow conditions for Kang et al. (2008)

Kang et al. (2008)	
<b>Geometry</b>	
Main Pipe	24 inch (60.96 cm)
Connected Pipe	18 inch (45.72 cm)
Bend angle	90°
<b>Conditions</b>	
Fluid	light water
Temperature	188 °C
Inlet mass flow	1260 kg/s
Outlet mass flow (each)	630 kg/s
Reference pressure	3.2 MPa
<b>Code</b>	
CFX-5.10	

**Figure 2.12:** CFD calculations from the Surry Unit 2 failure from Kang et al. (2008).<sup>4</sup>

the bend of the elbow. In Figure 2.12, the CFD results from Kang et al. (2008) of this geometry can be seen. In Figure 2.12a, the velocity vectors are presented, and in Figure 2.12b, the WSS, which is derived from the velocity vectors, is on display. The CFD calculation was done with the commercial code Ansys CFX. The case was a steady state simulation with the  $k-\epsilon$ -model as a turbulence model, but the Shear Stress Transport model ( $k-\omega$ -SST) (SST) was also tested with no big differences for the distribution of the WSS. The detailed geometry and flow conditions for the simulation are listed in Table 2.3. Comparing Figure 2.11 and 2.12b, it becomes clear that the region of high WSS is equivalent to the region of high wall loss. Due to this observation, Kang et al. (2008) conclude that the WSS distribution is a suitable tool to find regions of high wall loss, and therefore, regions which need a closer monitoring. Hence, they investigate the feeder pipes of the Wolsung unit 1 in Korea with their method. During their investigation, they found out that the present monitoring points are not sufficient because areas with large WSS are not covered. Another approach goes one step further, but it is still a comparative approach. As already written in section 2.1, the general term

<sup>4</sup>Kang et al. (2008) published under an open access licence, which permits the reuse.



**Figure 2.13:** Double elbow geometry with the coordinate system of Keshtkar et al. (2016).<sup>5</sup>

for the FAC rate is defined in equation 2.1. The studies assume that for the given flow domain, the concentration difference of the dissolved material is constant. Therefore, the concentration difference is a scaling factor for the MTC and does not effect the shape of the distribution of the wall thinning. In that case, the knowledge of the MTC distribution is enough to find the hot spots of the FAC. The MTC distribution would be similar to the method of Kain, Roychowdhury, Mathew, et al. (2008). Studies which use this approach are, for example, Keshtkar et al. (2016) and Rani et al. (2014). Both studies have a double elbow as investigated geometry. Systematical experimental investigations of wall loss over time are rare. Hence, both studies use damaged elbows in their final state to validate their studies. Keshtkar et al. (2016) used a unspecified damaged double elbow, whereas Rani et al. (2014) used inspections of wall thinning in a 90° and 73° elbow of an Indian nuclear power plant and CANDU nuclear power plant, respectively. The experimental investigations were taken from Slade et al. (2005). The summary of the geometry and the flow conditions of both studies can be found in Table 2.4. Under the turbulence flow conditions, both studies used the already in equation 2.9 introduced Chilton-Colburn equation. In the study of Keshtkar et al. (2016), the MTC was investigated in relation to the Reynolds number and the dimensionless distance ( $L/D$ ), where  $L$  is the distance between and  $D$  the diameter of both elbows. In Figure 2.14, most of the results of Keshtkar et al. (2016) are summarized for the  $L/D$  ratio of 2.85. There the simulated MTC for different Reynolds numbers along the  $X$  ordinate can be seen. For better visualization, the corresponding geometry is shown in Figure 2.13 with the matching coordinates. The first observed increase belongs to the extrados of the first elbow, whereas the second increase belongs to the intrados of the second elbow, where also the overall maximum MTC occurs. For this  $L/D$ -ratio, the MTC stays nearly at the level of the outlet of the first elbow between the two elbows. Then the MTC rises sharply in the intrados of the second elbow before it drops again. The described general behavior of the MTC is the same for all investigated Reynolds numbers, but for higher Reynolds numbers it is shifted to higher MTCs, whereas according to Keshtkar et al. (2016) the rise of maximum MTC is not linear connected to the Reynolds number. Keshtkar et al. (2016) also compare the MTC distribution of the second elbow with measured wall thickness at the same position. In the diagram, the dashed line indicates the measurements at the wall, and as it can be seen, there is a good coincidence

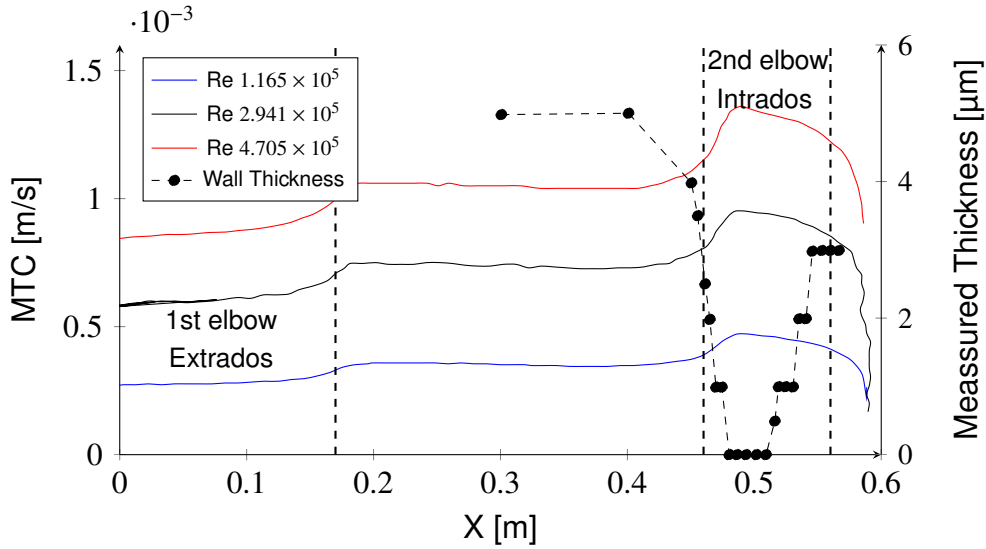
<sup>5</sup>Figure is reused with the permission of the rights owner

**Table 2.4:** Key parameter of the investigations by Keshtkar et al. (2016) and Rani et al. (2014)

<b>Keshtkar et al. (2016)</b>		<b>Rani et al. (2014)</b>	
<b>Geometry</b>		<b>Geometry</b>	
Typ	Double elbow	Typ	single elbow
Bend angle	90°	Bend angle	73°
Inner diameter $D_i$	105 mm	Inner diameter $D_i$	59 mm
Outer diameter	115 mm	Outer diameter	63.5 mm
Bend radius $R_b$	170 mm	Bend radius $R_b$	95.25 mm
L/D	2.85	<b>Conditions</b>	
<b>Conditions</b>		Fluid	havy water
Fluid	water	Temperature	310 °C
Temperature	120 °C	Reynolds number	$6.27 \times 10^6$
Reynolds number	$1.18 \times 10^5$	Schmidt number	9.2
	$-4.7 \times 10^5$	<b>Code</b>	
Schmidt number	42	ANSYS Fluent 12.1	
<b>Code</b>		Turbulence model	k-ε
ANSYS CFX15			
Turbulence model	k-ε		

between the location of minimum wall thickness and maximum MTC.

Rani et al. (2014) did a similar investigation with a focus on the occurring secondary flows in the double elbows. For validation of the work, single elbows with 73° and 90° bends, respectively, were used. Compared to Keshtkar et al. (2016), this study uses for the 73° bend an higher Reynolds number ( $6.27 \times 10^6$ ) and a significant lower Schmidt number (9.2). For the Chilton-Colburn equation 2.9, this means that the calculated MTC is explicitly higher than in the work of Keshtkar et al. (2016). The simulation results for the MTC calculation are shown in Figure 2.15b. According to this distribution, the maximum MTC occurs at the beginning of the intrados of the 73° bend and at the outlet of the extrados. The minimum MTC is calculated at the outlet of the intrados. Comparing quantitatively the simulated MTC from Rani et al. (2014) with Keshtkar et al. (2016), the overall MTC of Rani et al. (2014) is significantly higher as it is expected due to the higher Reynolds number which means higher mean velocity, higher WSS, and lower Schmidt number. The results of this investigation are compared to the FAC rate measurements under CANDU conditions. The measurement results are shown in Figure 2.15a. In this case, the FAC rate is measured in  $\mu\text{m}/\text{EFPY}$ . EFPY stands for Effective Full Power Year and is therefore a time equivalent. In other words, the FAC rate is the wall loss in micrometer per year if the nuclear power plant would be under full power the whole year. From the FAC rate distribution, it becomes clear that the bend suffers the most wall loss at the same position where Rani et al. (2014) expect the highest MTC: At the inlet of the intrados ( $130 \mu\text{m}/\text{EFPY}$ ) and at the outlet of the extrados ( $110 \mu\text{m}/\text{EFPY}$ ). And with  $40 \mu\text{m}/\text{EFPY}$ , the minimum FAC rate is measured at the outlet of the intrados consistently with the simulated MTC minimum. Rani et al. (2014) conclude with this method of calculating the MTC, it is possible to predict



**Figure 2.14:** MTC simulation results of Keshtkar et al. (2016) for different Reynolds numbers compared to the wall thickness measurements of a double elbow along the X ordinate.

the locations of high wall loss and therefore, this method is suitable for investigating erosion processes.

### FAC Investigation by Calculating the FAC Rate

The presented studies above have in common that they do not calculate the wall loss directly. They are examples of studies where the investigation focus is on a quantity (WSS, MTC) which is closely linked to the wall loss. In this section, examples of studies are presented which try to calculate the wall loss and not only a linked quantity.

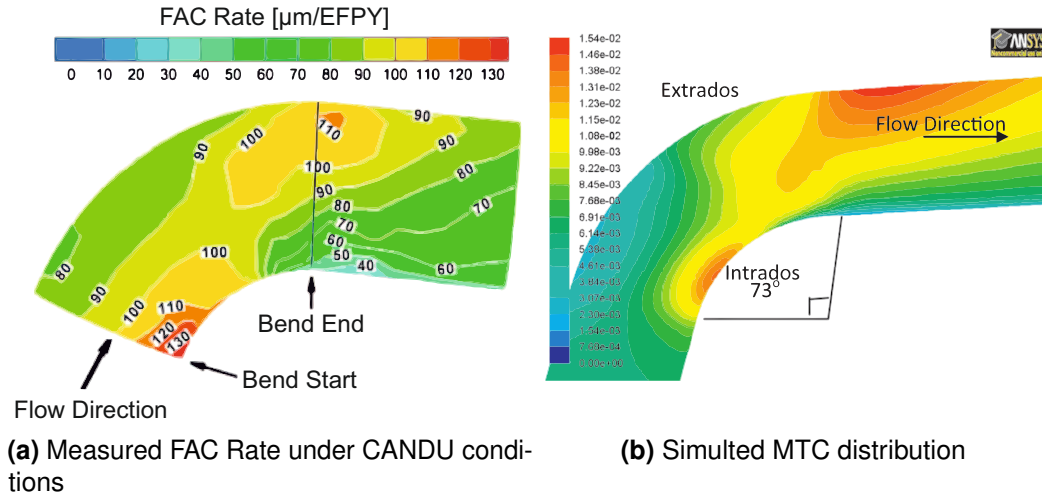
The study of Prasad et al. (2018) is one of these investigations which uses this different approach to calculate the wall loss. Prasad et al. (2018) calculate the FAC rate with the following equation:

$$R_c = \frac{(C_e - C_b)\theta}{\frac{1}{K_r} + (1 - f)\left(\frac{\delta}{D} + \frac{\theta}{MTC}\right)} \quad (2.36)$$

The equation was derived from the considerations that the FAC rate is equal to the production of metal oxide and the mass transport through the oxide layer. The FAC rate is, therefore, dependent on the porosity  $\theta$  of the oxide layer, the equilibrium concentration  $C_e$ , the bulk concentration  $C_b$ , the diffusion coefficient  $D$ , the thickness of the oxide layer  $\delta$ , the mass transfer coefficient  $MTC$ , and the reaction rate  $K_r$ . With  $f$  being the fraction of oxidized iron, and therefore, is  $1-f$  the fraction which diffuses through the oxide layer. The FAC rate  $R_c$  is the mass loss over time per area ( $\text{kg}/(\text{s m}^2)$ ). To transform the FAC rate to a wall loss over time, the following equation is used

$$R_c = \rho_s \frac{dh}{dt} \quad (2.37)$$





**Figure 2.15:** MTC calculations of Rani et al. (2014)<sup>6</sup> compared to FAC rate measurements of Slade et al. (2005) in a 73° elbow.

where  $\rho_s$  is the density of the structural material. For the MTC, Prasad et al. (2018) assume that it can be separated in two factors which are independent from each other:

$$MTC = K_g K_d(t) \quad (2.38)$$

where  $K_g$  is the geometric factor for non-straight pipes and  $K_d$  is the time-dependent part. The time dependencies is caused by the wall loss and will be described later. The geometric factor is the ratio between a non-straight pipe and a straight pipe. It is the factor which describes the deviation of the actual MTC from the MTC at a straight pipe.  $K_g$  has to be determined experimentally with CFD simulations. Prasad et al. (2018) used a CFD calculation for determining it. The second factor is determined with the help of the Sherwood number

$$Sh = K_d(t) \frac{D_i}{D} \quad (2.39)$$

where  $D_i$  is the characteristic length, in this case the inner diameter. The Sherwood number is calculated with the correlation of Petukhov (1970), a correlation for straight pipes with fully developed velocity and concentration profile for hydraulic smooth and rough walls with Reynolds number range of  $1 \times 10^4$  to  $5 \times 10^6$  (Pietralik, 2012):

$$Sh = \frac{\zeta(t)}{8} \frac{ReSc}{1.07 + \sqrt{\frac{\zeta}{8}(Sc^{0.667} - 1)}} \quad (2.40)$$

with

$$\zeta(t) = \left( 1.8 \log \left( \frac{6.9}{Re} + \left( \frac{\epsilon(t)}{3.75D_i} \right)^{1.11} \right) \right)^{-2} \quad (2.41)$$

where  $\zeta$  is the hydraulic resistance coefficient with  $\epsilon$  being the surface roughness. Prasad et al. (2018) assume that the surface roughness is equal to the wall loss

<sup>6</sup>Figure 2.15a and 2.15b are reused with the permission of the rights owner

( $\varepsilon(t)=h(t)$ ). Hence, the surface roughness is time-dependent. With the equations 2.38 to 2.41 it is possible to write a new term for the MTC:

$$MTC = K_g \frac{D}{D_i} Sh = K_g \frac{D}{D_i} \frac{\zeta(t)}{8} \frac{ReSc}{1.07 + \sqrt{\frac{\zeta}{8}(Sc^{0.667} - 1)}} \quad (2.42)$$

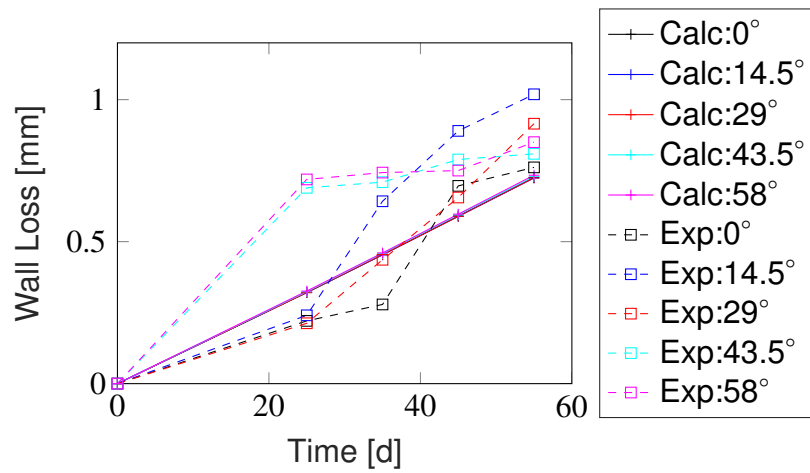
With this term and equation 2.37, the change of the wall thickness can be calculated. To determine the geometric factor with CFD, a two dimensional case is used. For the simulation, a fine mesh at the wall is generated, and for the turbulence, the k- $\omega$  SST model is used. The idea for calculating the wanted factor is that water is used as the solvent and Calcium sulphate is used as the solute. Pure water streams into the domain via the inlet and the concentration fraction of the solute at the wall of the computational domain is kept at 1 (pure calcium sulphate). Then the MTC is evaluated at different points of the computational domain and at the straight pipe with following equation:

$$MTC = \frac{D(C_s - C_1)}{\Delta y(C_s - C_b)} \quad (2.43)$$

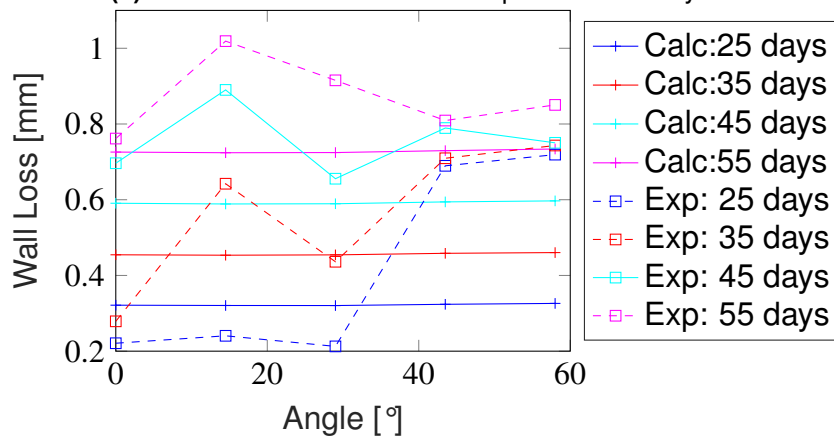
where  $C_s$  is the concentration of the solute at the surface,  $C_1$  the concentration at the first mesh node and  $C_b$  in the bulk, and  $\Delta y$  is the grid size of the first layer. By obtaining the concentrations from the CFD study, a local MTC can be determined and can be put into perspective with the MTC of a straight pipe:

$$K_g = \frac{MTC_{local}}{MTC_{pipe}} \quad (2.44)$$

This idea works with the assumption that it does not matter what kind of solute is used, and that the enhancement/deterioration of the MTC is independent of the solute. The validation of this approach was done by an experimental investigation of an 58° elbow (Prasad et al., 2018). The wall thinning of the extrados was measured over a time period 55 days every 14.5°. The detailed description of the conducted experiment can be read in chapter 5.1.1. At this point, only the theoretical results will be compared to the experimental results. The results can be found in Figure 2.16. As it can be seen in Figure 2.16a, the theoretical calculated wall loss over time is for all positions nearly linear. The experimental results do not show a linear behavior over time, and furthermore, the experimental measurements show a different behavior for each locations. This indicates that the geometric factor has a strong impact on the results. In Figure 2.16b, the wall loss is compared to the position. There it becomes clear that the geometric factor has nearly no effect on the theoretical calculation. For all time steps, there is a horizontal line. Hence, the wall loss is always the same at each position. The experimental results are discussed in chapter 5.1.3 in more detail. For now, it can be concluded that the theoretical approach is underestimating the geometrical factor or it does not consider it at all.

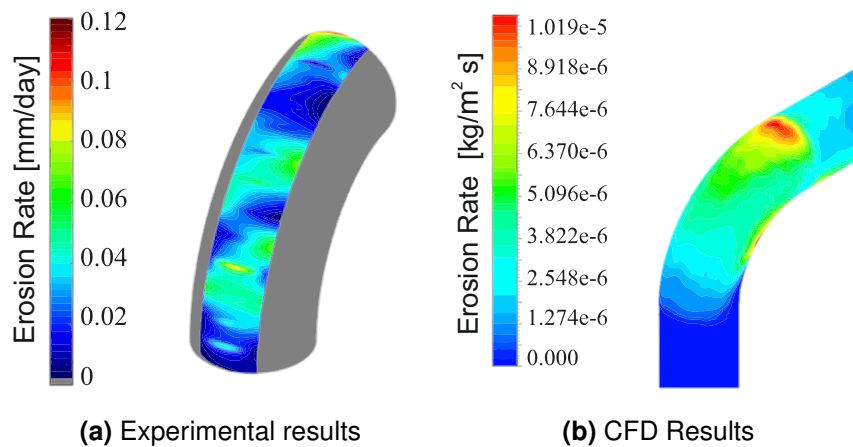


(a) Wall loss at the extrados in dependence of days.



(b) Wall loss at the extrados in dependence of angle

Figure 2.16: Theoretical and experimental results of Prasad et al. (2018)



**Figure 2.17:** Experimental and CFD results from Sedrez et al. (2019)<sup>7</sup>

## 2.4.2 Overview of Numerical Investigations of Abrasion

Like any other type of erosion, particle erosion (abrasion) is a broad field. Because of its relevance, in the gas and oil industry, for example, there are a lot of studies concerning this issue. In general, there can be distinguished between two main systems: Solid particles in a gas stream or in a liquid flow. This work only deals with the latter one. Particle erosion is a purely mechanical process which occurs mainly at regions, where the flow suddenly changes. Therefore, valves, tees, chokes, and elbows have a high risk to suffer from this kind of erosion. Because of the inertia of the solid particles, the particle can not follow the path lines of the flow. A part of the solids impinge on the wall, and erosion can happen over time. How severe the wall interaction is, depends on several parameters: The velocity of the flow, the combination of fluid and the material of the solid particles, structural material, the shape of the particle, impact angle, and velocity of the particle before the impact. As it can be seen, this selection of possible parameters already offers many combinations. To investigate all these combinations experimentally is very time-consuming, reliable CFD calculations can help to assist particle erosion investigations. For this purpose, robust and trustworthy models which describe the particle wall interaction are needed.

Exemplary, one CFD study is presented here in detail. The study is a recent work by Sedrez et al. (2019) from the Erosion/Corrosion Research center in Tulsa, USA. Sedrez et al. (2019) compare their CFD simulations with their own experiments. The experimental set-up is described in detail in chapter 5.3. The investigated domain is a piping system with two consecutive 90° elbows, but only the erosion of the first elbow is measured. The geometry is shown in Figure 2.18a. The case conditions are summarized in Table 2.5. The numerical modeling consists of the steps flow modeling, particle tracking, and erosion calculation. The first two steps are described in chapter 3.1.1. As a rebound model, the Grant and Tabakoff model is used (Grant et al., 1975). For the last step, an erosion model is needed. Sedrez

<sup>7</sup>Figures are reused with the permission of the rights owner

**Table 2.5:** Key parameters of the numerical and experimental investigation from Sedrez et al. (2019)

<b>Geometry</b>	
Typ	elbow
Bend angle	90°
Inner diameter $D_i$	50.8 mm
Bend radius $R_b$	76.2 mm
<b>Conditions</b>	
Fluid	water
Liquid mass flow	12.8 kg/s
Particle	sand
Particle diameter (mean)	300 $\mu\text{m}$
Particle density	2650 kg/m <sup>3</sup>
Particle mass flow	0.1285 kg/s
Particle volume concentration	0.37 %
<b>Code</b>	
ANSYS FLUENT 17.2	

**Table 2.6:** Material coefficients for stainless steel

Material	$C_1$	$C_2$	K	$U_{tsh}$ [m/s]
Stainless steel 316	$4.58 \times 10^{-8}$	$5.56 \times 10^{-8}$	0.4	5.8

et al. (2019) adopted the model developed by Arabnejad et al. (2015):

$$ER_c = \begin{cases} C_1 \frac{u_p^{2.41} \sin\theta [2K \cos\theta - \sin\theta]}{2K^2}, & \theta < \tan^{-1} K \\ C_1 \frac{u_p^{2.41} \cos^2\theta}{2}, & \theta > \tan^{-1} K \end{cases} \quad (2.45)$$

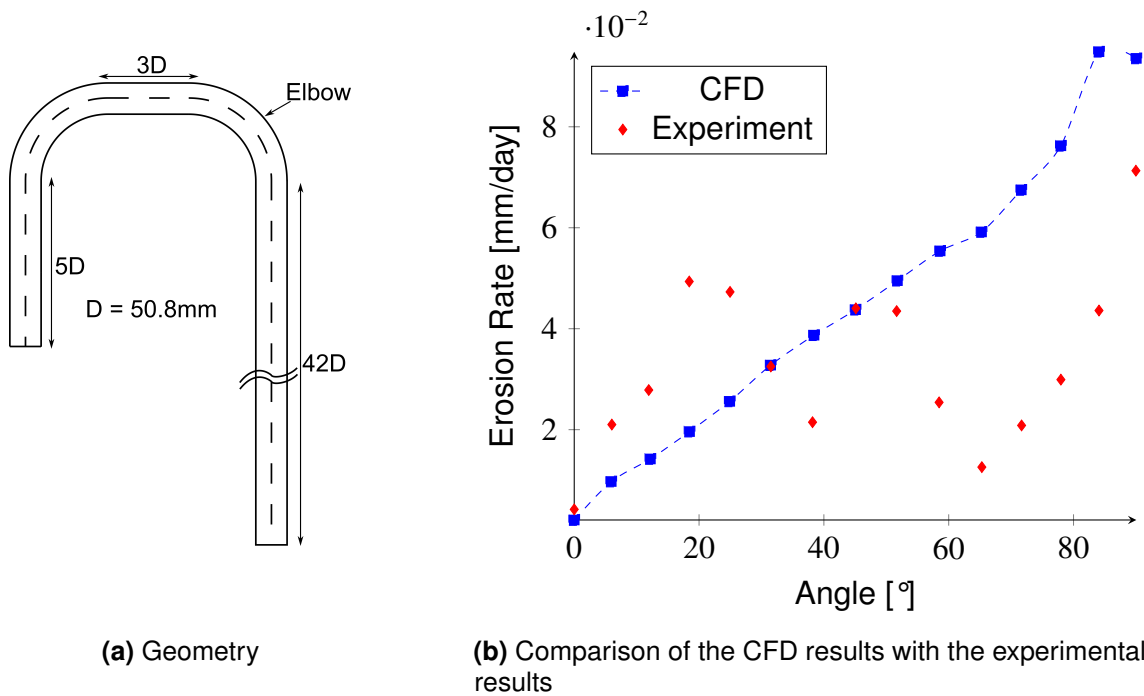
$$ER_D = C_2 (u_p \sin\theta - U_{tsh})^2 \quad (2.46)$$

$$ER_{tot} = ER_c + ER_D \quad (2.47)$$

where  $ER_c$  is the cutting erosion,  $ER_D$  the deformation erosion,  $u_p$  the particle velocity, and  $\theta$  the particle impact angle. The coefficients  $C_1$ ,  $C_2$ , K, and  $U_{tsh}$  are empirical constants. The coefficients for stainless steel 316 are shown in Table 2.6.

The CFD calculation was calculated with a steady state approach with a mass flow inlet and a pressure outlet. The particles are released uniformly at once at the inlet and are considered as non-spherical. It is assumed that the particles do not effect the fluid (one-way coupling).

The experimental and simulation results are shown in Figure 2.17. The experimental result measures a maximum erosion at 90° (0.18 mm/day) with different sub-peaks in other regions. The simulation also predicts the maximum erosion at 90°. The calculated results are given in kg/m<sup>2</sup>s. The corresponding wall loss at 90° is 0.1 mm/day, which matches well with the measured 0.12 mm/day. In contrast to the experimental results, the numerical results show no sub peaks at different bend



**Figure 2.18:** Geometry and Comparison of the CFD and experimental results from Sedrez et al. (2019)

angles. For the numerical prediction, there is a constant rise from the beginning to the end of the bend as Figure 2.18b shows.

Sedrez et al. (2019) concluded that the CFD calculation is able to predict the location of highest erosion well, and also quantitatively, the wall loss is predicted well. The difference in the erosion patterns is led back to the experimental time: With much more experimental time, it is expected that the uniformly increasing erosion profile could be achieved.

### 2.4.3 Heavy Liquid Metal Erosion

Compared to other corrosion systems like water or gas systems (with and without particles), there are less investigations for heavy liquid metal systems because in the past these systems were less relevant than water or gas systems for the industry. Nevertheless, there are studies which deal with FAC problems in lead alloy systems. A good overview of the important mechanisms for these systems and how FAC could be described in lead alloys is given by Balbaud-C  lerier's group in several different works over the years ((Balbaud-C  lerier and Barbier, 2001) (Balbaud-C  lerier et al., 2002) (Balbaud-C  lerier and Terlain, 2004) (Balbaud-C  lerier and Martinelli, 2010)). The fluids of interest in this works were LBE, lead, and a lead-lithium alloy (Pb-17Li). The corrosion rate depends on the type of steels which are exposed to lead or LBE and on the concentration of oxygen in the fluid. With much oxygen dissolved, a protective oxide layer could be formed on the surface which protects it from further corrosion. In Balbaud-C  lerier and Barbier (2001), only the process for low oxygen levels are discussed, so no oxidation happens, and the corrosion happens by dissolution of the steel components.

Assuming the process in the mass transfer region (cf. Figure 2.1a), the general mechanism of the process does not differ from other fluids. Like before, the corrosion rate can be expressed with equation 2.1, e.g. as a function of MTC and the concentration difference. That means that suitable correlations for the MTC have to be found to estimate the corrosion rate in heavy liquid metal system. In dimensionless form, the MTC can be expressed with the already in equation 2.2 presented Sherwood number. With the help of dimensional analyses, it can be shown that the Sherwood number is a function of Reynolds number and Schmidt number (equation: 2.3):

$$Sh = aRe^bSc^c \quad (2.48)$$

The coefficients a, b, and c are empirical which have to be determined experimentally.

For pipe flows, Balbaud-Célérier and Barbier (2001) investigate three different existing MTC correlations and whether they are suitable for their application in heavy liquid metal pipe flows. The first correlation is the Berger and Hau correlation (Berger et al., 1977):

$$MTC_{B-H}[m/s] = 0.0165u^{0.86}D_i^{-0.14}\nu^{-0.53}D^{0.67} \quad (2.49)$$

The experiments were done in a fully developed flow with  $8 \times 10^3 < Re < 2 \times 10^5$  and Schmidt numbers  $1000 < Sc < 6000$ .

The second investigated correlation is the correlation from Harriott et al. (1965). It is a correlation which was done for Reynolds numbers between  $1 \times 10^4$  and  $1 \times 10^5$  and Schmidt numbers between 430 and  $1 \times 10^5$ :

$$MTC_{H-H}[m/s] = 0.0096u^{0.913}D_i^{-0.087}\nu^{-0.567}D^{0.654} \quad (2.50)$$

The last correlation is the correlation by Silverman (Silverman, 1984) (Holser et al., 1990). It is a correlation for high Schmidt numbers and Reynolds number up to  $1 \times 10^5$ .

$$MTC_{Silverman}[m/s] = 0.0177u_\tau^{0.875}D_i^{-0.125}\nu^{-0.579}D^{0.704} \quad (2.51)$$

where  $D_i$  is the inner diameter of the pipe in m,  $\nu$  the kinematic viscosity in  $m^2/s$ , and  $D$  the diffusion coefficient in  $m^2/s$ . In contrast to Silverman's correlation, the other correlations are dependent on the flow velocity  $u$ , whereas the correlation of Silverman is dependent of the friction velocity  $u_\tau$ :

$$u_\tau = \sqrt{\frac{\tau_w}{\rho}} \quad (2.52)$$

This is interesting, because with the friction velocity, a local quantity is taken into account, which means this could be a correlation which could be used for other situations than only pipes.

For estimating the corrosion rate with equation 2.1, the material properties of the diffusion coefficient  $D$ , the kinematic viscosity, and the concentration difference have to be known. The assumption was made that the bulk concentration is negligible, and the concentration at the wall is at saturation concentration. The difficulty for the heavy liquid metal systems is that the properties, like diffusion coefficient of

**Table 2.7:** Correlation results in a pure lead pipe flow (Balbaud-C  lerier and Barbier, 2001)

Conditions		Results	
Temperature	600 �C	MTC <sub>B-H</sub>	$6.22 \times 10^{-5}$ m/s
Velocity	0.42 m/s	MTC <sub>H-H</sub>	$6.73 \times 10^{-5}$ m/s
Inner diameter D <sub>i</sub>	0.01 m (estimated)	MTC <sub>Silverman</sub>	$6.59 \times 10^{-5}$ m/s
<b>Properties</b>		R <sub>c,B-H</sub>	$1.56 \times 10^{-3}$ g/m <sup>2</sup> s
Kinematic viscosity $\nu$	$1.545 \times 10^{-7}$ m <sup>2</sup> /s	R <sub>c,H-H</sub>	$1.69 \times 10^{-3}$ g/m <sup>2</sup> s
Diffusion coefficient	$1.15 \times 10^{-9}$ m <sup>2</sup> /s	R <sub>c,Silverman</sub>	$1.65 \times 10^{-3}$ g/m <sup>2</sup> s
D <sub>Fe in Pb</sub>		<b>Wall loss rate</b>	
Schmidt number	134	$\frac{dh}{dt}$ <sub>B-H</sub>	6255 �m/year
Solubility of iron	25.1 g/m <sup>3</sup>	$\frac{dh}{dt}$ <sub>H-H</sub>	6627 �m/year
		$\frac{dh}{dt}$ <sub>Silverman</sub>	6668 �m/year

iron in LBE or saturation concentration of iron in LBE, are not completely known yet (Balbaud-C  lerier and Martinelli, 2010).

Table 2.7 shows a comparison of all three correlations with an experimental investigation in pure liquid lead. In the experimental investigation, pure lead circulated with  $u = 0.42$  m/s at 600  C, with a measured wall loss of 2600  m/year. As it can be seen, the three equations predict similar wall losses. They all overestimate the wall loss by a factor of approximately 2.4. The reasons for the systematic overestimation could be the assumption of saturated concentration and/or the negligence of the bulk concentration. Also, the Schmidt number with 134 is lower than the given range for the correlations. Nevertheless, according to Balbaud-C  lerier and Barbier (2001) the prediction is in a reasonable range.

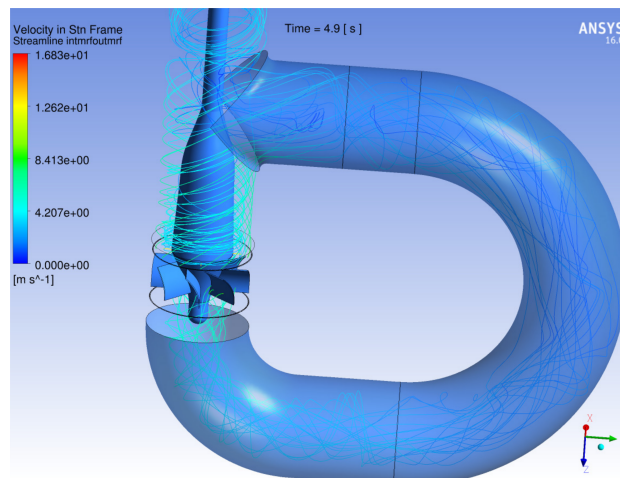
#### 2.4.4 Centrifugal Pumps with Liquid Metal as a Working Fluid

Centrifugal pumps have a long history, and therefore, there are countless of experimental and numerical investigations concerning all aspects of centrifugal pumps. A good introduction and overview on centrifugal pumps is given by G  lich (2014a), and a review for numerical studies is given for example by Pinto et al. (2017).

In contrast to the broad range of centrifugal pump investigations, there are only a few investigations concerning heavy liquid metal pumps. Until now, liquid metals are promising working fluids, but they are not common in industry applications at the moment. Due to that, the fundamental research in this field is done in a smaller scale at universities. There the liquid metal loops have lower flow rates and no need to work as efficient as possible but should work with low maintenance. Hence, there is not a great need for mechanical pumps, and the small loops can be driven by induction pumps with no moving parts and sealing problems.

The closer an industrial use of liquid metals comes, the more interesting the investigation of mechanical pumps gets. The pumps have to operate under challenging conditions - they have to withstand high temperatures and corrosive media. Amy et al. (2017), for example, presented in their work a prototype mechanical pump out of a ceramic which is able to pump tin at 1600 K. To achieve that, the mechanical and sealing components were made of ceramics which are able to



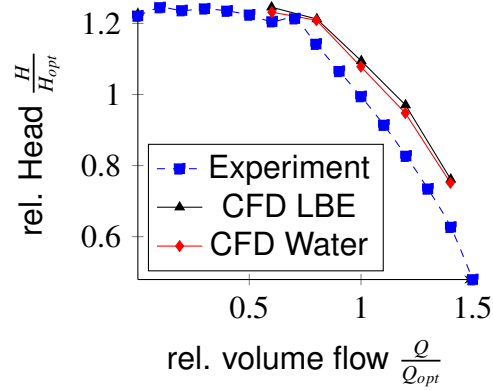


**Figure 2.19:** Computational domain of Borreani et al. (2017) with path lines of the flow <sup>8</sup>

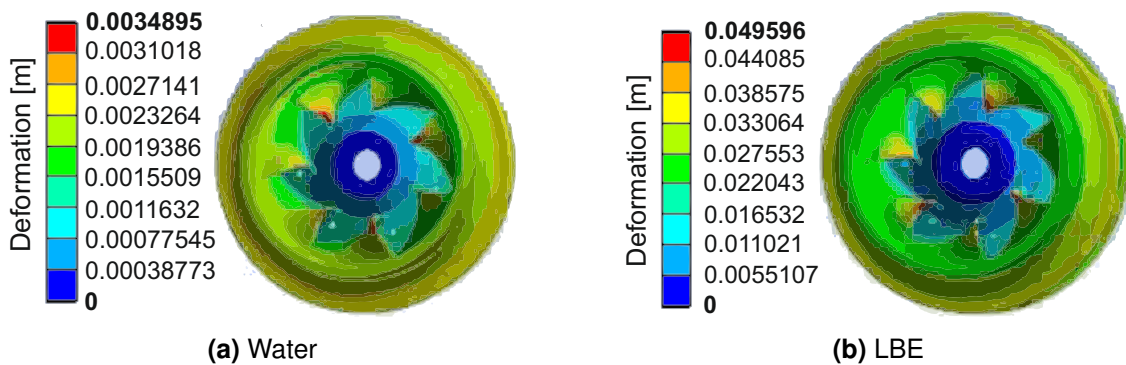
withstand these temperatures but even this special material suffers of visible wear after 72h of pumping (Amy et al., 2017). According to the authors, there is a high potential to minimize the wear rates in the future and that this was essentially a proof-of-concept demonstration.

A technical application of interest for heavy liquid metals is for sure the Lead cooled Fast Reactor (LFR). In these systems lead and LBE are both considered as working fluids. The challenges of the primary circulation pump in a LFR are mentioned in Alemberti (2015). To avoid unacceptable erosion phenomena, the fluid velocity is restricted in the whole system to 2 m/s, except for the area of the blades, where 10 m/s are allowed because of the use of special materials. This group investigates possible pump designs for the Generation IV LFR on the basis of the requirements of the Advanced Lead Fast Reactor European Demonstrator (ALFRED) design (Borreani et al., 2017) (Lomonaco et al., 2016). It is a numerical investigation, and the investigated pump designs were a jet design, archimedean pump, and the blade pump. In the course of the investigation, the blade pump shows the best performance. The configuration of the pump was a flow rate of 2200 m<sup>3</sup>/h and a head of 1.5 m. Due to the high flow rate and low head, the blade pump was designed as a semi-axial pump based on the design of Gülich (2014a) with geometrical adaption, so that the velocity does not exceed the critical velocity. The computational domain can be seen in Figure 2.19. The pump is located in a straight pipe linked to a piping system with a u-profile. The outlet of the computational domain would lead to the steam generators. The simulation was done with the Multiple Reference Method (MRF) approach like the pump simulations in this work. The MRF zone is indicated with the black lines under and above the blades. This approach is described in chapter 3.1.2. The authors suppose that, due to the swirled flow after the blade combined with the T-junction, the flow enters the steam generators disturbed, and this problem should be addressed in the future, but for the general performance it is convincing compared to the other designs.

<sup>8</sup>Borreani et al. (2017) published under an open access licence, which permits the reuse.



**Figure 2.20:** Comparison between numerical and experimental results by Ma et al. (2016)



**Figure 2.21:** Deformation contours at the  $Q_{opt}$  flow rate (Ma et al., 2016)<sup>9</sup>

Another mechanical pump investigation with LBE as a working fluid was done by Ma et al. (2016). The target of this work was the numerical stress analysis of a centrifugal pump impeller with a consecutive one-way fluid to solid coupling. With this fluid-solid coupling, the deformation, respectively, the displacement of the blades, caused by the fluid forces, are calculated. The numerical set-up was similar to the set-up above or with the set-up used in this work. The MRF approach was used for the rotation, and as a turbulent model, the  $k-\omega$ -SST model was used. The validation was done by comparing the numerical results of water and LBE as working fluids with experimental results, where water at room temperature was used. The results for the head can be seen in Figure 2.20. As it can be seen, the numerical results for water and LBE are close to each other. The numerical results overestimate the experimental findings. In Figure 2.21, the deformation distributions for water and LBE can be seen at the design point. The maximum deformation can be found for both fluids in the middle of the leading edge. The maximum deformation for LBE is around 14 times higher than the calculated deformation for water.

<sup>9</sup>Ma et al. (2016) published under an open access licence, which permits the reuse.

# 3. General Strategy for a Trustworthy CFD Simulation

The aim of this chapter is to describe how the CFD calculations are done for this work and what the governing equations for the different cases are. It summarizes exemplarily what was done for each case.

For modelling the FAC processes in this work, WSS was chosen as the key parameter. Hence, section 3.2, and in parts section 3.3, mainly deal with this parameter. As the velocity field is the main key parameter for particle erosion modelling, this parameter was considered in these cases.

## 3.1 Computational Model

This section serves the purpose to describe the computational models which were used in this study. As a base solver for all simulations, the SIMPLE algorithm (Caretto et al., 1973) in form of the simpleFoam Solver from OpenFOAM (Version OpenFOAM v3.0+ up to OpenFOAM v1906) was used to solve the pressure velocity coupling. This solver is suitable for steady state incompressible and turbulent flows. Therefore, all studies from this work were treated as steady state problems with flow conditions clearly in the turbulent regions. The fluids were considered as incompressible, which is a good assumption for all liquids. In addition, this study treats the fluids as isothermal, which reduces the governing equations to the continuity and the momentum equation. The continuity equation for a steady state case and an incompressible fluid is

$$\nabla \cdot \vec{U} = 0 \tag{3.1}$$

while the momentum equation is

$$\nabla \cdot (\vec{U} \otimes \vec{U}) = \nu \nabla \cdot \nabla \vec{U} - \nabla \left( \frac{p}{\rho} \right), \tag{3.2}$$

where  $\vec{U}$  is the velocity vector,  $\nu$  the kinematic viscosity of the fluid,  $p$  the pressure, and  $\rho$  the fluid's density. From the momentum equations, it becomes clear that the incompressible simpleFoam-solver only needs the kinematic viscosity of a fluid as

a material property for the calculation. As stated before, the kinematic viscosity is defined by

$$\nu = \frac{\mu}{\rho} \quad (3.3)$$

where  $\mu$  is the dynamic viscosity and  $\rho$  is the density. Therefore, every quantity, which is somehow related to the kinematic viscosity, is divided by the density. For example, OpenFOAM calculates the pressure in  $\text{m}^2/\text{s}^2$  ( $\frac{\text{Pa} \cdot \text{m}^2}{\text{kg}}$ ) instead of the SI-unit pascal. Therefore, the pressure has to be multiplied with the density of the fluid in a post-processing step, if there is a need for a pressure field in pascal.

The Reynolds averaged Navier Stokes (RANS) based k- $\omega$  SST model is used for taking the effects of turbulence into account (Menter, n.d.). The k- $\epsilon$  turbulence model and the SSG Reynolds stress model were also tested in a 90° elbow but the SST model was found to be the most suitable because of its good behavior in near wall regions and its robustness. For the wall treatment, basic wall functions and no wall functions, dependent on the  $y^+$ , were used.

#### 3.1.1 Particle Calculation

For particle erosion modeling, it is necessary to simulate the particle tracks inside the flow. Hence, simpleFoam can not be used as a sole solver in that case, it has to be combined with a second solver which is suitable for this kind of task. Therefore, a turbulent steady state CFD calculation is performed with the simpleFoam solver in a first step to get the flow field. In a second step, the particle motions are calculated with a time-dependent, so called Lagrangian, simulation. As a Lagrangian solver, the UncoupledKinematicParcel-FOAM solver was used. It is a Lagrangian solver for one-way coupling. One-way coupling means that the fluid influences the particle tracks but the particles do not influence the flow field of the fluid. If they would, it would be two-way coupling. Compared to one-way coupling, two-way coupling would lead to a huge increase of computational time due to the fact that after every Lagrangian time step the flow field has to be recalculated. The decision which coupling is necessary, is made by the value of  $\beta$ , which is defined as

$$\beta = \frac{\text{particle mass per volume}}{\text{fluid mass per volume}} = \frac{r_p \rho_p}{r_f \rho_f} \quad (3.4)$$

where  $\rho$  is the density of the particle (p), respectively, of the fluid (f) and  $r$ , in that case, the volume fraction of the involved phases. The critical value for  $\beta$  is 0.2. For higher values, two-way coupling is suggested. From equation 3.4, it becomes clear that beta reaches high values, if the density difference between the particle and fluid is high and/or the volume fraction of the particle is high. In the investigated cases, the value for  $\beta$  is far below that critical value. The governing equation for Lagrangian particle simulations is Newtons second law:

$$\sum F_i = m_p \frac{du_p}{dt} \quad (3.5)$$

$$u_p = \frac{dx_p}{dt} \quad (3.6)$$

### 3. General Strategy for a Trustworthy CFD Simulation

where  $m_p$  is the mass,  $u_p$  the velocity,  $x_p$  the location of the particle,  $t$  the time, and  $\sum F_i$  is the sum of all forces which act on the particle. One of the most important forces, which has to be considered, is the drag force

$$F_D = C_D \frac{\pi D_p^2}{8\rho_f} (u_f - u_p) |u_f - u_p| \quad (3.7)$$

where  $C_D$  is the drag coefficient, which has to be defined by existing correlations, and  $D_p$  the diameter of the particle.

Another important aspect for the trajectory of a particle is the rebound of the particle from the boundary wall. The model has to calculate the particle's velocity vector after an impact on a wall. The wall tangential (t) and wall normal (n) component of the velocity after the impact (a) are calculated with:

$$u_{n,a} = u_{n,b} - (1 + e_n) u_{n,b} \quad (3.8)$$

$$u_{t,a} = u_{t,b} - e_t u_{t,b}. \quad (3.9)$$

As the equations show, the velocity components are multiplied with restitution coefficients  $e_n$  and  $e_t$ . Experimental investigations have shown that the restitution coefficients depend on the particle impact angle on the involved materials. The results shown in this work use the particle rebound model of Forder et al. (1998).

#### 3.1.2 Pump Calculation

For pump calculations, the described standard case set-up from above can be used with one addition: To handle the rotation of the impeller, this work uses the so called MRF method, also known as the frozen rotor approach. For this method, no actual moving mesh is needed, which reduces the computational time. The general idea is that the rotating zone is solved in a different reference frame than the stationary zone. In the rotating zone, the Coriolis force is added to the momentum equation and the flux is calculated with the relative velocity. The governing equations for the rotating zone can then be written as (Sig Turbomachinery, 2009)

$$\nabla \cdot \vec{U}_R = 0 \quad (3.10)$$

and

$$\nabla \cdot (\vec{U}_R \otimes \vec{U}_I) + \underbrace{\vec{\Omega} \times \vec{U}_I}_{\text{Coriolis force}} = \nu \nabla \cdot \nabla \vec{U}_I - \nabla \left( \frac{p}{\rho} \right). \quad (3.11)$$

In equation 3.10 and 3.11, the subscripts R and I stand for rotating and inertial, respectively.  $\Omega$  represents the angular velocity. The separation of the zones in a rotating and a stationary frame can be seen in Figure 3.1.

For the boundary conditions at the inlet, a flow rate was given and the pressure was set to a fixed value at the outlet. Due to this, the internal pressure of the pump adapts to this fixed value, but for the calculation of the pump head, only the pressure difference is needed.

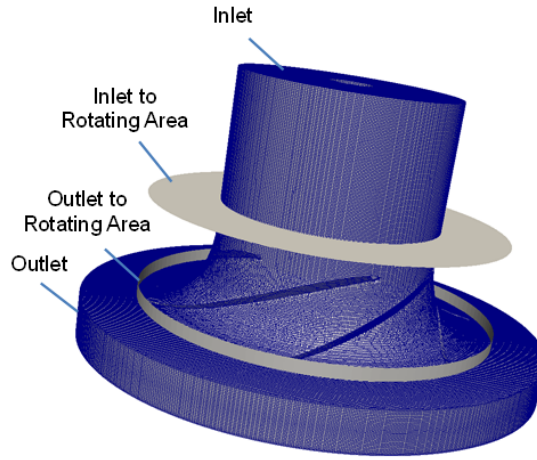


Figure 3.1: The different sections of the calculation zones.

## 3.2 CFD Simulations in Pipes

### 3.2.1 Preconditioning

As inlet condition, a pre-calculated fully developed turbulent velocity field is taken. A flow needs a certain distance to become fully developed. Even if a uniform inlet profile is considered, a developed flow is reached only after a certain distance from the inlet. The theoretical hydrodynamic developing length  $L_H$  for turbulent flows differs from source to source. For turbulent flows, this length is often considered as constant (Nikuradse, 1932) (Brauer, 1971) or with only low influence (Kleuker et al., 1993) of the Reynolds-number. The stated length varies from

$$\frac{L_H}{d} = 25 \text{ to } 100. \quad (3.12)$$

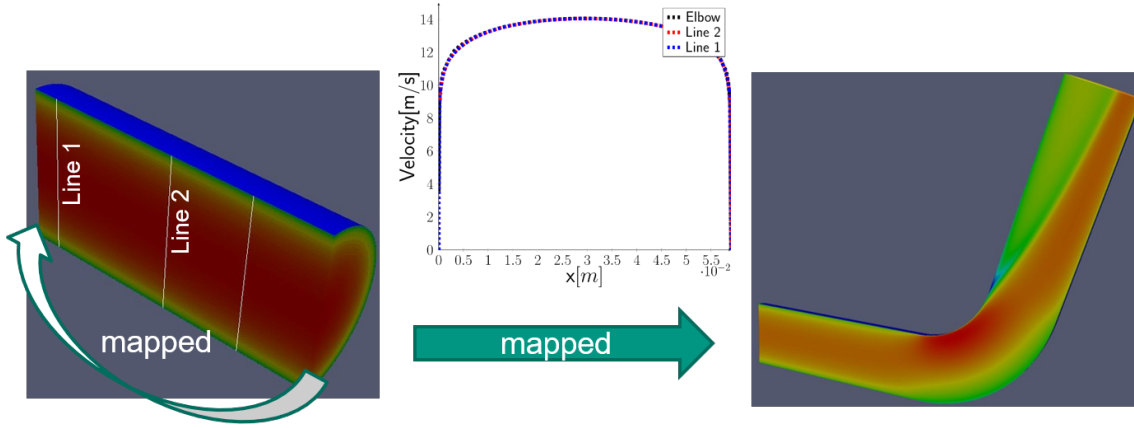
This large range can be led back to different inlet conditions of the different studies. To avoid these uncertainties and a unnecessary large computational domain, but to make sure that the flow is developed, a short pipe is simulated. Here, the values of the outlet are mapped to the inlet until the calculation is converged. In other words: With this approach, a segment of an infinite long pipe is calculated, and a fully developed flow is automatically achieved. In a second step, the values are mapped to the proper computational domain. The overall procedure can be seen in Figure 3.2. Also the velocity profiles in the pipe segment and at the inlet of an elbow are depicted to make sure that the flow is fully developed.

### 3.2.2 Mesh Sensitivity Study

As described in chapter 2.1, the most important quantity for modeling FAC erosion is the WSS  $\tau_w$ . Hence, a reliable distribution of  $\tau_w$  has to be achieved during the CFD simulation. The WSS is defined as

$$\tau_w = \nu \rho \frac{\partial u_x}{\partial y} \Big|_{y=0} \quad (3.13)$$

### 3. General Strategy for a Trustworthy CFD Simulation



**Figure 3.2:** Preconditioning of the CFD calculation for a fully developed flow.

where  $\nu$  is the kinematic viscosity and  $\rho$  the density of the fluid. The quotient  $\frac{\partial u_x}{\partial y}|_{y=0}$  is the gradient of the tangential velocity ( $u_x$ ) normal to the wall at the wall ( $y = 0$ ). From equation 3.13, it becomes clear that the velocity profile near the wall is the most important factor for predicting the WSS in a CFD simulation. This leads to the assumption that the mesh resolution at the wall is a key factor for a mesh sensitivity study.  $\tau_w$  is taken as the target quantity on which basis it is decided if a mesh's independency is reached. Normally, meshes in the near wall region are described with a so called  $y^+$  value. It is a dimensionless distance of the first mesh node to the wall and is defined as

$$y^+ = \frac{y u_\tau}{\nu} \quad (3.14)$$

where  $y$  is the distance to the nearest wall and  $u_\tau$  the friction velocity and it is defined as

$$u_\tau = \sqrt{\frac{\tau_w}{\rho}}. \quad (3.15)$$

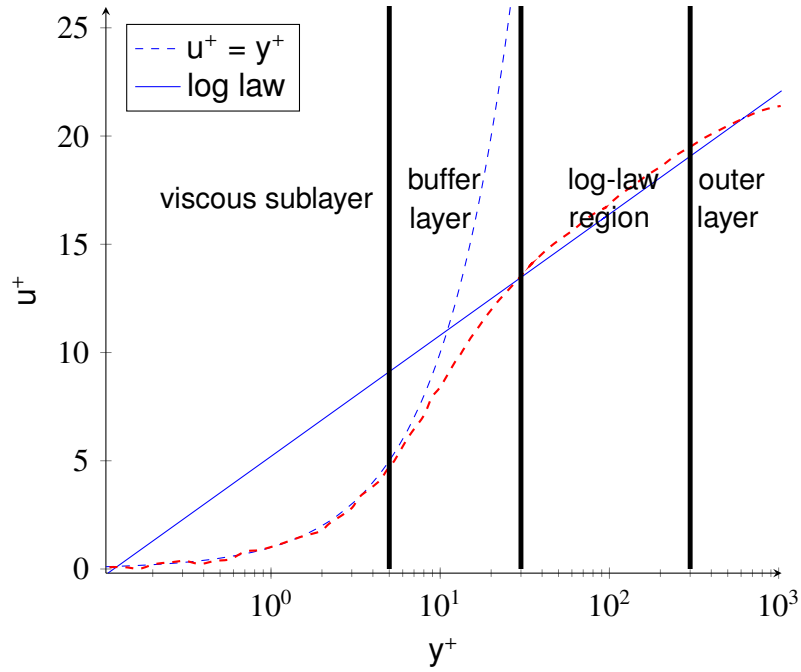
Analogous to  $y^+$ , the dimensionless velocity  $u^+$  is introduced:

$$u^+ = \frac{u_x}{u_\tau}. \quad (3.16)$$

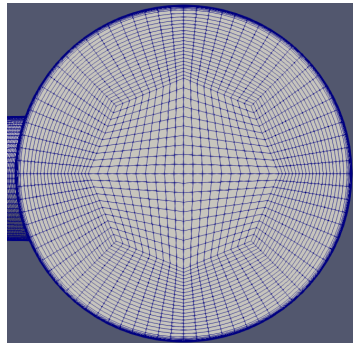
The relation between  $u^+$  and  $y^+$  can be seen in Figure 3.3. This figure shows the so called law of the wall. The diagram shows that the flow can be divided in different layers. The first is the viscous sublayer, where  $u_\tau$  is nearly equal to  $y^+$ . This layer is located below 5 for  $y^+$ . The buffer layer lies between  $y^+ > 5$  and  $y^+ < 30$ . The buffer layer is a transition layer between the viscous sub layer and the log-law region which goes up to a  $y^+$  value of around 300 (Wilcox, 1993). These three layers together form the inner layer. According to the practice rules of turbulence modeling,  $y^+$  value should avoid the buffer layer. For calculations without wall functions, the SST model suggest a  $y^+$  below 1 and between 30 and 300 when wall functions are used (Wilcox, 1993).

Figure 3.4 shows an exemplary mesh for the simulations. It was generated with the open source software Salome, a software for pre- and post-processing for

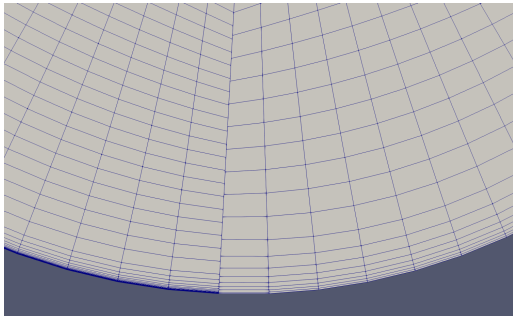
### 3. General Strategy for a Trustworthy CFD Simulation



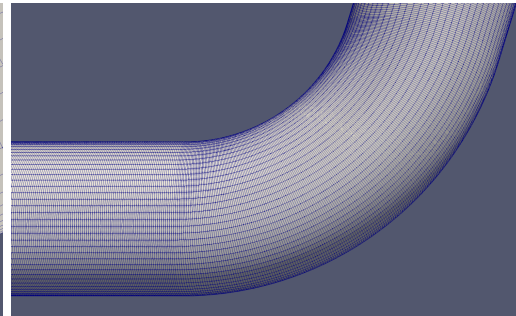
**Figure 3.3:** The Law of the wall with the relation between  $u^+$  and  $y^+$  (according to Wilcox (1993)).



**(a)** Radial mesh resolution



**(b)** Mesh comparison in the wall near region for  $y^+$  below 1 (left) and 180 (right)



**(c)** Mesh resolution in axial direction

**Figure 3.4:** Meshes for the Mesh sensitivity study .



### 3. General Strategy for a Trustworthy CFD Simulation

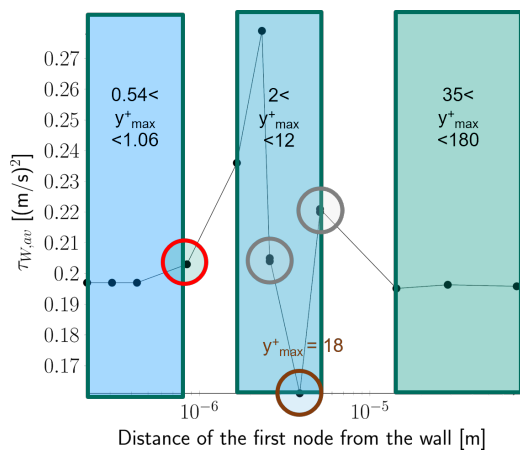
---

numerical simulations. In Figure 3.4a, the overall radial mesh structure can be seen. An octagon is defined for the core region of the flow with a relatively coarse mesh. Between this octagon and the wall region, a mesh with uniform layers is placed. A detailed view of the mesh near the wall can be seen in Figure 3.4b: Fine layers of different sized layers grow from the wall. For the mesh study, mainly the number and overall size of these layers were changed. The figure is divided into two parts: On the left side, a mesh is shown with a  $y^+$  value below 1 and on the right side, a mesh with a  $y^+$  value of around 180 is depicted. In Figure 3.4c, the axial resolution of the mesh is shown. In axial direction, the mesh is equally spaced over the whole computational domain but can be refined easily with Salome in the elbow region if necessary.

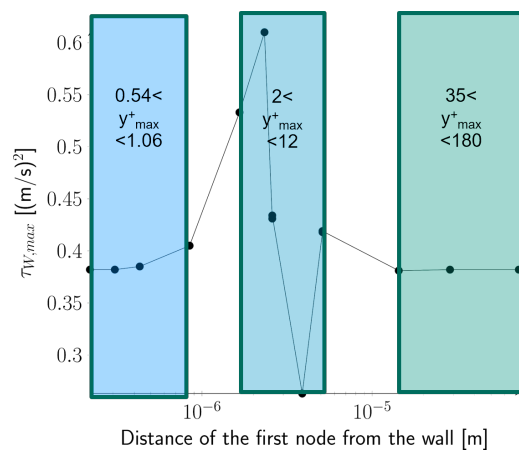
From equation 3.15, it becomes clear that the WSS has a direct influence on  $y^+$ . A simulation which under- or overpredicts the WSS, would influence the  $y^+$ . So, a traditional  $y^+$  mesh study would not be constructive. Hence, the study was carried out by varying the wall distance  $y$  and calculating the  $y^+$  value afterwards. Figure 3.5 shows the WSS as a function of  $y$ . As described in section 3.1, units are written as a function of the density of the fluid, therefore the unit of  $\tau_w$  is given in  $(\text{m/s})^2$  in the diagrams instead of  $\text{N/m}^2$ . In Figure 3.5a, the averaged WSS against the wall distance  $y$  is shown, in Figure 3.5b the maximum WSS, and in 3.5c the minimum WSS. In these diagrams, the values of  $y$  and  $y^+$  are also set into perspective: The blue range of  $y^+_{\text{max}}$  shows the results for  $y^+_{\text{max}}$  below 1, this range is calculated without wall functions. The light blue range of  $y^+_{\text{max}}$  are the results of  $y^+_{\text{max}}$  calculations between 2 and 12. The gray circles indicate that these cases were calculated with and without wall functions. The brown circle shows the problem from above that  $y^+$  and  $\tau_w$  are functions of each other. There, the  $y^+$  value is higher (18) than the neighbor to the right (12) even if the distance to the wall is lower. In this range, the results are varying extremely and no trend can be found. With the  $y^+$  calculation, it turned out that this is the buffer layer which should be avoided. The dark green area is the range of  $y^+_{\text{max}}$  between 35 and 180, this range was calculated with wall functions. As it can be seen from these figures, the averaged and maximum  $\tau_w$  in the blue and the dark green area are steady and consistent. Only for the minimum value of  $\tau_w$ , the calculation needs to be below 1 to stabilize, but, as described early in this chapter, high values of  $\tau_w$  are most critical for the erosion. Due to that fact and to reduce computational time in most cases, it is sufficient to use meshes with a  $y^+$  in the dark green range. The red circle in Figure 3.5a indicates cases with the same radial resolution of the mesh but with different axial resolutions. It becomes clear that the results do not change by making the mesh finer in the axial direction.

To make sure that the simulations not only predict the same values of WSS by coincidence and the WSS distributions are completely different, the distributions were compared and the locations of the minimum and maximum value were identified. The locations of these extreme values are shown in Figure 3.5d. The location of the maximum is at the beginning of the elbow whereas the minimum is at the exit of the bend. All extreme values from the simulations are within the small bubbles displayed in the figure, therefore, it can be concluded with confidence that the simulations predict the right distribution of the WSS.

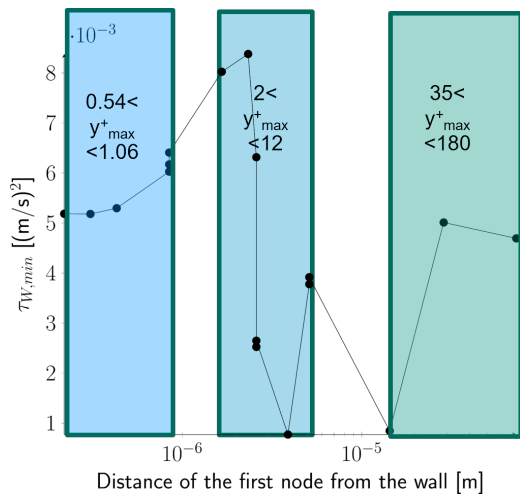
### 3. General Strategy for a Trustworthy CFD Simulation



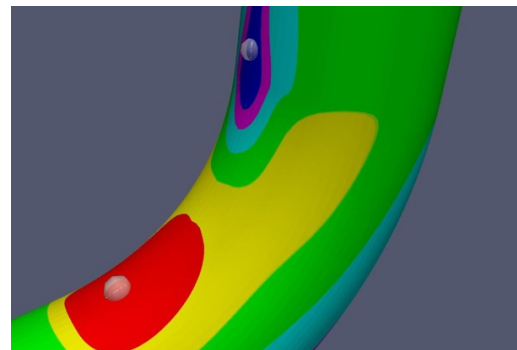
(a) Average WSS in relation to the wall distance of the first node



(b) Maximum WSS in relation to the wall distance of the first node



(c) Minimum WSS in relation to the wall distance of the first node



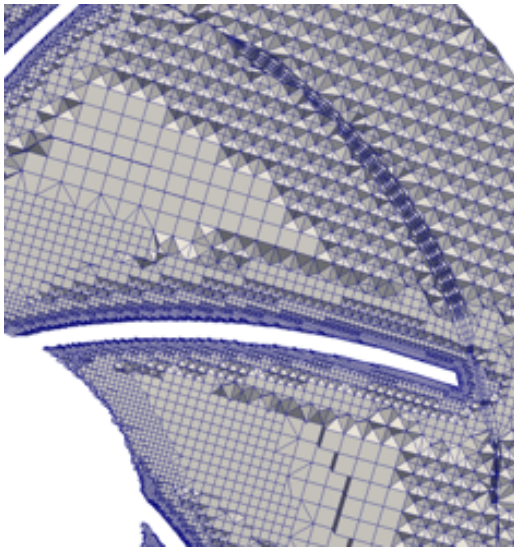
(d) Location of maximum (red) and minimum (blue) WSS

**Figure 3.5:** WSS  $\tau_w$  as a function of the wall distance  $y$  and locations of the extreme values

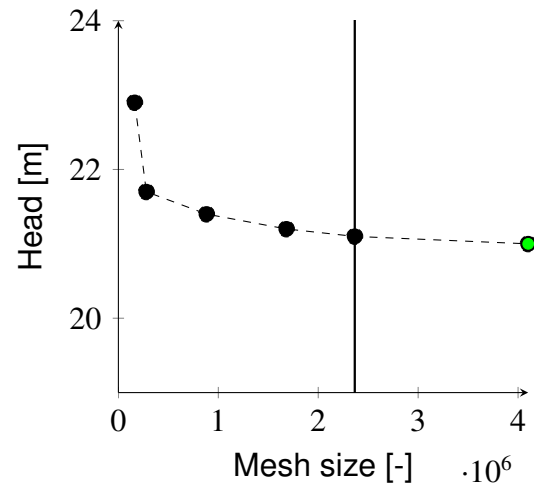
## 3.3 Erosion in Pumps

For pump calculations, a different approach was used due to the more complicated geometry and therefore more complicated mesh generation process. The discretization of the computational domain is done by the OpenFoam tool *snappyHexmesh*. This mesh generator constructs, as the name already suggest, hex dominated meshes. The process of generating a mesh is divided into four steps. In the first step, a background mesh is defined by the user, this mesh enwraps more than the whole calculation area and defines the basic coarseness of the final mesh. Then, *snappyHexmesh* removes all cells which are not entirely part of the calculating area. The remaining cells close to the surface of the calculating area are refined up to a user defined level. The third step is called the snapping process where the mesh points next to the surface are moved exactly to a position on the surface. In the last step, the wall boundary layers can be added to refine these regions further. In this study, the wall regions and especially the blades of the impeller were refined and boundary layers were used. An impression of the used mesh can be seen in Figure 3.6a.

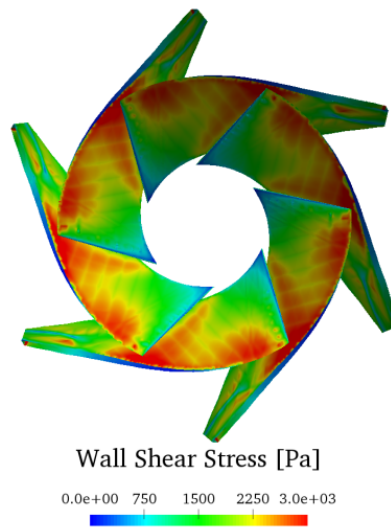
To find an appropriate mesh, a mesh sensitivity study is carried out like in 3.2, but in the case of pump impellers, the more integral value head of the impeller was used as the target value for the grid independence study. The result of this study can be seen in Figure 3.6b. Six meshes with different cell numbers were tested and analyzed. For this mesh study, the same inlet flow rate ( $Q_{opt} = 280 \text{ m}^3/\text{h}$ ) and kinematic viscosity of LBE were used. The mesh size differs from around 0.16 million up 4.1 million cells. For the five smaller meshes, the background mesh was the same, and only the refinement degree at the walls, especially at the blades, differed. The idea is that with this approach, the final mesh is as coarse as possible and only the wall regions are resolved in more detail. To test if the background mesh is too coarse, a sixth mesh with different settings was calculated. This mesh is the one which is marked with a green dot in the diagram. It has the same relative refinement level as the second largest but it starts with finer background mesh. This leads to nearly 2 million more cells but with no change for the head. The head of the impeller does not change much between 2.4 million cells and 4.1 million cells, therefore, and to keep the calculation time reasonable, the 2.4 million cells mesh is used. In general it can be said that producing a mesh with low  $y^+$ -values for LBE leads to very fine meshes at the walls because  $y^+$  is directly dependent on the kinematic viscosity as equation 3.14 indicates. For the LBE calculations, this means that on the blades, the average  $y^+$ -values vary from about 1200 with the first mesh to 220 with the largest mesh. The mesh, which was used for the calculations, provides an average value of 290 at the blades. This value is just in alignment with the needed  $y^+$ -values described in section 3.2, when wall functions are used. Even if this is fulfilled in average, the values are already at the upper limit. In comparison to water as a working fluid, the same mesh has an average  $y^+$ -value of 35. In general, it is challenging to find a suitable mesh for all flow conditions. To calculate a characteristic curve, not only the flow rate at the design point, which leads to different velocity profiles, and therefore to different  $y^+$ -values, but different flow rates have to be calculated. Like in Figure 3.5d, Figure 3.6c is an example of the WSS distribution on pump impeller blades.



(a) Used mesh with coarse inner cells and mesh refinement at the blades



(b) Grid independence diagram



(c) Wall shear stress distribution of a 5bladed impeller

**Figure 3.6:** Pump simulation for a grid independence study

# 4. Erosion Modeling in a Mesh Adapting Framework

The purpose of this chapter is to describe the idea and the approach to model erosion processes. The general idea is shown in 4.1. As it can be seen from this flow chart, the modeling happens in different steps, the main idea is to predict the erosion with the help of local values from a CFD calculation and empirical models. Afterwards, the predicted erosion is used to change the mesh according to the erosion. The single steps will be described in the following and later in chapter 5, the method will be applied and tested for different cases.

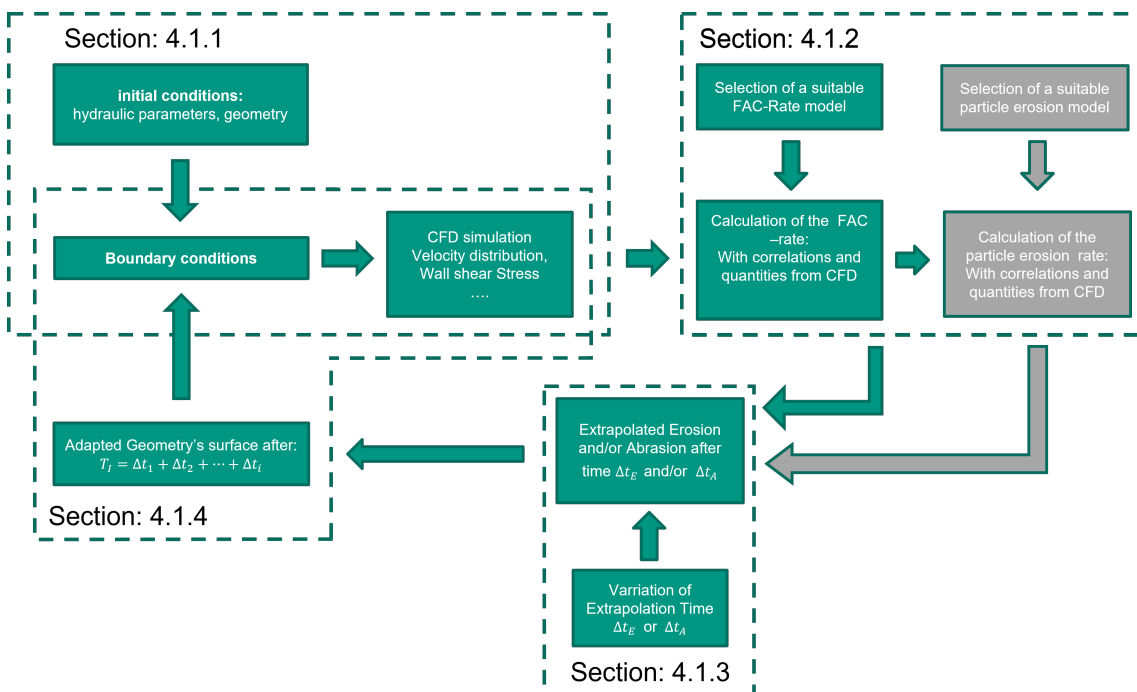
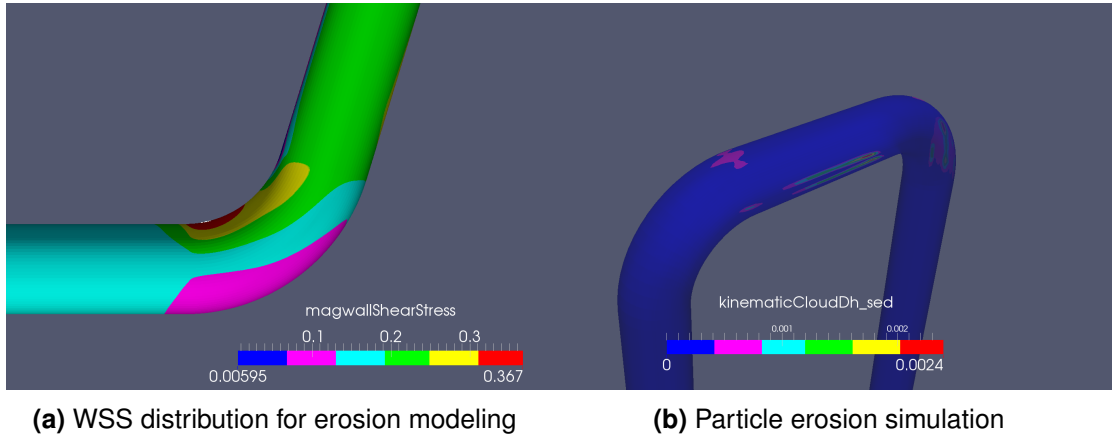


Figure 4.1: General method for modeling erosion

## 4.1 Description of the Method

### 4.1.1 CFD Calculation as Initial Step

At the beginning of the workflow, a robust CFD simulation is needed. For this simulation, the computational fluid domain, which is the object of the investigation



**Figure 4.2:** CFD calculations as initial step

and the case set-up with all the boundary conditions, turbulence models, kinematic viscosity, etc. have to be defined. This initial CFD calculation has to pass the different steps described in chapter 3. For demonstration purpose, initial CFD simulations are shown in Figure 4.2. In Figure 4.2a, the WSS field is shown. This field is needed for the FAC erosion model case. Another model case is a particle erosion case, for this case, also a flow field is calculated, but in an additional Lagrangian step the path of particles through, the computational domain is simulated. The results are shown in Figure 4.2b.

### 4.1.2 Erosion calculation

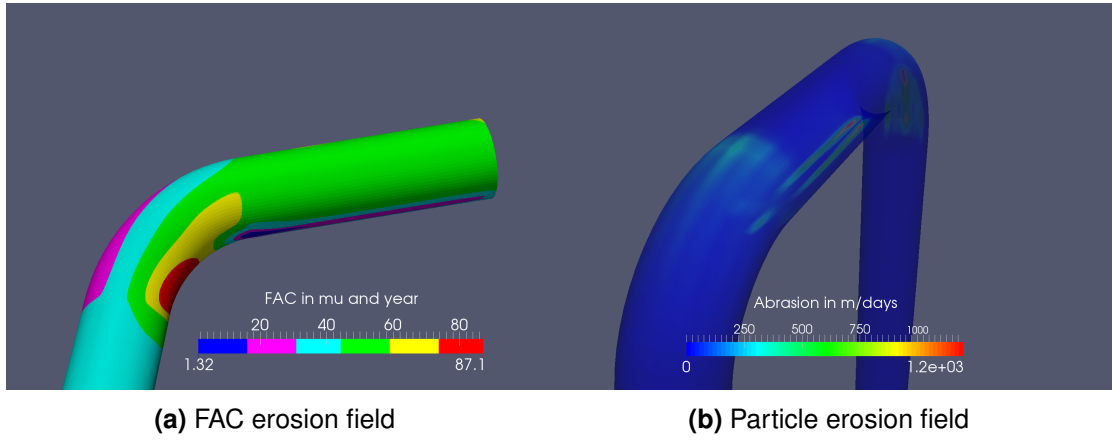
The second step of the workflow is the actual calculation of the erosion, e.g. the wall loss, after a specific time. As described in chapter 2, many different processes are involved when it comes to erosion. Simulating only parts of these chemical processes would not be feasible in an application orientated method. Therefore, to model the erosion, correlations gained from experimental investigations are needed. The accuracy of the modeling depends crucially on the used correlations. In general the FAC rate is defined with equation 2.1:

$$R_C = MTC (C_w - C_B) \left[ \frac{kg}{m^2 s} \right]. \quad (4.1)$$

The mass transfer coefficient (MTC) can be calculated, for example, with the Chilton-Colbrun correlation, which is introduced in chapter 2.1.1:

$$MTC = \left( \frac{\tau_w}{U\rho} S c^{-\frac{2}{3}} \right) \quad (4.2)$$

For this correlation, the WSS is needed and CFD simulations can provide the local distribution of the WSS. In this work, the assumption for the concentration of the corrosion products at the wall is that saturated concentration is reached ( $C_w = C_{sat}$ ) and that there are no products in the bulk ( $C_B = 0$ ). With the calculated MTC and the concentration difference, the erosion rate can be predicted. The erosion rate is given in  $\frac{kg}{m^2 s}$ , this means it represents the material loss per area and time. Hence,



**Figure 4.3:** Wall loss over time

this quantity has to be transferred to a wall loss per time. These quantities are linked via the density of the construction material (Prasad et al., 2018):

$$\frac{dh}{dt} = \frac{R_c}{\rho_s}. \quad (4.3)$$

The results of this consideration can be seen in Figure 4.3a, the wall loss over time caused by FAC erosion.

Another model case is a particle erosion case. The particle erosion models provide the erosion  $E$  in removed construction material mass per particle mass ( $\frac{\text{kg(ConstructionMaterial)}}{\text{kg(Particle)}}$ ). To transfer this quantity to the wall loss per time in the same way, the following equation is used

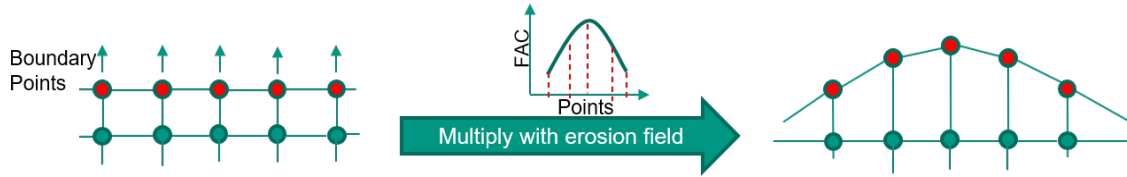
$$\frac{dh}{dt} = \frac{E \dot{m} t}{\rho_s A} \quad (4.4)$$

where  $E$  is the calculated erosion caused by the particles,  $\dot{m}$  is the mass flow of particles impacting onto the boundary wall,  $A$  is the corresponding area of the mesh cell,  $t$  is the time period of particles striking the wall, and  $\rho_s$  is the density of the construction material. The result is the wall loss caused by particle erosion over time and is shown in Figure 4.3b.

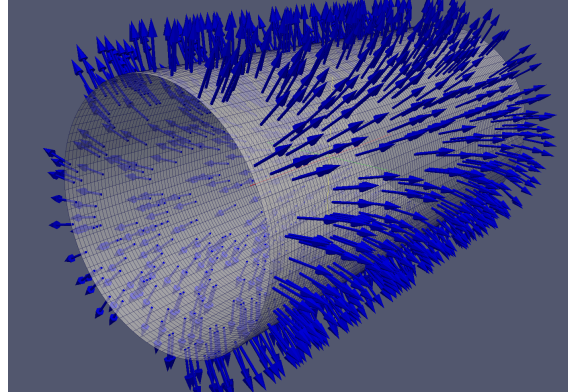
With the fields shown in Figure 4.3, the modeling can proceed to the next step: The deformation of the mesh according to the calculated erosion.

### 4.1.3 Mesh Deformation

The mesh deformation step is the step where the geometry is changed according to the calculated erosion fields in chapter 4.1.2. The procedure scheme of the mesh deformation is shown in Figure 4.4a with FAC erosion as an example. The tool used for deformation is originally based on the OpenFOAM tool *deformedGeom*. This utility was adapted for erosion problems. How the geometry change is done is described in the following. The mesh deformation happens along a unit vector which is normal to the mesh boundary  $\vec{e}_n$ . The unit normal vectors are seen in Figure 4.4b and are 1 micrometer long. They define the direction in which the



(a) Scheme of the mesh deformation process



(b) Wall normals of a pipe

**Figure 4.4:** Mesh Deformation (1)

boundary node will be moved. The magnitude of the movement will be defined by the values of the erosion field at each point and the desired erosion time  $\Delta t_E$ . The positions of the moved points are calculated according following equation:

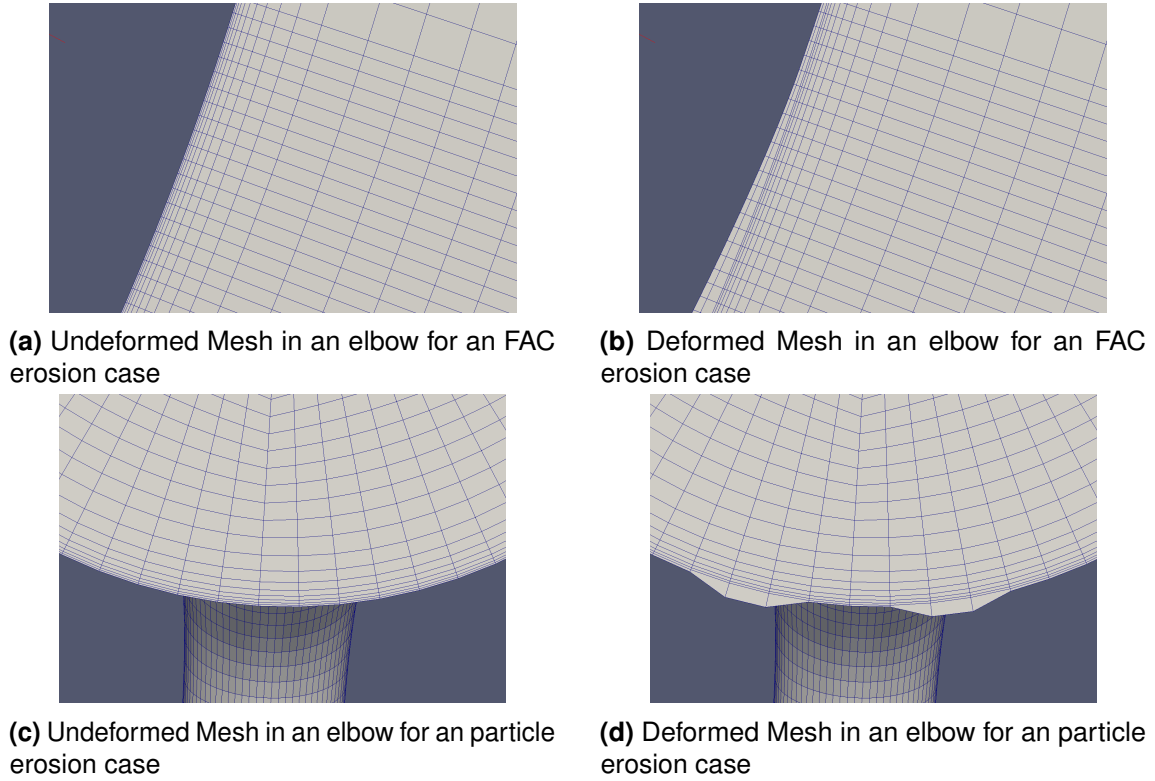
$$\vec{p}_{old} + \vec{e}_n \frac{dh}{dt} \Delta t_E = \vec{p}_{new}. \quad (4.5)$$

The mesh deformation according to the described procedure can be seen for different examples in Figure 4.5a to Figure 4.5d, where the undeformed mesh can be found on the left side, while the deformed mesh is displayed on the right. In the first two pictures of Figure 4.6c, the deformation is shown in detail for three nodes. It can be seen that only the boundary mesh is moved. This leads to a coarser mesh in the near wall region, this problem has to be addressed in a mesh refinement step. This step is described in the section below. In Figure 4.5a and 4.5b, the deformation according to a FAC erosion is shown. In the close up, the inside of the bend is displayed, unveiling that the erosion happens on a larger area and that the erosion decreases near the outlet of the bend. In contrast to that, Figures 4.5c and 4.5d show examples of a particle erosion. There, the major part of the geometry is unaffected, in this example case, the erosion happens at the lower side of the cross section of the 90° elbow, directly after the bend.

### Mesh Refinement

As mentioned before, the coarse mesh, caused by the erosion, has to be somehow refined. The general scheme of the deformation and consecutive refinement is shown in Figure 4.6a. The tool for the refinement is based on the OpenFOAM utility *refineWallLayerSmart*, which is based on its part on the official OpenFOAM utility *refineWallLayer*. The idea of the *refineWallLayerSmart* utility is to refine the





**Figure 4.5:** Mesh Deformation (2)

mesh to a target  $y^+$  value. In contrast, the aim of the adapted version, named *refineWallLayerSmart\_yplas\_av*, is to keep the  $y^+$  constant, despite the deformation. That means that the average  $y^+$  of the deformed case will become nearly the the same as the average  $y^+$  of the undeformed case. To achieve this goal, several steps have to be taken. The first step is to calculate a new  $y^+$  value for the deformed but not refined mesh. Hence,  $y^+$  is calculated with the already mentioned equation 3.14:

$$y^+ = \frac{y u_\tau}{\nu} \quad (4.6)$$

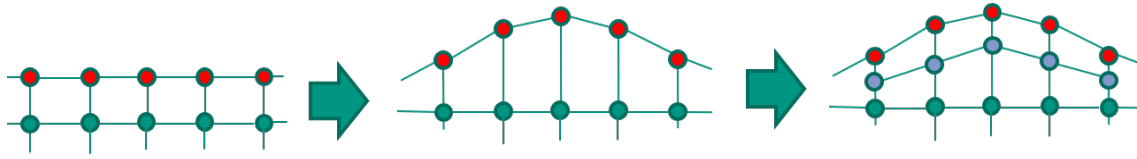
$u_\tau$  and  $\nu$  are not changed in the process of deformation. Therefore, the  $y^+$  value changes solely due to the change of  $y$ , therefore following relation is valid:

$$\frac{y_{new}^+}{y_{undeformed}^+} = \frac{y_{new}}{y_{undeformed}} \quad (4.7)$$

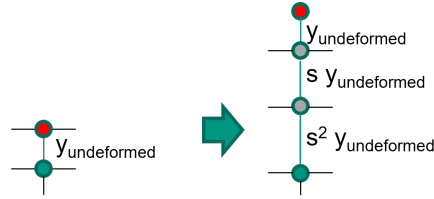
Furthermore, more than one layer should be generated if the deformation of the mesh is too large and the layers should grow with a stretch factor  $s$ , like it is shown in Figure 4.6b. There the growth of the layers should obey following equation:

$$y_{new} = y_{undeformed} + s y_{undeformed} + s^2 y_{undeformed} + \dots + s^N y_{undeformed} = y_{undeformed} \sum_{n=0}^N s^n. \quad (4.8)$$

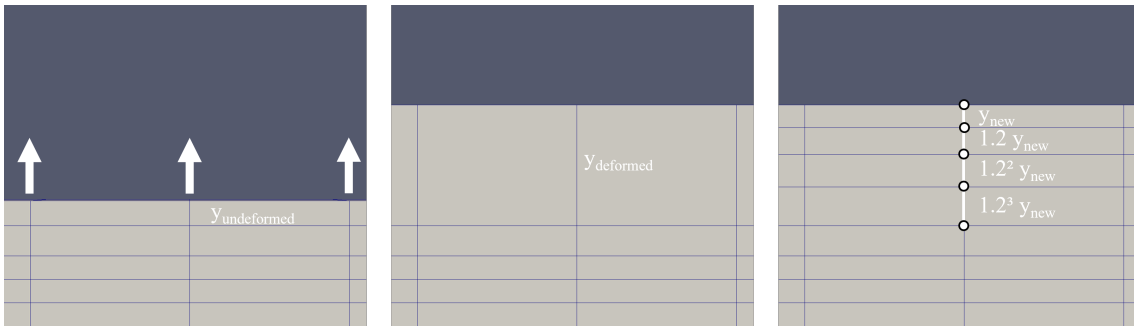
#### 4. Erosion Modeling in a Mesh Adapting Framework



(a) General scheme for mesh deformation and consecutive refinement



(b) Mesh refinement to keep  $y^+$  constant with stretching factor



(c) Mesh refinement on an actual mesh with a stretching factor of 1.2 ( $y^+_{undeformed} = 96$ ,  $y^+_{deformed} = 509$ ;  $y^+_{new} = 82$  (values are averaged))

**Figure 4.6:** Mesh Refinement

This sum is called a geometric series and can be rewritten to

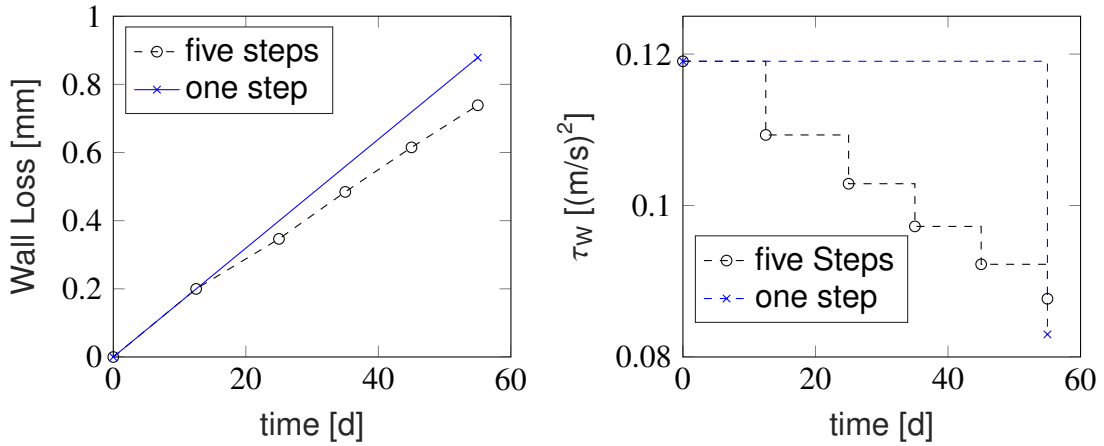
$$\frac{y_{new}}{y_{undeformed}} = \frac{1 - s^{N+1}}{1 - s} \quad (4.9)$$

With equation 4.9 and 4.7, a decision can be made about how often the cell has to be divided to keep the  $y^+$  constant:

$$\frac{\ln\left(1 - \frac{y_{new}^+}{y_{undeformed}^+}(1 - s)\right)}{\ln s} - 1 = N = \text{Refinementvalue}. \quad (4.10)$$

$N+1$  is the number of times the deformed cell has to be split to achieve the required  $y^+$  with the given stretch ratio. As  $y^+$  is defined a priori, 4.10 does not result in a natural number, the result has to be rounded to the next natural number.

An actual example case is shown in Figure 4.6c, there, the averaged  $y^+$  value of the undeformed mesh is 96. After the deformation, this value becomes 509. With equation 4.10 and a given stretching factor of 1.2, the refinement value is 2.9 which means it is rounded to 3, hence, the stretched cell will be split three times. After the deformation and refinement, a new CFD calculation can be started with the deformed mesh. This recalculation of the case leads to an actual average  $y^+$  of 82, which is close to 96, and therefore, it can be assumed that the given refinement method can keep the  $y^+$  around the given range.



(a) Wall loss after 55 days

(b) The corresponding wall shear stress, which is used for the extrapolation

**Figure 4.7:** Example of a wall loss modeling at fixed location in a elbow for 55 days of erosion, where the modeling happen in 5 steps and only one step.

### 4.1.4 Time Iteration

The last step of the iteration of the workflow is the restart of the process. One iteration involves the CFD calculation, the determination of the erosion rate, the erosion over a given time, and the deformation of the geometry over the given time  $\Delta t_E$ . The idea of the workflow is to model an erosion process over a total time  $T_E$ , this total time is reached by the summation of the time steps gained in each iteration:

$$T_{E,I} = \Delta t_{E,1} + \Delta t_{E,2} + \dots + \Delta t_{E,i} \quad (4.11)$$

The single time steps in each iteration should not be too large, otherwise the flow conditions could change too much between the extrapolations, and with the flow conditions, also the predicted erosion changes. Figure 4.7 shows an example how the predicted erosion is influenced by different time steps. In one case, the workflow, shown in Figure 4.1, was passed only one time, the extrapolated time was 55 days. In the other case, the workflow passed 5 iterations. As it can be seen from the diagram, the final wall loss differs significantly between the cases. The wall loss for the case with only one step is 0.88 mm and from the case with five sub-time steps 0.73 mm, which makes a difference of around 21%. The reason for the difference is the change of the flow conditions within the 55 days due to the erosion, and therefore, the WSS decreases like it is shown in Figure 4.7b. Every time step leads to a reduction of the WSS, and this reduced shear stress is used for the next iteration round which leads to a reduced predicted wall loss. In that case, a direct extrapolation in one time step would lead to a higher wall loss.



# 5. Application of the Method and Its Validation

In this part of the work, the method which was presented in the last chapter has to be validated by comparing it to experimental investigations of FAC erosion and particle erosion. The difficulty of modeling is that it is always a simplification of reality and, in case of erosion, a lot of different mechanisms are taking part in the overall process. Therefore, the aim of the modeling is not to take all aspects of the process into account but to get an overall idea of how the flow driven erosion deforms the geometry.

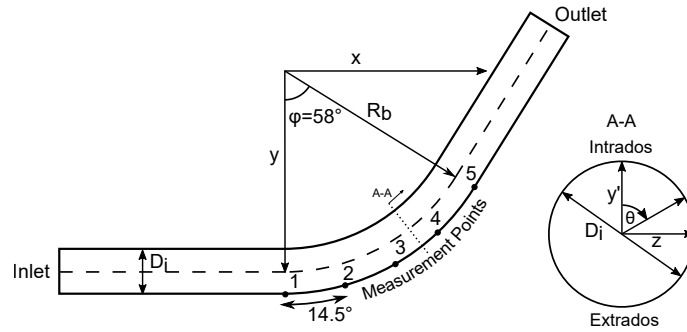
## 5.1 Flow Accelerated Corrosion in a 58° Elbow

### 5.1.1 Summary of the Experiment

The experiment for the validation was conducted by Prasad et al. (2018), the numerical investigations from this work are already described in chapter 2.4. The investigated object in this work was a 58° elbow with water as fluid. The stated dimensions of this elbow are an inner diameter  $D_i$  of 13.9 mm and an outer diameter  $D_o$  of 21.3 mm, which results in a theoretical wall thickness of 3.7 mm. Measured wall thicknesses at the extrados of the bend were between 3.9 mm and 4.4 mm at the beginning of the bend. The bend radius  $R_b$  of the elbow is two times the outer diameter, i.e. 42.6 mm. The temperature of the water is kept at 120 °C during the experiment, and also the pH value of 7 was kept constant. A constant volume flow rate of 1.06 l/s leads to an average flow velocity of 7 m/s. The used construction material is a carbon steel named ASTM A106 Gr "B". The experiment was conducted for 55 days, and the wall thickness was measured at the beginning and the 25<sup>th</sup>, 35<sup>th</sup>, 45<sup>th</sup>, and 55<sup>th</sup> day. The ferrous iron concentration in the bulk water was 80 µg/l at the beginning of the experiment. Due to filtration, the concentration of these ions were kept at a value of 250 µg/l to 300 µg/l during the experiment, which is low compared to the equilibrium concentration at 120 °C. The wall thickness was measured with ultrasonic technique at specific points at the extrados of the elbow on the symmetry plane. The locations of these points can be seen in Figure 5.1. For a better overview, the two angles are introduced  $\varphi$  and  $\theta$ .  $\varphi$  describes the angle along the bend, and  $\theta$  describes the position in the pipe. The angles are also shown exemplary in Figure 5.1. In terms of this notation, the

**Table 5.1:** Summary of the geometry and flow conditions

Geometry	
Bend angle	58 °
Inner diameter $D_i$	13.9 mm
Outer diameter	21.3 mm
Bend radius $R_b$	42.6 mm
Operating conditions	
Fluid	water
Temperature	120 °C
Averaged velocity	7 m/s
Kinematic viscosity	$2.46 \times 10^{-7} \text{ m}^2/\text{s}$
Reynolds number	400 000



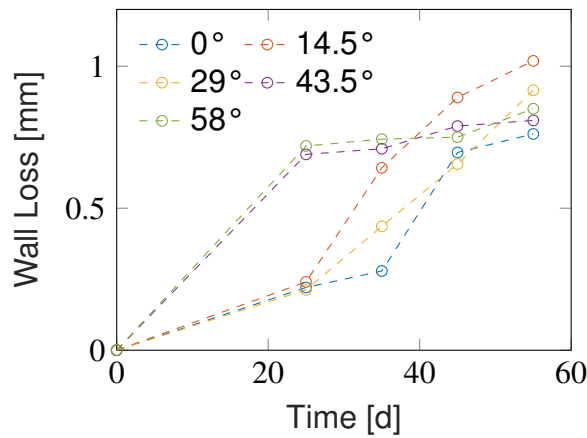
**Figure 5.1:** Schematic of the 58° elbow with the locations of the measurement points. (According to Prasad et al. (2018))

measuring points on the extrados are between 0° and 58° and  $\theta=180^\circ$ . The angular interval between every measurement point is around  $\Delta\varphi=14.5^\circ$ . The kinematic viscosity ( $\nu= 2.46 \times 10^{-7} \text{ m}^2/\text{s}$ ), which is needed for the CFD calculation, was taken from Huber et al. (2018) at 120 °C and saturation pressure. For these dimensions and flow conditions, the resulting Reynolds number  $Re$  is around 400000, which means that the investigated case clearly is a turbulent case. The dimensions and hydrodynamic parameters of the experiment are summarized in Table 5.1.

In Figure 5.2, the results of the experiment are shown. There the wall loss at the different measuring points over time are depicted. The range of wall loss after 55 days is between 0.7 mm and up to 1 mm. From the diagram, it can be seen that in the first half of the experiment the points at the end of the bend (43° and 58°) suffers of much more erosion than the other measuring point. For the second half this trend is reversed. The slope of the wall loss flattens dramatically at the last two locations and gets steeper for the rest of the points, even to the point, where the erosion at 14.5° and 29° exceeds the wall loss of the other points.

### 5.1.2 CFD Calculations and Modelling of the Erosion

The CFD calculations were carried out like described in the chapters 3.1 and 3.2. The results of the undeformed initial CFD simulation are shown in Figure 5.3, and are discussed exemplarily in the following. The case was set up with the same parameters as the experiment. In Figure 5.3a, three velocity profiles



**Figure 5.2:** Wall loss during the experiment at the different positions (from Location 1 ( $\varphi=0^\circ$ ) to Location 5 ( $\varphi=58^\circ$ ))

are compared, two profiles 1D and 2D, respectively, away from the inlet and one profile from the preconditioning straight pipe (described in chapter 3.2.1). As it can be seen, all profiles are matching each other and have a typical profile of a fully developed turbulent flow. That means an hydraulic developed velocity profile was used as an inlet condition. The inlet length of the computational domain is  $12D_i$ , due to the mesh deformation in the later process. The boundary mesh will be slightly deformed in every time iteration step, therefore, the developed profile can redevelop before entering the elbow. The CFD calculation was carried out with wall functions.

In Figure 5.3b, the overall behavior of the flow through the elbow is shown: the velocity profile in axial direction and streamlines (gray) depict the the flow along the elbow. From the axial profile, it can be derived that a detachment zone develops along the bend, and hence, a zone of less flow velocity is located after the bend on the intrados side and a zone of high velocity on the extrados side. Additionally to the detachment zone, the elbow introduces a three dimensional character of the flow. This can be seen on the basis of the streamlines. Before the bend, all of the streamline are well aligned, during the bend, the streamline gets twisted and twirled. Additionally to the axial behavior of the flow, several cross sections are depicted in Figure 5.3b. These cross sections serve as help for orientation. In Figure 5.4, four of these cross sections are shown in detail. In the diagrams of Figure 5.4, the secondary flows, which are introduced by the bend, are investigated. The secondary flows are shown at different positions of the pipe. The first cross section is taken from the middle of the bend at  $\varphi=29^\circ$ , the second cross section from the end of the bend ( $\varphi=58^\circ$ ), and the third and fourth were taken from  $2D_i$  and  $4D_i$ , respectively, after the bend. For orientation, the position of the intrados and extrados are marked in the diagrams. The length and the color of the velocity vectors indicate the magnitude of the secondary flow. The shown swirls, which are indicated in Figure 5.3b with the streamlines, are developing along the bend. At  $29^\circ$ , midway through the bend, two swirls can be already identified in Figure 5.4a. They are symmetric to the vertical symmetry plane. Downstream, the secondary flows are becoming a more relevant factor. From the figures' point of view, the swirls in Figure 5.4a to Figure 5.4c are moving from the horizontal center towards

the intrados of the elbow and towards the vertical center. The swirls remain stable after the bend and are only decaying slowly along the pipe. In Figure 5.4d, 4  $D_i$  after the bend, the swirls are still distinct but the magnitude of the velocity vectors decreases. The last figure also indicates that the swirls are moving back towards the horizontal center of the pipe. Hence, the secondary flows lead to a three dimensional behavior of the flow. With the velocity profiles the WSS can be calculated. The WSS distribution for the intrados can be seen in Figure 5.3c and for the extrados in Figure 5.3d. From these figures, it becomes clear that the intrados experiences a distinctly higher WSS than the extrados, quantitatively this can be confirmed by the diagram in Figure 5.3e. This diagram shows the WSS trend along the elbow. As a further information from Figure 5.3c, it can be extracted that the highest point of WSS is at the beginning of the bend in the center of the pipe ( $\theta=0^\circ$ ). The WSS distribution is symmetric to the axial symmetry plane of the pipe. The minimum of the WSS is also located at the intrados ( $\theta=0^\circ$ ) and is induced by the already mentioned detachment zone next to the symmetry plane ( $0^\circ < \theta < 90^\circ$ ) towards the end of the bend ( $\varphi \rightarrow 58^\circ$ ). In contrary to the extreme values at the intrados, the extrados experiences medium WSS. Another difference for the intrados and the extrados can be seen in the local trend of the WSS in Figure 5.3e, where  $\theta$  is set to  $0^\circ$  and  $180^\circ$ . As already mentioned, the intrados suffers the highest WSS at the beginning, or, to be more specific, at  $\varphi=11^\circ$  into the bend and then decreases. For the extrados it is the other way round, there the WSS increases to the end of the bend and reaches its maximum at the outlet of the bend. The behavior of the WSS can be led back to the detachment zone and the symmetric swirls: The detachment induces the WSS decrease along the intrados and the increase at the extrados and the swirls are in alignment with the local maxima at the sides of the elbow. In Figure 5.3c, after the bend, a line of less WSS along the center of the pipe can be distinguished. This area of low WSS also indicates stable swirls downstream of the pipe.

Figure 5.3 and Figure 5.4 show the calculated starting conditions of the erosion modeling. This simulation can now be used as the initial step for the presented method. To determine the FAC-rate  $R_c$  the equation 2.1 was introduced in chapter 2.1:

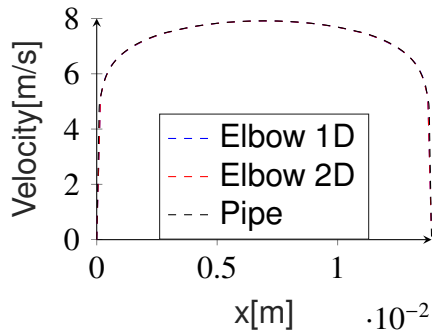
$$R_c = MTC(C_w - C_B). \quad (5.1)$$

For the MTC, the also already introduced Chilton-Colbrun correlation (equation 2.9) will be used:

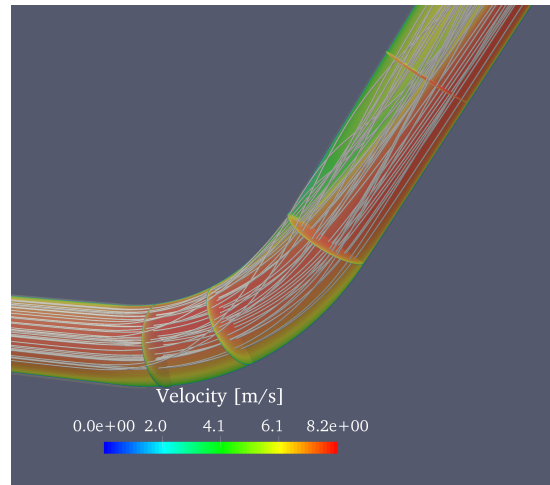
$$MTC = \frac{\tau_w}{u\rho} S c^{-\frac{2}{3}}. \quad (5.2)$$

This means, for the estimation of the erosion the following quantities have to be known: the Schmidt number, the averaged velocity, the fluid's density, and the WSS. The WSS distribution from the CFD calculation already is a function of the density, so the fluid's density is not needed for the calculation. The averaged velocity is known from the experiment, and the Schmidt number can be calculated with the kinematic viscosity  $\nu$  and the diffusion coefficient  $D$  of the iron ions (equation 2.5). The kinematic viscosity is known which makes the last unknown quantity for the MTC the diffusion coefficient of the iron ion. In chapter 2.1.1, different ways to calculate a diffusion coefficient are presented. The diffusion coefficient

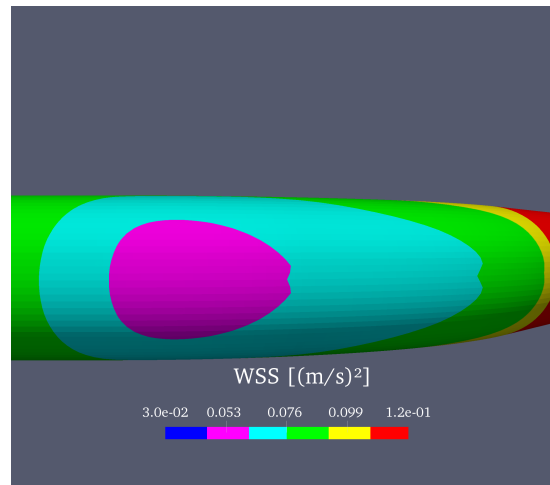
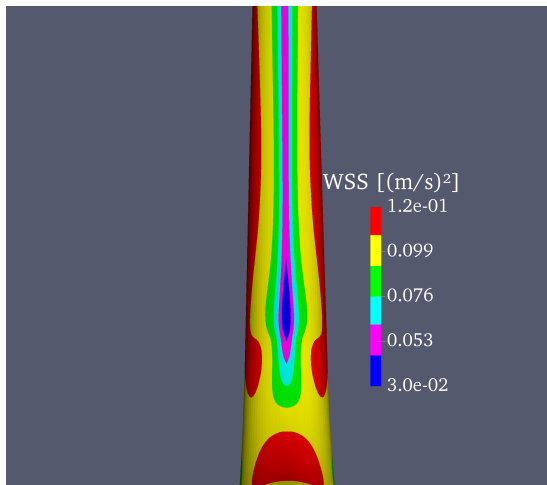




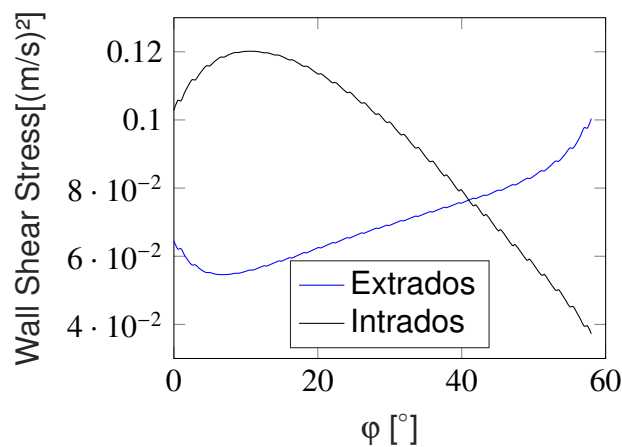
(a) Profile comparison 1D and 2D away from the elbow's inlet and profile in a preconditioned straight pipe



(b) Velocity distribution along the elbow with detachment zone and streamlines. Indicated cross sections are shown in more detail in 5.4.

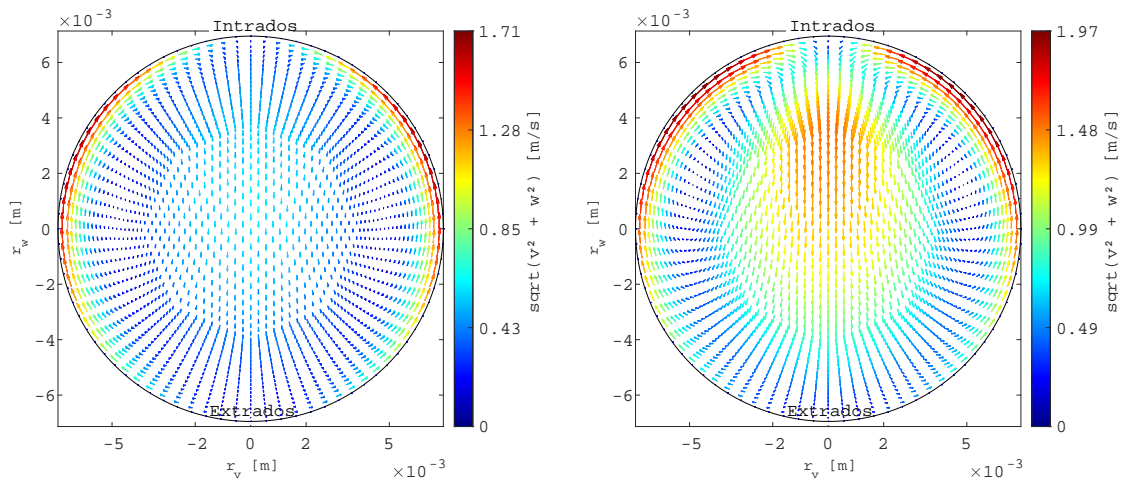


(c) WSS distribution at the intrados of the elbow (d) WSS distribution at the extrados of the elbow

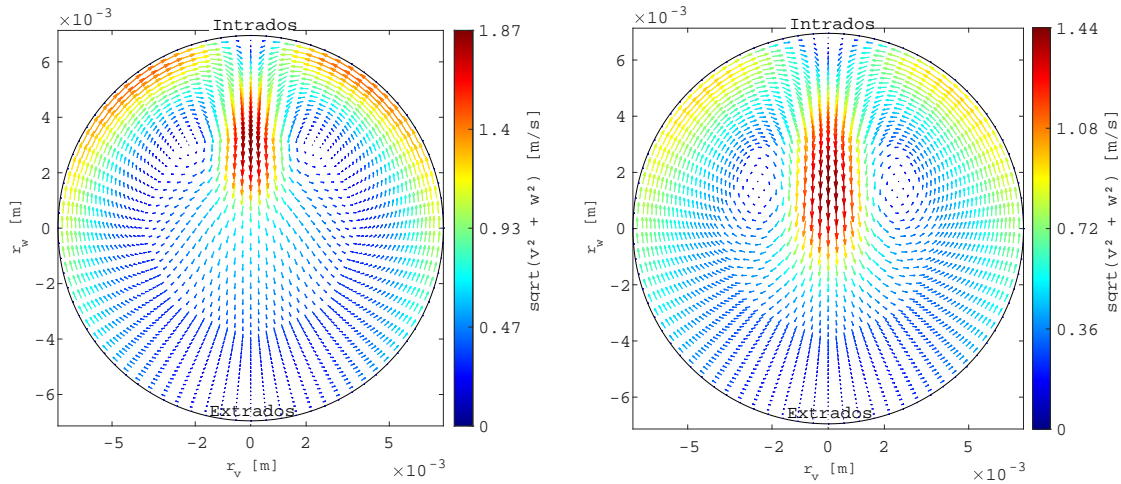


(e) WSS along the bend angle of the elbow at the intrados ( $\theta=0^\circ$ ) and extrados ( $\theta=180^\circ$ )

**Figure 5.3:** CFD results of the undeformed  $58^\circ$  elbow



(a) 29°: Developed swirls in the center ( $r_w$  direction) of the pipe (b) 58°: Developed swirls moved from the center to the intrados of the bend.



(c) 2  $D_i$  after the bend: Developed swirls moved closer to each other and to further to the intrados. (d) 4  $D_i$  after the bend: Developed swirls stay the same but move back to the horizontal center.

**Figure 5.4:** Secondary flow within an 58° elbow at different cross sections

**Table 5.2:** Summary of the quantities necessary for the erosion calculation

<b>Erosion conditions</b>	
Temperature	120 °C
Averaged velocity	7 m/s
Kinematic viscosity	$2.46 \times 10^{-7} \text{ m}^2/\text{s}$
Diffusive species	$\text{Fe}^{2+}$
Diffusion coefficient	$3.64 \times 10^{-9} \text{ m}^2/\text{s}$
Schmidt number	67.6
Concentration difference	$1.52 \times 10^{-3} \text{ kg}/\text{m}^3$
Steel	ASTM 106 Gr "B" carbon steel
Steel density	$7850 \text{ kg}/\text{m}^3$

of  $\text{Fe}^{2+}$  at 298.15 K is  $7.19 \times 10^{-10} \text{ m}^2/\text{s}$  (Lide et al., 1994), and with equation 2.13, the temperature dependency can be calculated. Hence, for 120 °C the diffusion coefficient is  $3.64 \times 10^{-9} \text{ m}^2/\text{s}$ . From equation 2.14, it can be seen that  $\text{Fe}^{2+}$  is not the only possible ion but it is the smallest one, and therefore, the one with the highest diffusion coefficient. Thus, it is the most conservative assumption for the determination of the diffusion coefficient. With the diffusion coefficient and the kinematic viscosity, the Schmidt number adds up to 67.6.

With the assumption that the concentration difference is location-independent, the concentration difference purely is a scaling factor of the erosion. The concentration difference was determined by the wall loss in the straight pipe, namely by the wall loss at position 1 over the first 25 days, and was set to  $1.52 \times 10^{-3} \text{ kg}/\text{m}^3$ . Compared to the Pourbaix diagram, described in chapter 2.1.2, the concentration difference is plausible: for a pH-value of 7 the Pourbaix diagram estimates a saturation concentration of  $1.15 \times 10^{-3} \text{ kg}/\text{m}^3$ , which is close to the calculated  $1.52 \times 10^{-3} \text{ kg}/\text{m}^3$ . Deviations can be led back to the difference in temperature. The Pourbaix diagram shows the saturation temperature for 298 K, but the experiment was done at 393 K, and secondly, small variations of the pH-value lead to huge variation of the saturation concentration. Hence, for further calculations  $1.52 \times 10^{-3} \text{ kg}/\text{m}^3$  were used as the concentration difference.

To calculate, the wall loss over time according to equation 4.3, the density of the construction material is needed. In the experiment, the construction material of the pipe is ASTM 106 Gr "B" carbon steel with a density of  $7850 \text{ kg}/\text{m}^3$  (Projectmaterials, 2017). The quantities are summarized in table 5.2.

In Figure 5.5a and 5.5b, the predicted wall loss after 55 days is shown. The positions of the most severe wall loss match with the regions of high MTC shown in Figure 5.5c. The predicted wall loss for the time period of 55 days differs from 0.07 mm to 0.9 mm. In the straight pipe before the bend, the wall loss is evenly distributed and is about 0.55 mm. In the intrados three hot spots of severe wall loss can be identified: in the center at the beginning of the bend the wall loss is maximum with 0.9 mm and the secondary maxima are next to the symmetry plane with 0.8 mm nearly at the end of the bend ( $\varphi=58^\circ$ ). The minimum wall loss at the intrados is only 0.07 mm and it is located at the symmetry plane at the end

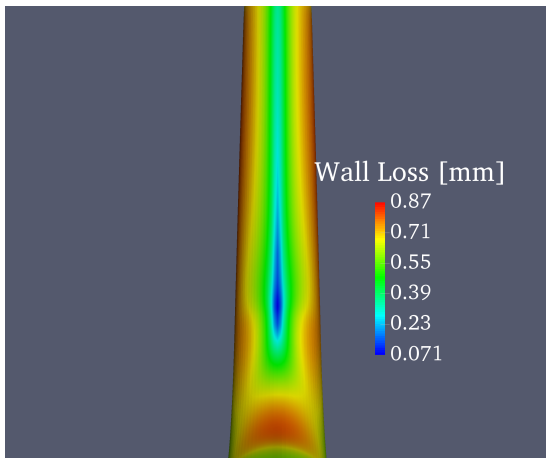
of the bend ( $\varphi=58^\circ$ ,  $\theta=0^\circ$ ). Hence, the wall loss differs between the maximum and minimum by a factor of more than 10. From the point of minimum wall loss, a streak of less wall loss develops along the pipe downstream of the bend. As a compensation of this area of less wall loss, the back side of the straight pipe downstream of the bend suffers a wall loss of up to 0.9 mm, which means that this wall loss is comparable to the maximum in the bend. It is a large area of high wall loss downstream of the bend, which can be seen in Figure 5.5b. As already mentioned before, Figure 5.5c shows the MTC distribution, the picture is split in two parts: one part of the figure is the MTC distribution which was used for calculating the erosion for the first 12.5 days, and the other part shows the MTC distribution which was used to calculate the last 10 days of the experiment. As it can be seen, the MTC decreased between day 12.5 and day 55 and with it the wall loss over time. Exemplarily for the reduction of the MTC in the elbow, the diagram in Figure 5.5d shows the reduction of MTC over time at different angle positions at the intrados. The angle positions are  $\varphi=0^\circ$ ,  $11.5^\circ$ ,  $29^\circ$ , and  $58^\circ$ , which means at the beginning of the bend, at the position of the highest MTC, in the middle of the bend, and at the end of the bend. At the maximum point of MTC, the MTC drops from 0.001 m/s to 0.0007 m/s. This corresponds to a wall loss rate from 0.7  $\mu\text{m}/\text{h}$  to 0.5  $\mu\text{m}/\text{h}$ .

The reason for the predicted decreasing wall loss over time is the erosion itself. Due to the wall loss, the effective diameter of the straight pipe increases from 13.9 mm to 15 mm before the bend, which is an increase of 8%. The volume flow rate remains the same, therefore, the average velocity decreases, and hence, the Reynolds number decreases from around 400 000 to 370 000. Due to that, the predicted erosion slows down as time goes by. This process can also be seen in Figure 5.5e. There, the wall loss at the intrados for different positions along the symmetry plane over the days is shown. The positions were chosen in alignment with the measuring points at the extrados for the experiment. The slowing down can be seen especially near the end of the bend. The wall loss between  $0^\circ$  and  $29^\circ$  is still nearly linear over the 55 days, which means there the wall loss rate is constant over the whole time period. This is different for the two locations at the end of the bend,  $43.5^\circ$  and  $58^\circ$ , there the wall loss rate already decreases significantly. For  $58^\circ$  it seems that the calculated wall loss is already stagnating, there is nearly no further wall loss between day 45 and day 55.

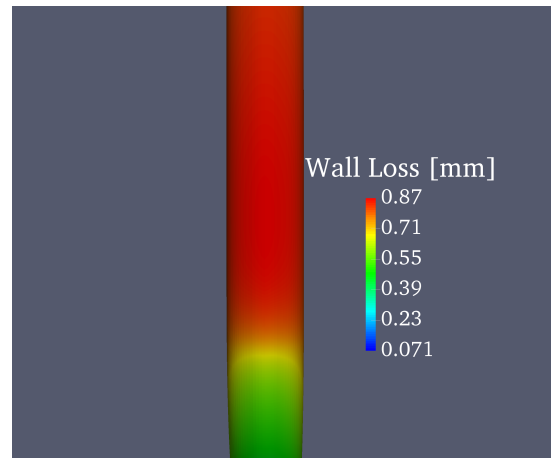
### 5.1.3 Comparison of the Experiment with the CFD Modelling

In the description of the experiment, it is already mentioned and it is shown in Figure 5.1 that the wall measuring points of the experiment are at the extrados, an area of an expected medium wall loss. The comparison of the calculated wall loss, the measured wall loss, and the simulated wall loss from Prasad et al. (2018) at these positions are shown and summarized in Figure 5.6. Figure 5.6a and Figure 5.6b show the wall loss at the measuring points as a function of time. In contrast, Figure 5.6c shows the results in dependence of the angle and the days are fixed. From these diagrams it can be seen that the theoretical predictions of Prasad et al. (2018) always have the same rate. That means, according to

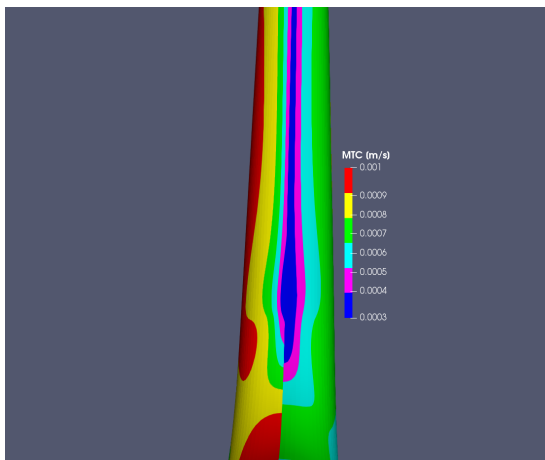
## 5. Application of the Method and Its Validation



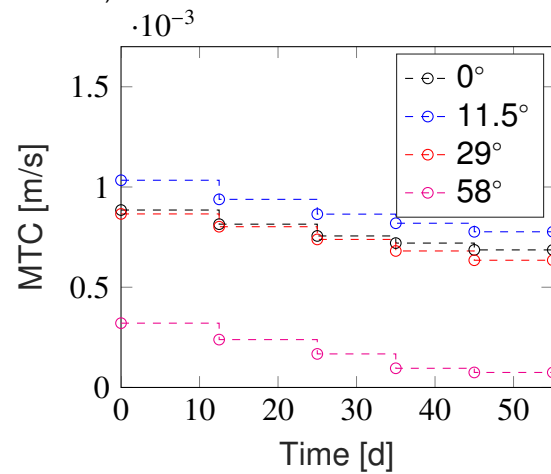
(a) Predicted wall loss after 55 days (view on the intrados).



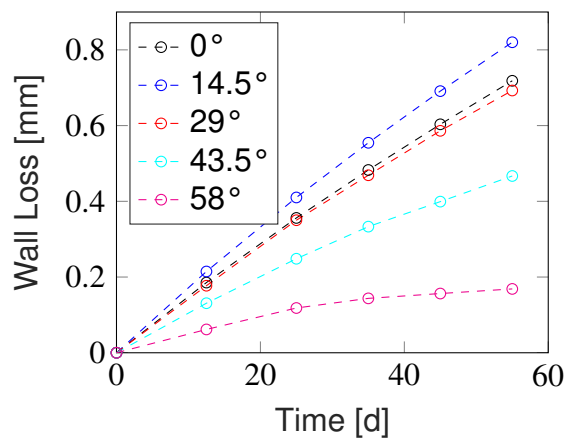
(b) Predicted wall loss after 55 days (view on the extrados).



(c) MTC distribution for the wall loss from 0 days to 12.5 days (left)



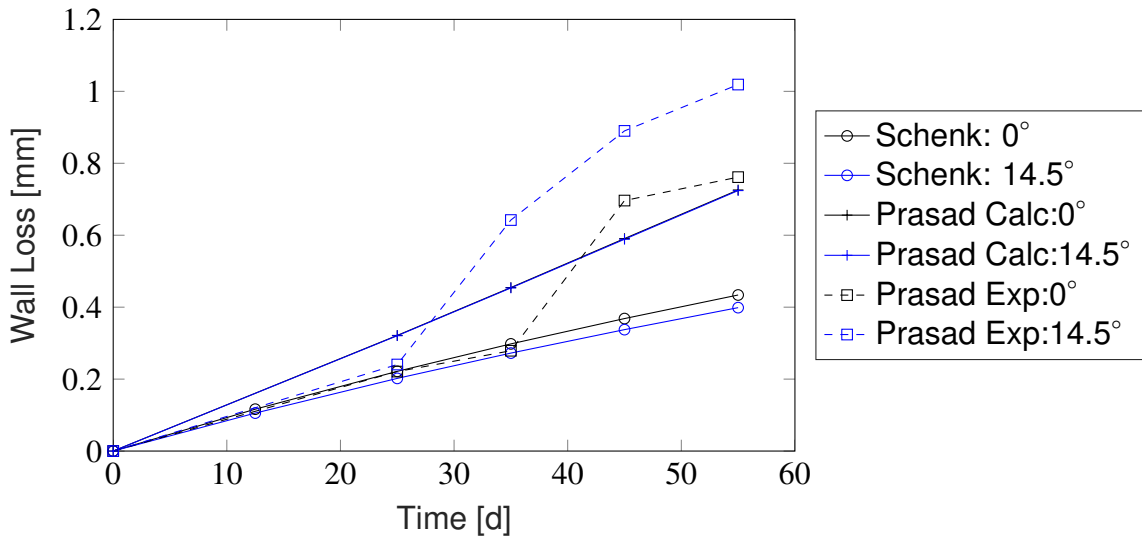
(d) MTC development during the simulation at different position of the intrados ( $\theta=0^\circ$ ) (right).



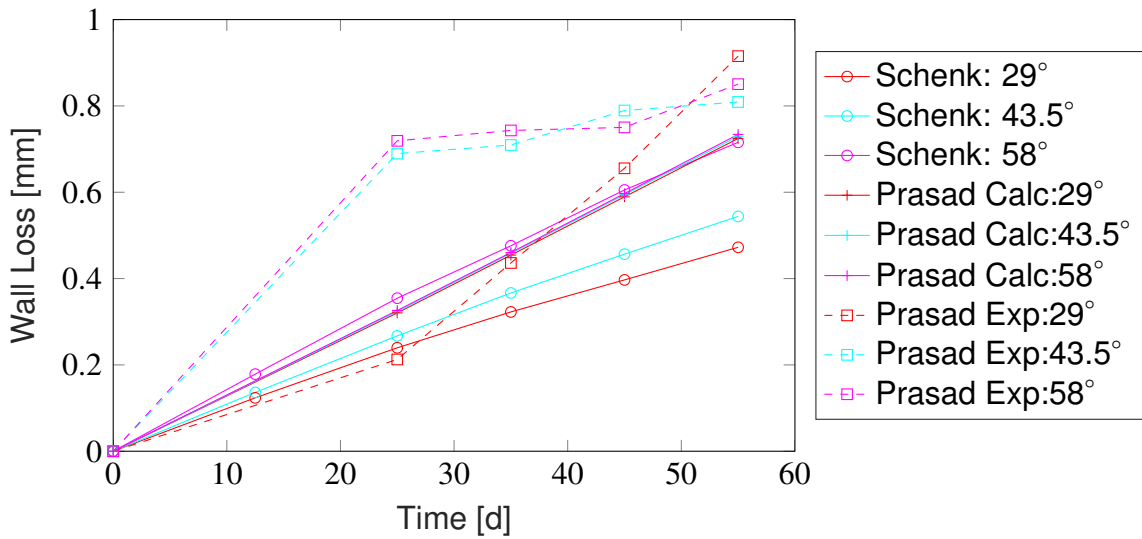
(e) Wall loss at the intrados ( $\theta=0^\circ$ ) in dependence of the  $\varphi$ .

**Figure 5.5:** CFD wall loss prediction of the 58° elbow.

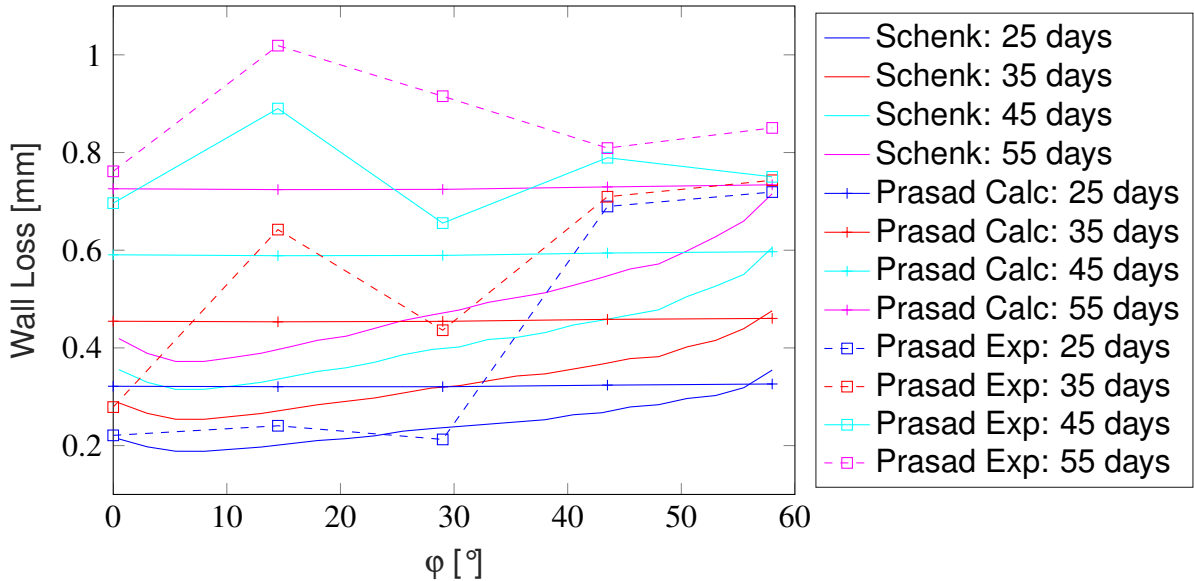
## 5. Application of the Method and Its Validation



(a) Wall loss at the extrados in dependence of the time for  $\phi = 0^\circ$  and  $14.5^\circ$ .



(b) Wall loss at the extrados in dependence of the time for  $\phi = 29^\circ, 43.5^\circ$ , and  $58^\circ$ .



(c) Wall loss at the extrados in dependence of the angle  $\phi$ .

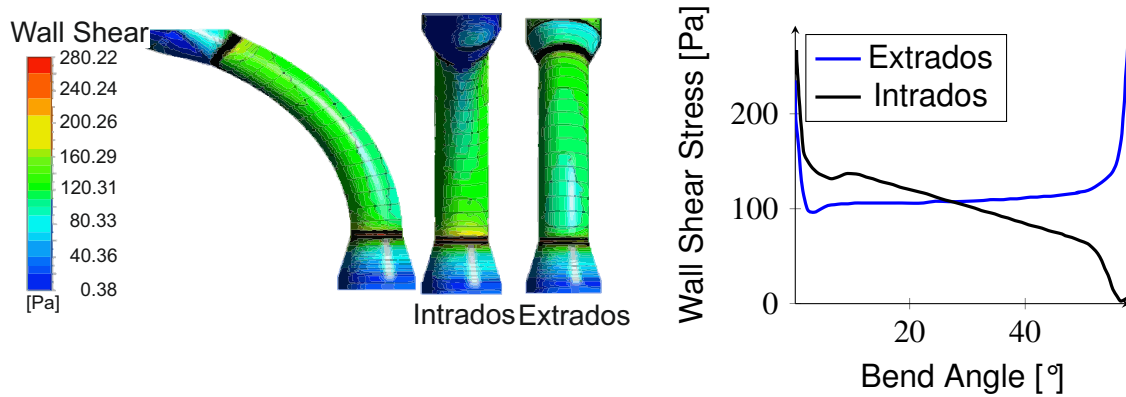
**Figure 5.6:** CFD wall loss prediction of the  $58^\circ$  elbow vs. the measured wall loss and the predicted wall loss from Prasad et al. (2018)

them, the development of the degeneration of the wall is linear. This is because they calculated the MTC once and extrapolated it for the whole experiment. More important is that they also predict the same degeneration at every position with no local effects. In the diagrams, this circumstance arise from the fact that in the first two diagrams the graphs of Prasad et al. (2018) are in alignment with each other and show no differences for different positions, and in the last diagram the results from Prasad et al. (2018) are horizontal lines with no dependencies of the angle. Even though Prasad et al. (2018) used a geometrical factor (described in chapter 2.4.1), it does not affect the results. Prasad et al. (2018) use a 2D computational domain for calculation, this could be a reason for non-existing geometrical effect.

In contrast to the theoretical results of Prasad et al. (2018), the experimental results show a strong local behavior and also nonlinear time dependency. The erosion modeling in this work also shows differences for different locations. By comparing the modeling results from this work with the experimental results, it can be seen that for the first half of the bend (up to  $29^\circ$ ), and nearly half of the experiment time (up to 25 days), the results are in agreement with the experiment. This agreement holds for the starting of the bend at  $0^\circ$  up to 35 days before the results starts to differ. For the second half ( $43.5^\circ$  and  $58^\circ$ ) of the bend, the experiment shows a huge wall loss in the first days already. Qualitatively, the modeling shows the largest wall loss also at the second half of the bend, this is in alignment with the wall shear stress distribution shown in Figure 5.3e: the WSS rises until the end of the bend at the extrados. Quantitatively, the modelling underestimates the measured wall loss significantly at this area. From day 25, these underestimation also migrates to the beginning of the bend. At  $43.5^\circ$  and  $58^\circ$ , the underestimation is reduced over time because the experiment shows a constant behavior for the rest of the experiment. The largest difference quantitatively, but especially qualitatively, is at around  $14.5^\circ$ , the modeling expects the least wall loss with around 0.4 mm, but the experiment measures the most wall loss with 1 mm.

There could be several reasons for the difference in the qualitative behavior. Firstly, erosion is a stochastic process (Prasad et al., 2018), imperfections of the construction material are distributed stochastically. Imperfections are starting points of corrosion and will be attacked more severely than areas with no defects. The modeling, or better the correlations, can only expect uniform behavior of the construction material. One single experiment could deviate from this behavior. Secondly, and more important, the experimental set-up was chosen extremely aggressive by Prasad et al. (2018). The works of Kain (2014), Madasamy et al. (2018), and Sweeton et al. (1970) mention that the chosen environment,  $120^\circ\text{C}$  and a pH of 7, is one of the most aggressive set-ups for corrosion investigations (for water/carbon steel combinations). And as the Pourbaix diagram in Figure 2.4 shows, no protective magnetite layer can be formed under these conditions. Additionally, this aggressive regime is accompanied by a high Reynolds number of 400 000. Normally, these kinds of processes are slow, and it would take a lot of time for the experiments. Therefore, this aggressive environment was chosen, and even then the experiment took nearly two months. But this also means that in this regime, small variations of the pH-value can lead to differences in the corrosion

## 5. Application of the Method and Its Validation



(a) WSS distribution along the test section in Madasamy et al. (2018) (b) WSS distribution with respect to bend angle in Madasamy et al. (2018).

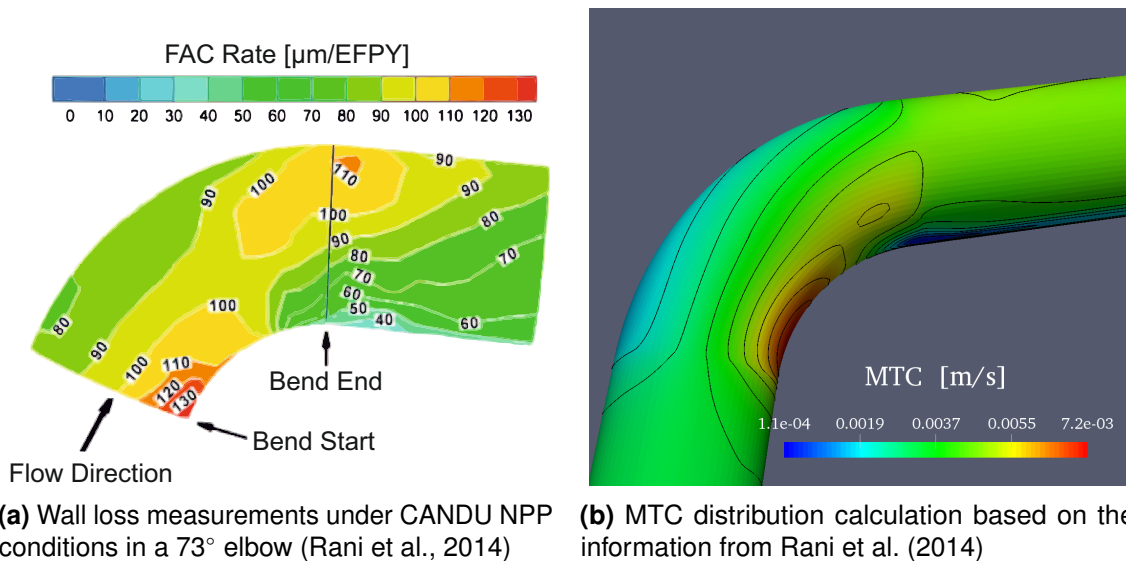
**Figure 5.7:** Results of the numerical investigations of Madasamy et al. (2018) <sup>1</sup>

behavior. The experiment and the modeling start with good agreement timewise and locally. As mentioned before, the wall loss starts to differ at the exit of the bend, where the WSS is the highest. Unfortunately, the first measurement was performed after 25 days, hence, it can not be distinguished if the wall loss at the exit happened gradually or abruptly, but for an abrupt breakaway speaks the later behavior of this area: during the rest of the experiment, the wall loss is gradual and with a comparable slope to the modeled one. It can be expected that between day 25 and day 35 somewhere between  $29^\circ$  and  $43.5^\circ$ , a sharp edge exists. This edge could lead to disturbance of the flow, and therefore, to a locally declined pH-value: according to equation 2.14, during the dilution of iron, also  $H^+$ -ions are produced. If these  $H^+$ -ions could not be transported away immediately, the local pH-value declines. Only a small decline of the pH-value leads to a significant higher dissolution of iron, as it is shown in the Pourbaix diagram in Figure 2.4. This could explain the nonlinear behaviour of the wall loss. On day 35 the deviation already reached  $14.5^\circ$ , at this point the start of the bend is still in alignment with the predicted wall loss. After day 35, the edge also reaches the beginning of the bend and the difference between the wall loss at the beginning of the bend and at the end of the bend are closing because the end of the bend stops losing much material after day 25, while the rest starts to catch up.

That this behavior is rather unlikely, and therefore, can be led back to above's interpretation, shows other corrosion works. Madasamy et al. (2018) used a slightly different geometry in a comparable aggressive environment. Their numerical investigations are qualitatively in line with in this work's presented investigations. In Figure 5.7, parts of their results are shown. The wall shear is similarly distributed as in this work, especially because the authors lead back the strong changes, which can be seen in Figure 5.7b, at the beginning and at the end of the bend, to their slightly different geometry set-up: the connection to the test section reduces the larger pipe of the facility to the smaller elbow, and the connection from the elbow back to the pipe is the other way round, like it can be seen in Figure 5.7a.

<sup>1</sup>Figure 5.7a is reused with the permission of the rights owner





**Figure 5.8:** Presented results from Rani et al. (2014)<sup>2</sup> and CFD calculation based on Rani et al. (2014)

Another example of the qualitative conformity of this work expected behavior is the work of Rani et al. (2014). In Figure 5.8a, they present the measurement of the FAC rate in a 73° elbow under CANDU NPP conditions. The wall loss rate is presented in  $\mu\text{m}/\text{EFY}$ , where EFY stands for Effective Full Power Year. In Figure 5.8b, the simulated MTC distribution is shown. This simulation was done equivalently to above's simulations. It can be seen that the wall loss is in good agreement with the MTC distribution. A closer look at the wall loss at the extrados also reveals similarities with the WSS distribution shown in Figure 5.3e. Figure 5.8a also shows at the extrados firstly a drop to a local minimum at the beginning of the bend. Then the FAC rate increases until the end of the bend before it drops again. The reason for the much lower wall loss rates, compared to the experiment of Prasad et al. (2018) is that Rani et al. (2014) presents a real case under CANDU NPP conditions. In real cases, erosion rates are kept as low as possible because it is an unwanted process, on the contrary, in erosion investigations the erosion is tried to be sped up to reduce the experimental time, but this fast forward erosion could lead to false assumptions of the nature of the erosion.

## 5.2 Flow Accelerated Corrosion Erosion in Heavy Liquid Metals

In chapter 2.4.3, possible correlations are presented which could be suitable for heavy liquid metal applications. The selection is based on the work of Balbaud-Célérier and Barbier (2001). For pure lead three different correlations were tested, namely the correlations from Berger et al. (1977) (Index K-H), Harriott et al. (1965)(Index H-H), and Silverman (1984):

$$MTC_{K-H}[m/s] = 0.0165u[m/s]^{0.86}D_i[m]^{-0.14}\nu[m^2/s]^{-0.53}D[m^2/s]^{0.67} \quad (5.3)$$

<sup>2</sup>Figure 5.8a is reused with the permission of the rights owner

**Table 5.3:** Correlation results in a pure lead pipe flow (Balbaud-C  l  rier and Barbier, 2001)

Conditions		Results	
Temperature	600 ��C	MTC <sub>B-H</sub>	$6.22 \times 10^{-5}$ m/s
Velocity	0.42 m/s	MTC <sub>H-H</sub>	$6.73 \times 10^{-5}$ m/s
Inner diameter D <sub>i</sub>	0.01 m(estimated)	MTC <sub>Silverman</sub>	$6.59 \times 10^{-5}$ m/s
Reynolds number	27185	R <sub>c,B-H</sub>	$1.56 \times 10^{-3}$ g/m <sup>2</sup> s
<b>Properties</b>		R <sub>c,H-H</sub>	$1.69 \times 10^{-3}$ g/m <sup>2</sup> s
Kinematic viscosity $\nu$	$1.545 \times 10^{-7}$ m <sup>2</sup> /s	R <sub>c,Silverman</sub>	$1.65 \times 10^{-3}$ g/m <sup>2</sup> s
Diffusion coefficient		<b>Wall loss</b>	
D <sub>Fe in Pb</sub>	$1.15 \times 10^{-9}$ m <sup>2</sup> /s	<b>per year</b>	
Solubility of iron	25.1 g/m <sup>3</sup>	$\frac{dh}{dt}$ <sub>B-H</sub>	6255 ��m/yr
in oxygen-free lead		$\frac{dh}{dt}$ <sub>H-H</sub>	6627 ��m/yr
		$\frac{dh}{dt}$ <sub>Silverman</sub>	6668 ��m/yr

$$MTC_{H-H}[m/s] = 0.0096u[m/s]^{0.913}D_i[m]^{-0.087}\nu[m^2/s]^{-0.567}D[m^2/s]^{0.654} \quad (5.4)$$

$$MTC_{Silverman}[m/s] = 0.0177u_\tau[m/s]^{0.875}D_i[m]^{-0.125}\nu[m^2/s]^{-0.579}D[m^2/s]^{0.704} \quad (5.5)$$

As described in chapter 2.4.3, the MTC in the correlations of Berger and Harriott is a function of the velocity  $u$ , the pipe diameter  $D_i$ , and the diffusion coefficient  $D$ . In contrast, the correlation of Silverman substitutes the velocity with the friction velocity  $u_\tau$ . Balbaud-C  l  rier and Barbier (2001) apply these correlations on two different experimental set-ups. One set-up is summarized in Table 5.3. With these conditions, the measured wall loss rate is around 2600   m/yr. According to Balbaud-C  l  rier and Barbier (2001) all three correlations provide nearly the same result, as Table 5.3 also shows. To convert the units of the erosion rate  $R_C$  from  $[\frac{g}{m^2 \cdot s}]$  to  $[\frac{\mu m}{yr}]$ , the density of the construction material is used, in that case 7860 kg/m<sup>3</sup>. Balbaud-C  l  rier and Barbier (2001) conclude that all three correlations are suitable for the prediction of the wall loss in pure lead.

On the one hand, the correlations of Berger and Harriott are not suitable for the method proposed in this work, because they do not use local quantities. Therefore, a coupling with a CFD calculation would not be beneficial. On the other hand, the approach of Silvermann could be used in piping systems. With the help of CFD simulation the friction velocity  $u_\tau$  could be locally derived and used for the estimation of the MTC. Balbaud-C  l  rier and Barbier (2001) estimate the WSS with the Fanning friction factor  $f$ :

$$\tau = \frac{f}{2}u^2\rho. \quad (5.6)$$

There are several correlations for the Fanning factor, one of them is the Blasius equation:

$$f = 0.079Re^{-0.25} \text{ for } 2.3 \times 10^3 < Re < 1 \times 10^5. \quad (5.7)$$

With a Reynolds number of 27200, the described experiment is in the given range. The Blasius equation gives a Fanning factor of  $6.15 \times 10^{-3}$ . The friction velocity can then be calculated with:

$$u_{\tau} = \sqrt{\frac{\tau}{\rho}} = \sqrt{\frac{f}{2}}u, \quad (5.8)$$

The friction velocity in the investigated case is  $u_{\tau} = 0.0233$  m/s. With Silverman's correlation (equation 5.5), the MTC is  $5.2 \times 10^{-6}$  m/s. This would be a wall loss of around  $530 \mu\text{m}/\text{yr}$ , an underestimation by a factor of 5. Therefore, it is expected that Balbaud-C  l  rier and Barbier (2001) wrongly calculated their results with the bulk velocity  $u$ , and not the friction velocity  $u_{\tau}$ , because with that value the given MTC from Table 5.3 can be recalculated.

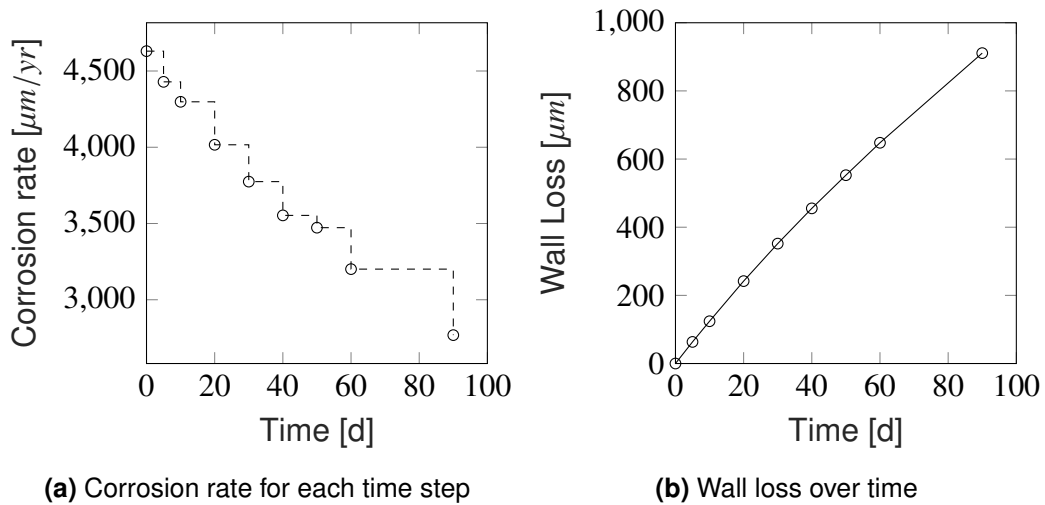
Nevertheless, a CFD calculation is done with an endless pipe like it is described in chapter 3.2.1 to get the WSS, and hence, also the friction velocity. With the given conditions, a WSS of  $5 \times 10^{-4} \text{ m}^2/\text{s}^2$  is calculated, which is a friction velocity of  $0.0224$  m/s. The two friction velocities received from equation 5.8 and from the CFD simulation are nearly the same. This means that on the one hand, the CFD calculation is in line with equation 5.6, but on the other hand, that means using this correlation would lead to a great underestimation of the wall loss. In field of engineering an underestimation is always more problematic than an overestimation, and an underestimation by an factor of 5 means that the correlation of Silverman is not suitable for the case considered. Once again, the Chilton-Colburn equation is used and tested. The Chilton and Colburn J-factor analogy (compare 2.1.1) has a wide range of application. The analogy for heat, momentum, and mass transfer can be used for fully developed turbulent flows in a range of  $10\,000 < \text{Re} < 300\,000$ ,  $0.6 < \text{Pr} < 100$ , and  $0.6 < \text{Sc} < 2\,500$ . The Prandtl number  $\text{Pr}$  is a dimensionless number for heat transfer, it is the ratio of the momentum transfer to the thermal diffusivity:

$$\text{Pr} = \frac{\nu \rho c_p}{\lambda}. \quad (5.9)$$

Because of the high heat conductivity  $\lambda$ , liquid metals have a low Prandtl number. Lead at  $600 \text{ }^\circ\text{C}$  has a Prandtl number of  $0.013$ , which is significantly below the given range. Hence, for heat transfer problems, this analogy could not be used. But in the given case, it is a mass and momentum problem, and as already said, the Reynolds number being  $27\,200$  is within the range, and the Schmidt number for lead is  $134$  in this condition. Therefore, it could be expected that the Chilton-Colburn equation (equation 2.9) could be also used for this situation. With this equation, a MTC of  $4.56 \times 10^{-5}$  m/s is estimated, which is equal to a wall loss of  $4600 \mu\text{m}/\text{yr}$ . This is a reasonable overestimation of around  $1.8$ . This is already a better starting point than the correlations from above. Hence, the Chilton-Colburn equation is used for the workflow presented in chapter 4.1. Three months (90 days) erosion time are simulated: the first 2 time steps are 5 days each, the next time steps are 10 days, and the last one is 30 days. The calculated erosion rates for each time can be seen in Table 5.4 and Figure 5.9a. The total erosion time is limited to three months because the expected erosion rate is high. With a measured erosion rate of  $2600 \mu\text{m}/\text{yr}$ , one year would lead to diameter increase of around  $5 \text{ mm}$ , an increase of  $150 \%$ . The deformation of the mesh could be

**Table 5.4:** Erosion rates in  $\mu\text{m}/\text{yr}$  for each time step and the resulting mean erosion rate

Wall loss per year	
Day 0 to day 5	4630 $\mu\text{m}/\text{yr}$
Day 5 to day 10	4429 $\mu\text{m}/\text{yr}$
Day 10 to day 20	4298 $\mu\text{m}/\text{yr}$
Day 20 to day 30	4016 $\mu\text{m}/\text{yr}$
Day 30 to day 40	3775 $\mu\text{m}/\text{yr}$
Day 40 to day 50	3553 $\mu\text{m}/\text{yr}$
Day 50 to day 60	3473 $\mu\text{m}/\text{yr}$
Day 60 to 90	3201 $\mu\text{m}/\text{yr}$
(Day 90	2768 $\mu\text{m}/\text{yr}$ )
Mean Wall loss per year	
Day 0 to 90	3694 $\mu\text{m}/\text{yr}$

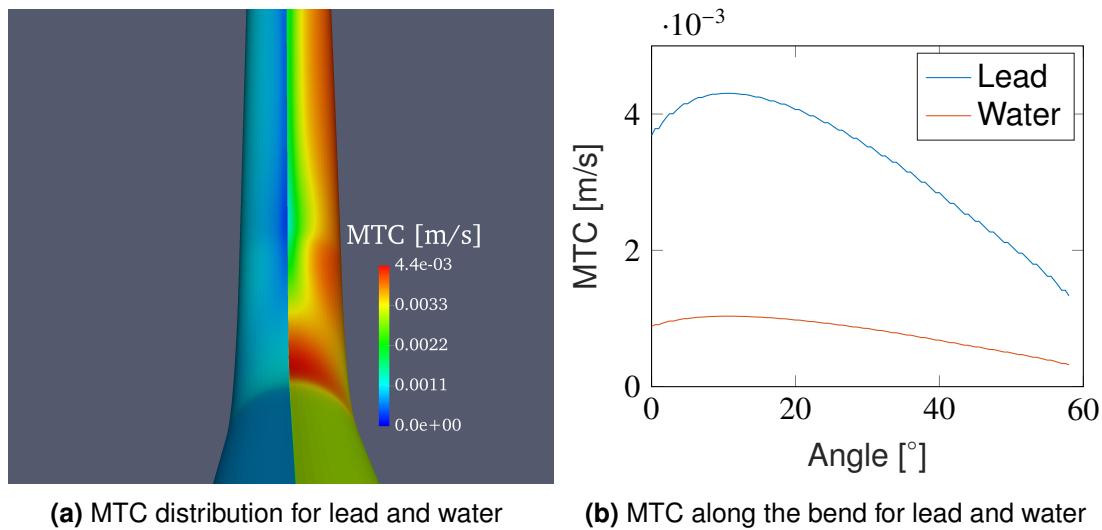


**Figure 5.9:** Development of the corrosion rate and wall loss during the simulated time

too much in that case. Therefore, the simulation time is limited. From Table 5.4 and Figure 5.9, it becomes clear that the erosion rate slows down over time. The first time step is calculated with the already mentioned erosion rate of  $4600 \mu\text{m}/\text{yr}$ . Then the erosion rate steadily drops to  $3201 \mu\text{m}/\text{yr}$ . Averaging the different erosion rates over time leads to a mean rate of  $3700 \mu\text{m}/\text{yr}$ , which is an overestimation by a factor of only 1.4. The calculated total wall loss for the simulated time is around  $910 \mu\text{m}$ . The wall loss leads to an increase of the diameter, and hence, to a decrease of the Reynolds number from 27200 to 22300.

From this application of the workflow, it can be concluded that the developed methodology can provide satisfying results for the estimation of wall loss due to FAC, and because of the dynamic mesh deformation, the MTC can adapt to new flow condition and is therefore in better agreement with the measurements.

To show the high erosion potential of lead in comparison with water, the case from chapter 5.1 is simulated with lead as working fluid, but the flow conditions, e.g. the



**Figure 5.10:** Comparison of the MTC for water and lead as the working fluid

Reynolds number is kept constant for both cases. A direct comparison for the first time step can be seen in Figure 5.10a. On the left side, the MTC of the water case is shown, and on the right, side the lead case is shown. For both cases, the same scale is used. The difference becomes even more clear in the diagram of Figure 5.10. There the MTC is compared along the middle line of the bend. It can be seen that the maximum MTC for lead and water differs by a factor of 4.3. The point of maximum MTC is in both cases at 11°, the point of minimum MTC at 58°, there the MTC for lead is about four times higher than the MTC for water. In terms of corrosion rate, this MTC would be a corrosion rate of 430 mm/yr. The elbow used in the experiment has a wall thickness of 3.7 mm, that means the wall would be gone in about 3 days.

## 5.3 Particle erosion in a 90° Elbow

### 5.3.1 Summary of the Experiment

The experiment for testing the methodology for particle erosion was done by Sedrez et al. (2019). The numerical investigations from this work are already presented in chapter 2.4. In the experiment the particle erosion caused by sand particles, which are transported in a water stream or in water/air flows, has been studied. In this work, the case of pure water with sand particles is used for testing the numerical setup. The test section of the facility consists of a vertical pipe with two 90° elbows mounted in series. Figure 5.11 is a simplified schema of the test section with its dimensions. The pipe has an inner diameter of  $D = 50.8$  mm, and the bend radius of the elbows are 76.2 mm. Between the two elbows there is a distance of  $3D_i$ . The water is supplied by a tank and two air operated diaphragm pumps, which are used to pump the water from the tank into the test section. The volume flow is measured with a flow meter. Upstream of the test elbow, the sand sampling port is located where the sand particles are injected. The sand concentration

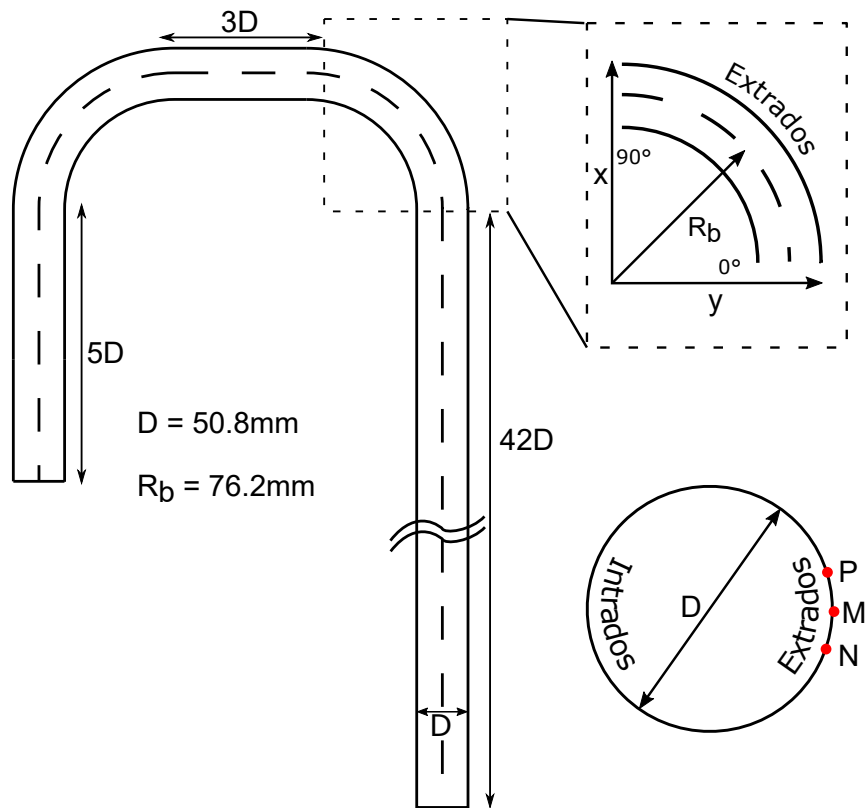


Figure 5.11: Overview of the geometry from Sedrez et al. (2019)

is measured at six locations across the pipe, upstream of the test elbow. From these measurements the particle volume concentration was calculated. For the given experiment the particle volume concentration is 0.37%. Only the first elbow is the elbow of interest in this experiment. After the experiment, the loss of the wall thickness is measured with a handheld ultrasonic thickness gauge. The wall thickness was measured along three lines around every  $4.5^\circ$  at the bend before and after the experiment. The results of these measurements were averaged. The radial position of the lines (M,N,P) are shown in Figure 5.11. This experiment took about 34 h and was performed with a water mass flow rate of 12.7 kg/s. The injected sand particles have a density of  $2650 \text{ kg/m}^3$ , the mean particle diameter ( $d_{50}$ ) is  $300 \mu\text{m}$ . The particle mass flow rate is 0.1285 kg/s. The key flow parameters and the essential geometry parameters of the experiment are summarized in Table 5.5.

### 5.3.2 CFD Calculations and Modelling of the Erosion

The overall procedure for CFD calculations with the Euler-Lagrangian approach is described in the chapters 3.1. For this simulation, the Eulerian steady state simulation was carried out with the so called Semi Implicit Method for Pressure Linked Equation (SIMPLE) algorithm and the  $k-\omega$ -SST turbulence model. The turbulence model is chosen because of its good behavior near the wall. The simulation near the wall is crucial for the erosion modeling because the particle impact velocity, impact angle, and rebound, is influenced by this prediction of the flow. With the consecutive Lagrangian simulation, the particle motions are

**Table 5.5:** Key parameters of the numerical and experimental investigation from Sedrez et al. (2019)

<b>Geometry</b>	
Typ	elbow
Bend angle	90°
Inner diameter $D_i$	50.8 mm
Bend radius $R_b$	76.2 mm
Construction material	Stainless steel 316
Density	7800 kg/m <sup>3</sup>
<b>Conditions</b>	
Fluid	water
Liquid mass flow	12.8 kg/s
Particle	sand
Particle diameter (mean)	300 $\mu$ m
Particle density	2650 kg/m <sup>3</sup>
Particle mass flow	0.1285 kg/s
Particle volume concentration	0.37 %

determined. In this simulation step, the particle erosion, as well as the particle rebound, is modelled every time a particle interacts with the boundary wall. A one-way coupling is used for the simulation. As erosion model, the erosion model of Ahlert (1994) and the rebound model of Forder et al. (1998) are used. In the Lagrangian simulation, the time step is set to 0.001 s, which is considered to be small enough to get a stable result. Starting with the simulation, in each time step 10 000 particles per second are injected over a time period of 10 seconds, resulting in a total number of 100 000 particles and a total mass of 1.285 kg, which is the given mass flow of 0.1285 kg/s. The number of the injected particles is sufficient to capture all the stochastic effects of the particle erosion phenomenon. After the 10 seconds injection time, the simulation continues for another 5 seconds, to let all particles leave the computational domain, so a total physical time of 15 seconds is simulated. The results of the initial simulation can be seen in the Figure 5.12. In Figure 5.12a, the qualitative distribution of the wall loss rate can be seen. There it becomes clear that most of the erosion happens at the end of the bend, near 90°. In Figure 5.12b, the quantitative results along the measurement lines and the result of the averaged line are shown. As expected the wall loss increases along the bend and has its maximum at 88°. After the maximum, the erosion decreases sharply. It has to be mentioned that the middle line has local maxima at around 63° and 80°. All lines have their maximum at the same position. The middle line has a maximum of 0.05 mm/day, and the averaged line has a wall loss rate at the maximum of 0.046 mm/day.

With this initial simulation, the workflow from chapter 4.1 can be applied. The mesh is deformed according to the distribution of the simulated erosion rate. In Figure 5.13, the averaged results for four different times are shown and compared. In Figure 5.13a, the erosion rate from the undeformed mesh is compared with the erosion rate after one day, and in the diagram of Figure 5.13b the erosion time is quadrupled twice (four days and 16 days). The extrapolation is for sure extreme

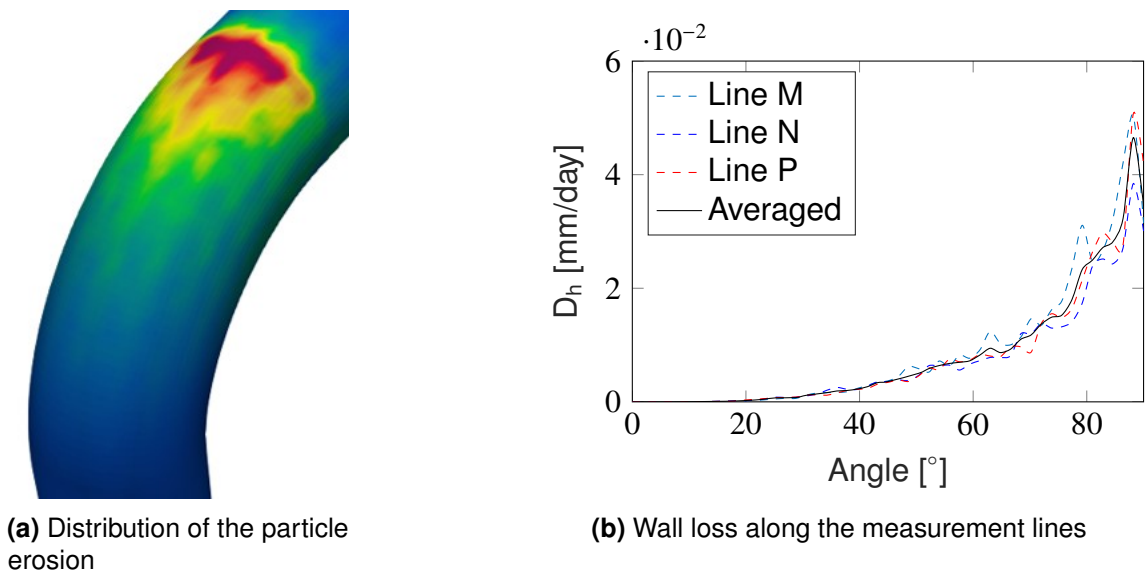


Figure 5.12: Qualitative and quantitative distribution of the wall loss rate

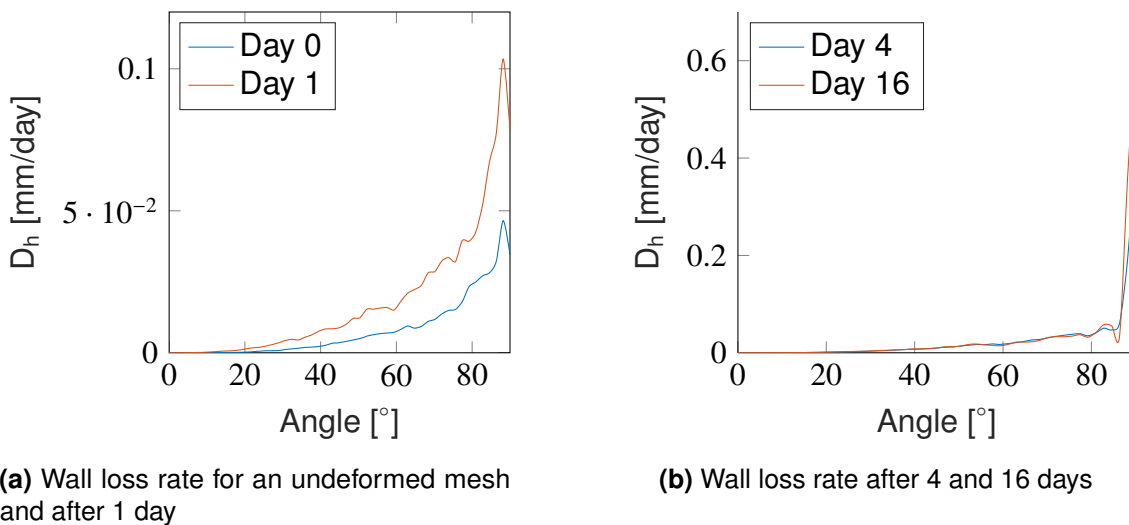
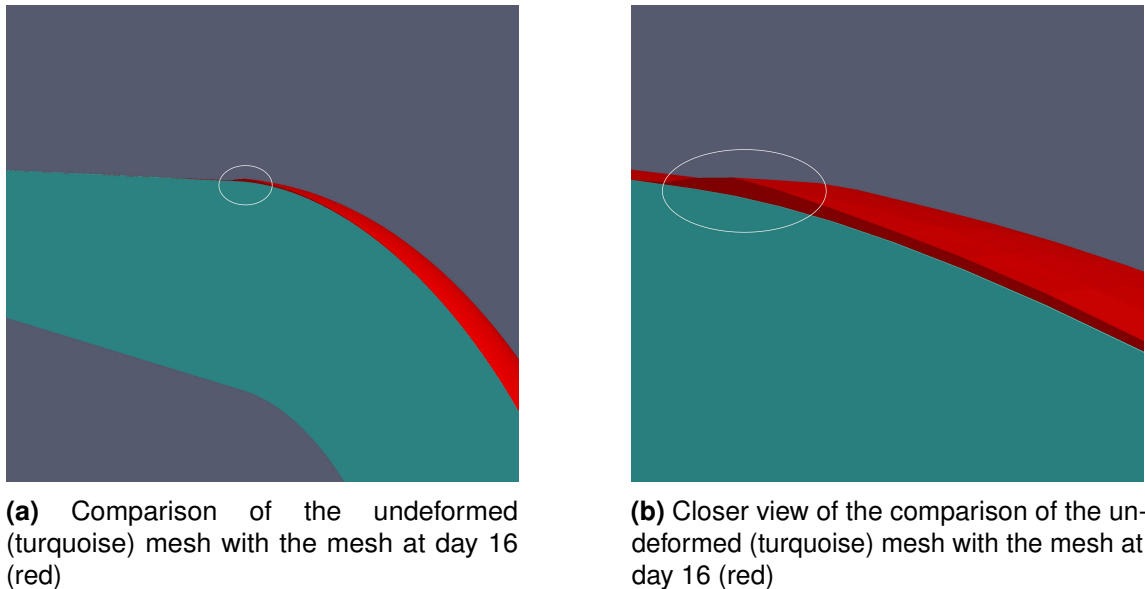


Figure 5.13: Extrapolated behavior for different days





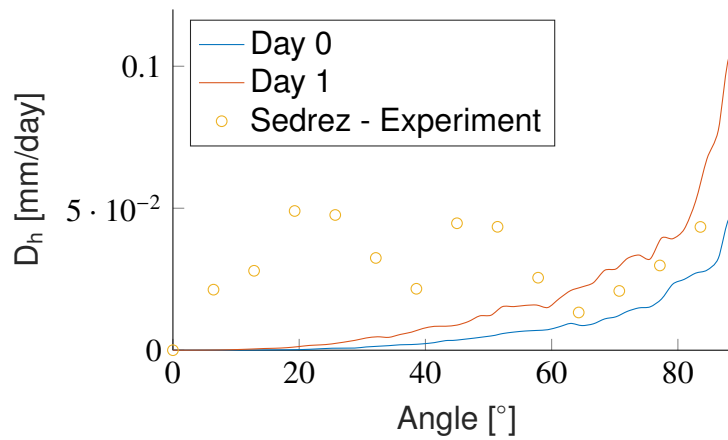
**Figure 5.14**

compared to the 34 h of experimental time. Therefore, this extrapolation should be seen more as a proof of concept. Compared to the experimental time, the simulation was extrapolated by around 3 times (four days) and 23 times (16 days). Sedrez et al. (2019) emphasize that to reach a experimental time of 34 h, it took them nearly four weeks in real time to achieve the experimental time. This means, assuming the experimental set-up of Sedrez et al. (2019), an experimental time of four days would already take a trimester in real time.

In Figure 5.13a, it can be seen that the erosion rate increases after the deformation. Also erosion rate starts to increase early in the bend, at day 0 the erosion starts to matter after  $30^\circ$ , after day 1, there is already at  $20^\circ$  a noticeable erosion rate. For both simulations, the maximum erosion rate is still at  $88^\circ$ , but compared to the undeformed mesh, the maximum erosion rate of 0.1 mm/day is more than double the erosion rate of the undeformed mesh. The further extrapolated meshes in Figure 5.13b show no significant change for most of the bend. The erosion rate remains nearly the same from 0 to  $85^\circ$ . After  $85^\circ$ , the erosion rate increases sharply to 0.4 mm/day (four days) and 1 mm/day (16 days). The maximum also moves completely to the end of the bend. The reason for the sharp increase can be seen in Figure 5.14, in Figure 5.14a the  $90^\circ$  elbow of interest is shown, the turquoise elbow shows the outline of the undeformed mesh, and the red elbow the deformed mesh after 16 days. Figure 5.14b shows the close up of the end of the bend of the same situation. There it can be seen that for the red mesh a pocket is formed at the end of the bend; a pocket where the particles impact angle is much steeper, and therefore, a much higher erosion rate is the consequence. As the development shows, this is a self-reinforcing process.

### 5.3.3 Comparison of the Experiment with the CFD Modelling

In this section, the CFD modelling is compared with the measurements of Sedrez et al. (2019). In Figure 5.15, the measured wall loss rates and the calculated



**Figure 5.15:** Wall loss rate of the simulation at day 0, day 1, and of the experiment (34h)

wall loss rates for day 0 (undeformed mesh) and days 1 (deformed mesh) are shown. For the numerical investigation, the erosion rate increases in a parabolic way. This clear trend is missing for the experimental data, besides the increase towards the end of the of the bend. According to Sedrez et al. (2019), the missing of this trends can be lead back to the short experimental time, and they expect this steadily increasing trend for longer experimental times. However, the magnitude of the particle erosion can be predicted reasonably by the numerical simulation. Between 60 and 90°, the calculated results have a similar shape compared to the experimental results. The unreformed mesh underpredicts the magnitude of the erosion, the maximum erosion rate for the middle line is 0.05 mm/day. This is less than half of the 0.12 mm/day measured maximum rate. The erosion rate after 1 day fits well with the experimental results in this area, the slope of the increase is slightly overpredicted but follows the experimental results. Also the magnitude and location of the maximum erosion rate with 0.13 mm/day is in accordance with the measured results.

With this results, it can be concluded that the presented workflow leads to better and more accurate predictions than compared to a modeling without a mesh deformation process. The deformation of the mesh can reproduce self-reinforcing processes like the developing pocket at the end of the bend. A normal, numerical investigation without a mesh deformation would not be able to catch this situation. Also the numerical investigation is able to predict the point of maximum erosion and magnitude well.

For future investigations, the extrapolation time could be done in smaller steps to investigate the influence on the developing pocket. This numerical investigation, in this respect, is a proof of concept investigation for the presented framework. Also, two-way coupling investigations could be done and also a closer look on the particles themselves. Sedrez et al. (2019) specify the particle size of the sand with a  $d_{50}=300\ \mu\text{m}$ , therefore, for the numerical investigation this diameter was used for the particles. Normally, particles have a size distribution, often a log-normal distribution. The influence of different size distributions on the erosion rate could also be investigated in the future.

# 6. Pump Investigation in Regards of Erosion Minimization

This chapter deals with centrifugal pumps in general, and with centrifugal pumps in (heavy) liquid metal applications in particular. The numerical investigations have the aim to investigate the flow behavior of centrifugal pumps in respect to erosion phenomena. The focus of this chapter is the development and distribution of the Wall Shear Stress (WSS) as the main driving factor for high FAC rates. The numerical calculations for pumps were done according to the procedure described in chapter 3.1.2 and 3.3. The structure of this chapter is shown in Figure 6.1. The aim of the first part of the chapter is to validate, verify the used numerical method, and used geometry tools. The second part deals with the simulation results, especially with the distribution of WSS.

## 6.1 Pump Characteristic

In chapter 2.3, the pump characteristic is described in detail. In this short section, the calculation of the pump characteristic for the numerical simulations is described and how the simulations are evaluated to get a pump characteristic, comparable to the one shown in Figure 2.9. The evaluation is done by a so called *functionObject*. *functionObjects* are utilities in OpenFoam for automatic evaluation during or after the calculation as a post processing step. The used *functionObject* is called

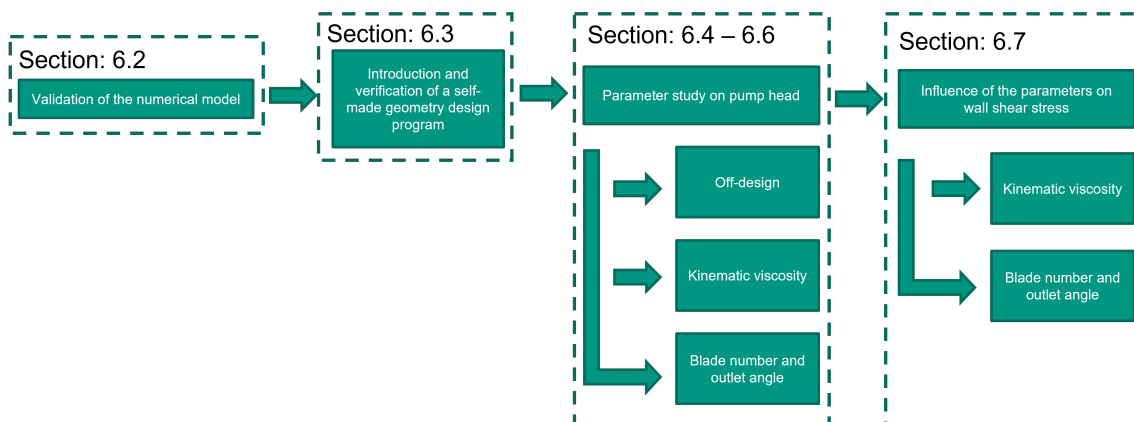
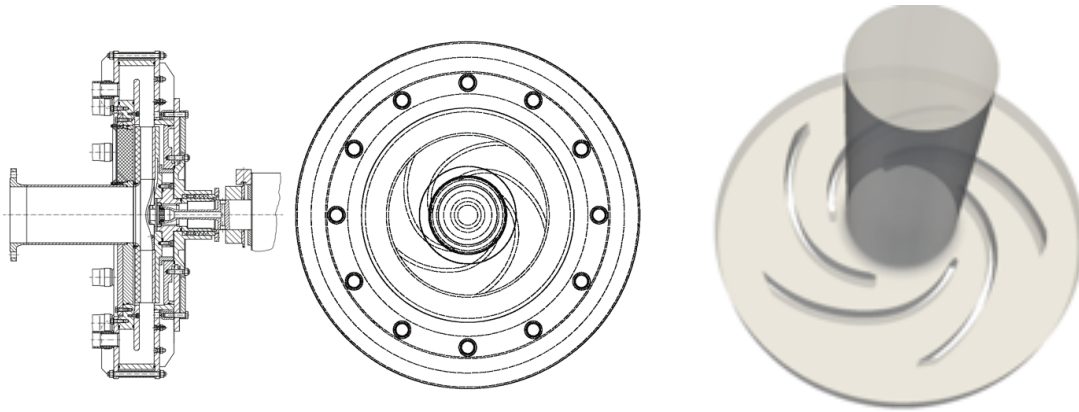


Figure 6.1: Pump investigation in regards of erosion minimization



(a) Cross section of the pump used by Suryawijaya et al. (2000) for experimental investigations (according to Müller et al. (2015)). (b) 3D model used for the CFD simulations.

**Figure 6.2:** Geometry of the pump<sup>1</sup> used for validating the CFD models.

*Turbomachinery Library turboPerformance* and was written especially for the evaluation of turbo-machines (Auvinen et al., 2011). The original version from Auvinen et al. (2011) was adapted, so it can run on the used OpenFoam version. The required quantities of a pump characteristic head  $H$ , power  $P$ , and efficiency  $\eta$  are calculated as described in the following (Auvinen et al., 2011):

$$P = P_{M,Outlet} + P_{M,Inlet}. \quad (6.1)$$

$P_M$  is the flow of the mechanical energy at the outlet and at the inlet, respectively. The in- and outflow of the mechanical energy are defined as

$$P_{M,Outlet} = \rho_f \sum \Phi_b P_{t,outlet} \quad (6.2)$$

and

$$P_{M,Inlet} = -\rho_f \sum \Phi_b P_{t,Inlet}. \quad (6.3)$$

As it can be seen from above's equations, the energy at the inlet is defined negative and at the outlet positive. For pumps, where energy is added to the fluid, the power  $P$  is positive. For other turbo-machines, like turbines, where energy is withdrawn from the fluid, the power would be negative.  $\rho$  is the density of the fluid,  $\sum \Phi_b$  is the sum of all face fluxes at each boundary, and  $P_t$  is the total pressure divided by the density. It is defined as:

$$P_t = \frac{p_b}{\rho_f} + \frac{u_b^2}{2} \quad (6.4)$$

where  $p_b$  is the static pressure at the boundary and  $u_b$  the velocity at the respective boundary. The pump head is calculated with

$$H = \frac{P}{-\dot{m}_{f,Inlet}g} \quad (6.5)$$

<sup>1</sup>Müller et al. (2015) published under an open access licence, which permits the reuse.

## 6. Pump Investigation in Regards of Erosion Minimization

Erosion conditions		Pump geometry data	
Flow rate $Q_{opt}$	412 m <sup>3</sup> /h	Inlet diameter	0.26 m
Head <sub>opt</sub>	10.16 m	Outlet diameter	0.556 m
Rotational speed $n_{opt}$	540 min <sup>-1</sup>	Inlet width	0.046 m
Specific speed $n_q$	32 min <sup>-1</sup>	Outlet width	0.046 m
		Blade inlet angle	19 °
		Blade outlet angle	23 °
		Blade number	5

**Table 6.1:** Key parameter of the pump investigated by Suryawijaya et al. (2000).

where  $\dot{m}$  is the mass flow at the inlet and  $g$  is the free fall acceleration (9.81 m/s<sup>2</sup>). Finally, the efficiency of the pump is defined as

$$\eta_p = \frac{P}{T \cdot \omega} * 100 \quad (6.6)$$

where  $T \cdot \omega$  is the needed power at the shaft of the pump.

For generating the pump characteristic, a range of different flow rates have to be simulated and evaluated. The simulated flow rates can normally be found in a range of between 60% and 120% of the optimal flow rate  $Q_{opt}$ .

### 6.2 Validation of the Numerical Method

For the validation of the CFD model (based on chapter 3.3), a real pump geometry was used with water as a working fluid because of the lack of liquid metal experiments in this field. The pump was used by Suryawijaya et al. (2000) for experimental investigations and by Müller et al. (2015) for numerical investigations. Müller et al. (2015) provided the original CAD-model of the pump after Suryawijaya et al. (2000), as the owner, agreed to this exchange. This pump has a optimal flow rate  $Q_{opt}$  of 412 m<sup>3</sup>/h, a head  $H_{opt}$  of 10.16 m, and a rotational speed  $n$  of 540 m<sup>-1</sup>. All key parameters are summarized in Table 6.1. The cross section of the pump is shown in Figure 6.2a, and the used 3D model is shown in Figure 6.2b. As it can be seen from these figures, the geometry was kept simple, and from the table it is known that it is a pump with a rather low specific speed. The validation of the CFD model was done with the commercial code Ansys CFX (Zhexin, 2018) (Constien, 2018) as well as with OpenFOAM. The simulation results for the pump head, compared with the experiment, are shown in Figure 6.3. The CFD results nearly agree with each other over the whole range of the simulated flow rates. It is noticeable that there is an overestimation compared to the experimental results. This can be explained with the simplification of the geometry for the CFD calculation, whereby no leakage flows can occur. With this simplification, the higher pump head can be justified, and therefore, this behavior is not surprising. Nevertheless, the simulations follow the experimental results qualitatively, and the results are only shifted parallel to higher heads. Due to the matching results with the results from the CFX calculations, which are based on the validated calculations from

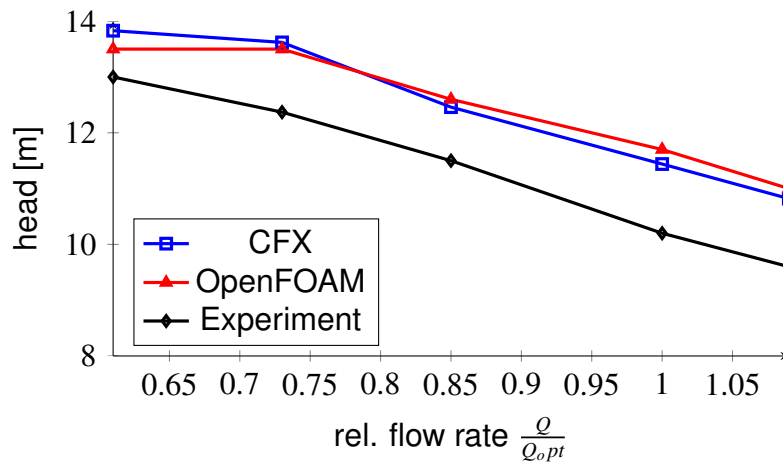


Figure 6.3: Simulated head vs. measured head

Müller et al. (2015), and the explainable differences to the experimental results, it can be said that the used models in the OpenFOAM calculation are valid for the simulations.

### 6.3 Geometry Design

In section 6.2, it was shown that the used numerical set-up is suitable for calculating the head of a centrifugal impeller. In this section, a program for modelling generic pump impellers, which was written in the course of this work, is introduced and tested. The essential concept of the program is shown in Figure 6.4: With only the four parameters

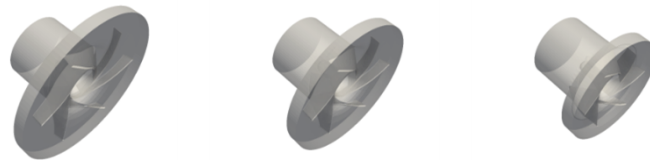
- Desired flow rate  $Q_{opt}$  [ $m^3/h$ ]
- Desired head  $H_{opt}$  [m]
- Rotational speed  $n$  [1/min]
- Fluid density  $\rho$  [ $kg/m^3$ ]

it is possible to generate a basic CAD model of a pump impeller in one step which can be used for numerical investigations. Although the density of the fluid could be changed by the user, this would influence the diameter of the shaft, but for this report the density is fixed to  $1000 kg/m^3$  (the density of water) due to better comparability. The aim of the program is also to make the generation of different pump impellers as flexible as possible, so that the geometry parameters can be changed easily and conveniently. The design of the impeller is based on the book "Centrifugal Pumps" by Gülich (2014a). This book describes, based on empirical equations and guidelines, the outlay of the different parts of a pump. The different equations and guidelines for a pump impeller, together with a front and back shroud, are transformed into a *Python* script. With this script, and the open source CAD tool *FreeCAD*, it is possible to generate the different CAD models of a pump impeller quickly and easily. Another advantage of this script based CAD modelling

## 6. Pump Investigation in Regards of Erosion Minimization

**Table 6.2:** Main dimensions and parameters of pumps with different specific speed (according to Schenk et al. (2018c))

Parameter	$n_q=31.5 \text{ min}^{-1}$	$n_q=43 \text{ min}^{-1}$	$n_q=72 \text{ min}^{-1}$
Flow rate $Q_{\text{opt}}$		280 m <sup>3</sup> /h	
Head $H_{\text{opt}}$	30 m	20 m	10 m
Rotational speed $n$		1450 1/min	
Shaft diameter	0.026 m	0.023 m	0.020 m
Inlet diameter	0.172 m	0.171 m	0.170 m
Outlet diameter	0.33 m	0.28 m	0.22 m
Blade height at inlet	0.066 m	0.068 m	0.070 m
Blade height at outlet	0.030 m	0.032 m	0.037 m



CAD model

is that all key characteristics are parametrized and can be handled separately: key characteristics, like the number of blades or the different angles of the blades, but also parameters like the maximum allowed shear stress of the construction material, which influences the shaft diameter. The influence of these parameters on the pump's behavior can be investigated with such a program very efficiently. Theoretically, this purely open source based tool can be compared to a simplified version of the commercial program ANSYS Vista (VISual Turbomachinery Analysis - Centrifugal and mixed-flow pump Preliminary Design). The advantage of a self-written program is that the functionalities and the dependencies of each parameter are known better. Also, the parameters can be changed more easily and especially more flexibly without any external restrictions of a given program.

For categorizing centrifugal pumps, one important characterisation for pumps is the already in chapter 2.3.3 introduced specific speed. This number allows to compare different pumps with each other. Impellers with the same specific speed have a similar qualitative behavior in terms of design and characteristic curves. To get an impression of how the shape of a impeller is influenced by the specific speed, three examples of pumps with different specific speeds can be seen in Table 6.2. For these examples, the flow rate and the rotational speed are fixed, and only the head of the pump is varied. From the CAD models, which are all generated automatically by the *Python* script, it can be seen that for low specific speeds the outlet diameter is larger than for higher specific speeds, whereas for the blade height, it is the other way around. In the following, the pump with the specific speed of  $n_q = 43 \text{ min}^{-1}$  is used. The basic design is a 6-bladed impeller, but also four and five-bladed designs are analyzed concerning the behavior towards the head capacity and WSS.



## 6. Pump Investigation in Regards of Erosion Minimization

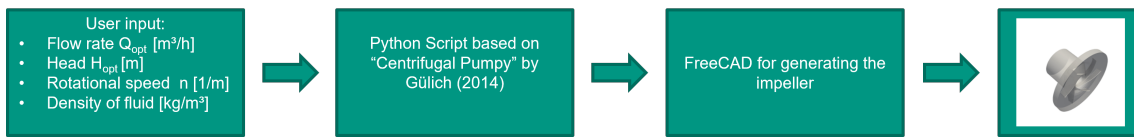


Figure 6.4: Schema for the generation of a pump impeller CAD model.

### 6.3.1 Verification of the Geometry Design

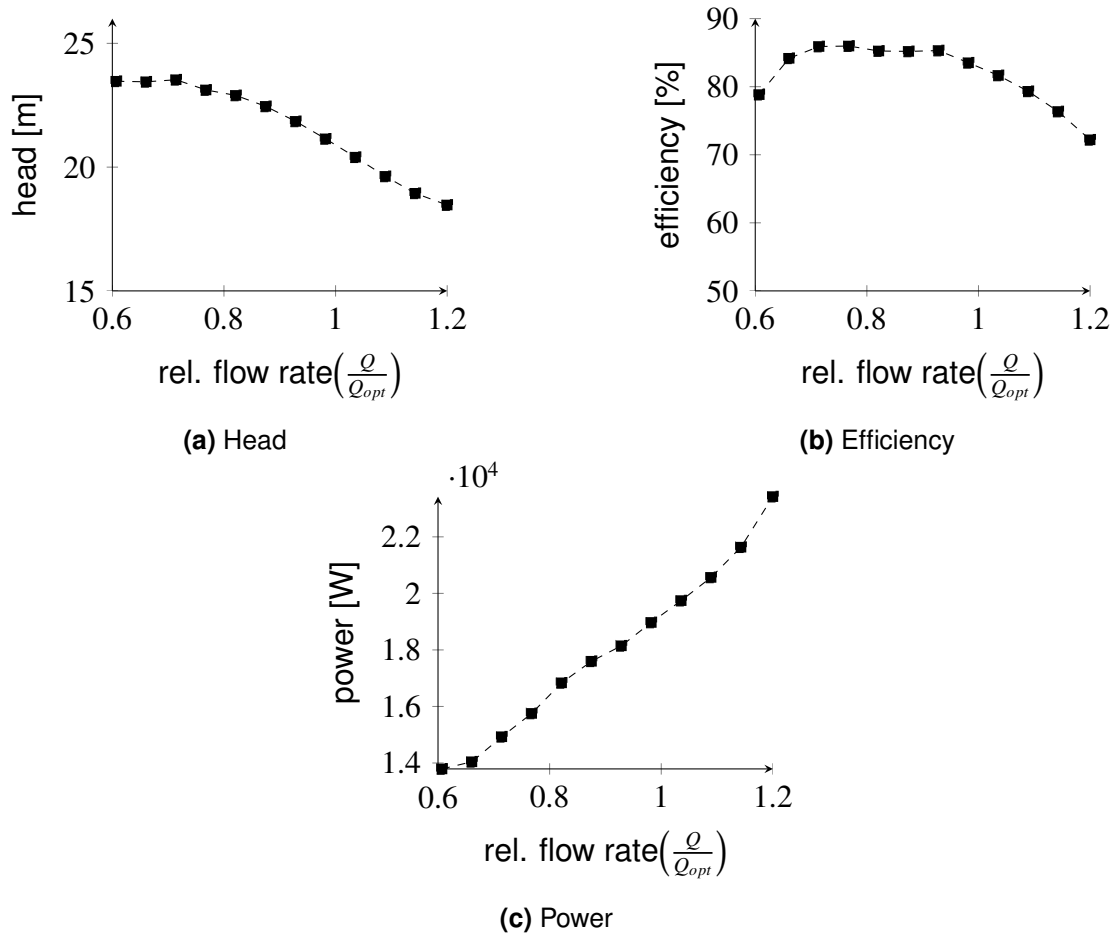
In this section, the program has to be tested if it is able to generate a geometry which has the desired properties given by the user. As already mentioned, the pump with a  $n_q$  of  $43 \text{ min}^{-1}$  from Table 6.2 is used for this work, therefore, the testing of the program is also shown for this geometry. After the geometry is generated with the desired properties, different CFD calculations with different flow rates, have to be done for the characteristic curve. As a working fluid water was used; In terms of CFD calculations this means that the kinematic viscosity of water and, later in a post-processing step, the density of water are used. The calculated flow rates vary between 0.6 and 1.2 times of the design point's flow rate, e.g. from 170 to  $340 \text{ m}^3/\text{h}$ . This has two reasons, one reason is that this is the typical off-design range pumps have to operate, and the second reason is that for lower flow rates unsteady effects become more and more important, so steady-state solutions are no longer physically meaningful, and hence, convergence problems can occur. In an automated post-processing step, the different calculations were put together to a characteristic curve. The outcome is illustrated in Figure 6.5. As shown in Table 6.2, this pump should have its design point at a flow rate  $Q_{\text{opt}}$  of  $280 \text{ m}^3/\text{h}$ , and a head  $H_{\text{opt}}$  of 20 m, and with a specific speed of  $43 \text{ min}^{-1}$ , the characteristic curve should be qualitatively similar to the generic curve shown in Figure 2.9. Additionally, according to Güllich (2014a) for this pump design, an efficiency  $\eta$  and optimal power  $P_{\text{opt}}$  of 84% and 18 kW, respectively, can be expected at the design point. According to Figure 6.5, the calculated values at the design point are:

- $H_{\text{opt,CFD}} = 20.3 \text{ m}$
- $P_{\text{opt,CFD}} = 19 \text{ kW}$
- $\eta_{\text{opt,CFD}} = 83 \%$

These values are close to the expected values, and also the shape of the characteristic curve comes close to the one shown before. But there are also differences between the calculated and the curve from Figure 2.9. As it can be seen, the characteristic curve generated by CFD calculations has a broad range between 70% and 100% of  $Q_{\text{opt}}$  where the efficiency  $\eta$  is higher than 80%. The calculated maximum efficiency is between 70% and 100% of  $Q_{\text{opt}}$ . At  $Q_{\text{opt}}$  the efficiency is already dropping, and at  $0.8Q_{\text{opt}}$  it is at around 85%. The calculated head of 20.3 m at the design point matches well with the expected 20 m, and the calculated 19 kW are in good agreement with the predicted 18 kW. So all in all, it can be said that the simplified CAD-modelling and the CFD-models provide results which are in line the predicted results from the textbook.



## 6. Pump Investigation in Regards of Erosion Minimization



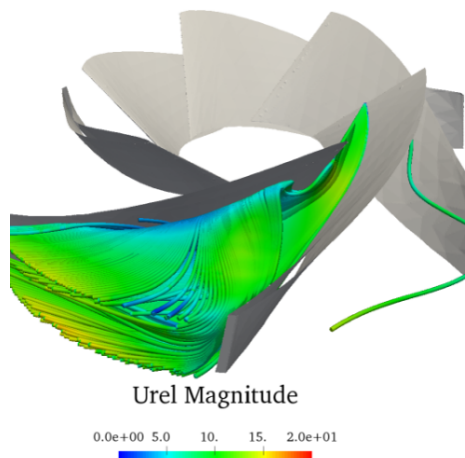
**Figure 6.5:** Pump characteristic with water as working fluid (according to Schenk et al. (2018c))

## 6.4 Recirculation at Off-Design Flow Rates

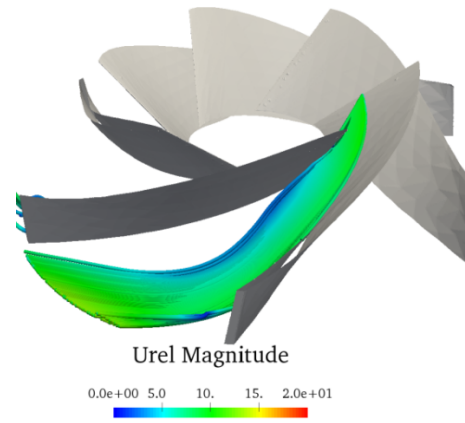
Recirculation occurs at reduced flows. The head of an impeller is a composite of the centrifugal head and the dynamic head. The centrifugal head is independent of the flow rate but not the dynamic head, which is a function of the velocity, and hence, a function of the flow rate. For low flow rates, the centrifugal head will exceed the dynamic head at some point. At this point, the pressure field is not symmetrical, and recirculation can happen. The recirculations occur near the suction side of the blades, and the small reversed part of the main flow induces vortices which rotate, together with the impeller blades (Fraser, 1981). This flow regime is not steady, but because the vortices rotate with the impeller, it can be described as somehow quasi-stationary, and therefore, a steady-state approach can give an idea of how the recirculation looks like and when this phenomenon occurs. The difference of the flow behavior between on-design condition and low flow rate condition can be seen in Figure 6.6. The origin of the stream lines in Figure 6.6a and 6.6b are a line between two neighboring blades to show how the flow develops. It can be seen that near the design point the stream lines are well aligned with the blades, and the stream lines fill the whole volume between the blades. The stream line plot with the same source points looks totally different under low flow rate conditions, which can be seen in Figure 6.6b. There the stream lines are not well aligned with the blades anymore. The stream lines, which come from the blade tips, bend around the suction side of the blade, which means that there is a vortex with only low fluid exchange with the main flow. The velocity vector-field plot of the mid plane (Figure 6.6c and 6.6d) confirms this assumption, the vortices can be seen clearly in Figure 6.6d. Whereas in Figure 6.6c there is only small disturbance in the velocity field at the tip and at a small region behind the edge, the eddy water region in Figure 6.6d fills a large part of the space between the two blades. This examination shows that, although it is a transient process, the steady-state approach can deal with this kind of flow regime and can be used to study it further, and use this phenomenon together with the already discussed wall shear stress distribution as a starting point for an optimization process.

## 6.5 Influence of the Kinematic Viscosity on the Pump Parameters

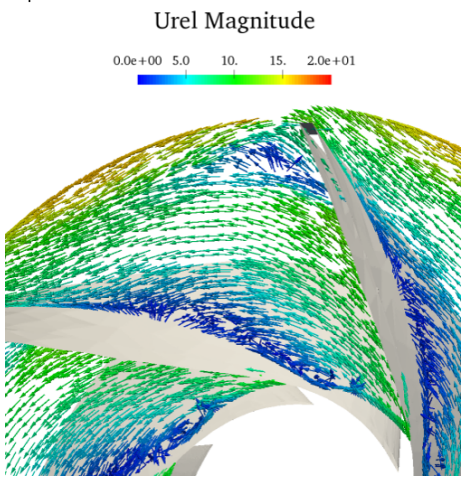
As already written in the introduction of this chapter, the aim of this part is not only to investigate the flow behavior of centrifugal pumps in respect to erosion phenomena, but also to investigate the behavior of centrifugal pumps with (heavy) liquid metals as the used working fluid. As mentioned before, the OpenFoam solver only needs the kinematic viscosity of the used fluid for simulations, therefore, only the kinematic viscosities of the metals are needed to change the working fluid from water to a liquid metal. The properties can be found in Table 2.2. To evaluate the general influence of the kinematic viscosity on the simulations, a broad range of different generic kinematic viscosities were simulated and analyzed at the design point. It should be also mentioned that with the change of the viscosity the



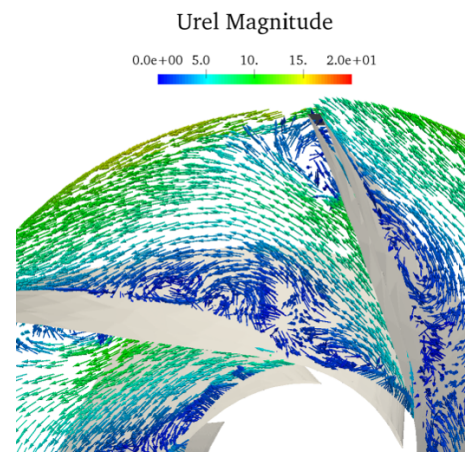
(a) Stream lines between two blades for  $Q_{opt}$



(b) Stream lines between two blades for  $0.6Q_{opt}$



(c) Velocity vector-field plot between two blades for  $Q_{opt}$



(d) Velocity vector-field plot between two blades for  $0.6Q_{opt}$

**Figure 6.6:** Stream lines and vector plot under design point conditions and under low flow rate condition

## 6. Pump Investigation in Regards of Erosion Minimization

---

Reynolds number is also changed. Normally the Reynolds number is defined as

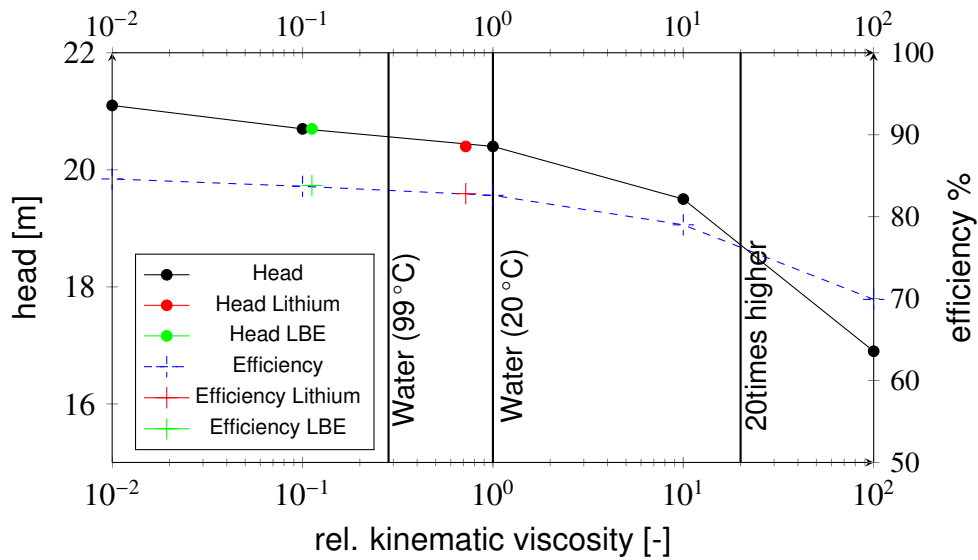
$$Re = \frac{uD}{\nu} \quad (6.7)$$

where  $u$  is the velocity of the fluid,  $\nu$  is kinematic viscosity, and  $D$  is the characteristic length. In case of centrifugal pumps, the characteristic length is the diameter of the impeller (Stepanoff, 1957b). For the same flow rate, the Reynolds number is only dependent on the kinematic viscosity. The results of the simulations with different kinematic viscosities can be seen in Figure 6.7. The head and efficiency of the pump at a flow rate of  $280 \text{ m}^3/\text{h}$  over the relative kinematic viscosity is illustrated. The relative viscosity is defined as

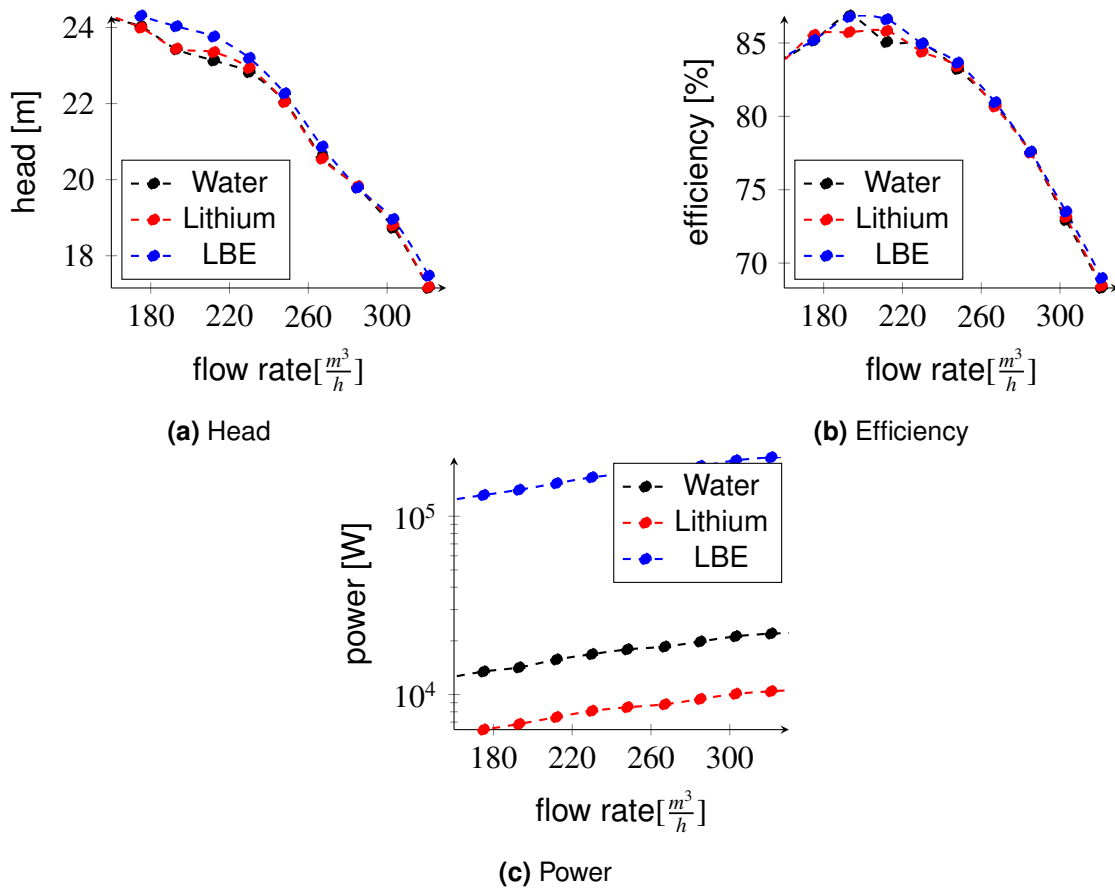
$$\nu_{rel} = \frac{\nu_{Fluid}}{\nu_{Water,20^\circ\text{C}}}. \quad (6.8)$$

From Figure 6.7, it can be seen that viscosities were calculated in a range 100 times lower and higher than the viscosity of water at  $20^\circ\text{C}$ , or in other terms, it can be said that at the same time the Reynolds number is varied by a factor of 10 000. From this diagram, it can be derived that for lower viscosities than water at room temperature, the influence on the head and efficiency is insignificant. Even if the viscosity is **100 lower**, there is only a rise of the efficiency from 83 to 85 % and for the head a rise from 20.4 to 21.1 m, which is a rise by 2.5 and 3 %, respectively. In contrast, a clear influence on the pump characteristics can be seen for viscosities which are about **ten times higher** than the kinematic viscosity of water at  $20^\circ\text{C}$ . There the head already drops to 19.5 m and the efficiency to 79 %, which is a drop by 4.4 and 5 %, respectively. If the viscosity is 100 times higher, the loss of head and efficiency is even more significant. This behavior of the simulation is confirmed by professional pump developers ((KSB SE & Co. KGaA, 2019) and Sadegh, 2018). There an adjustment of the pump is suggested if the fluid has a kinematic viscosity 20 times higher than water at  $20^\circ\text{C}$ . The liquid metals in question, however, have lower kinematic viscosities than water (see Table 2.2). Water at  $99^\circ\text{C}$  and atmospheric pressure has a kinematic viscosity of  $0.295 \times 10^{-6} \text{ m}^2/\text{s}$  (calculated according to SATO (*VDI-Wärmeatlas* 2013)), which is three times lower than water at  $20^\circ\text{C}$ . In other words, it is in the same range as liquid metals, which can be found in a range of  $0.72 \times 10^{-6} \text{ m}^2/\text{s}$  (Lithium) and  $0.11 \times 10^{-6} \text{ m}^2/\text{s}$  (LBE). Therefore, only a low influence is expected, and, as it is also illustrated in Figure 6.7, the head and the efficiency for Lithium and LBE differ only marginally from the pump parameters with water as a working fluid at the design point. For that reason, the whole pump characteristic of water and liquid metals are more or less the same, only the needed power differs because the power is directly proportional to the density of a fluid, which means that the power curve of LBE is shifted by the order of about ten. This expected behavior is confirmed by the calculated pump characteristic for the three fluids in Figure 6.8.

## 6. Pump Investigation in Regards of Erosion Minimization



**Figure 6.7:** Influence of the kinematic viscosity on the pump parameters at a flow rate of  $280 \text{ m}^3/\text{h}$  (according to Schenk et al. (2018c))



**Figure 6.8:** Characteristic curve for LBE, lithium and water

## 6.6 Impeller Performance with Different Blade Number and/or Outlet Angle

In this section, the influence of different geometric factors on the pump performance are investigated and discussed. First, the number of impeller blades are changed, and then the outlet angle is changed.

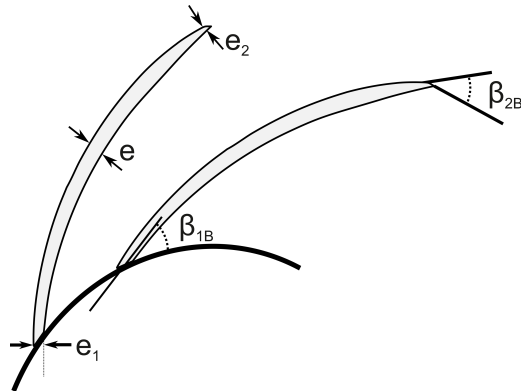
The number of impeller blades can not be changed solely. A change of the blade number leads directly to a change of various other parameters like blade thickness or blade outlet angle (Wesche, 2016b). A simplified depiction of the impeller and its parameters is shown in Figure 6.9. Hence, a variation of the impeller blades is equivalent to varying of the shape of one single blade. The calculated outlet angle  $\beta_{2B}$  for the different blade numbers differs from  $22^\circ$  (six blades) to  $32^\circ$  (four blades). According to the literature, a small outlet angle should make the head capacity curve of the impeller steeper, but at the same time, a smaller number of blades has the same effect, that means these two parameters will overlay each other (Wesche, 2016b). The results of the numerical analysis for the head performance curve can be seen in 6.10a. It is illustrated that for smaller blade numbers the curve is flatter than for higher blade numbers. In the part load region, the head of the impeller with fewer blades is lower than the head of the impeller with more blades. Due to the different steepness of the H-Q-curves, the curves meet each other in the slightly overload region of around 1.1 to 1.2 of  $Q_{opt}$ . The trend of higher head changes, and after the intersection of the curves the impeller with more blades has a higher head.

In the next step the number of blades is fixed (5), and the dependence of the outlet angle on the blade number is switched off in the program but not the dependencies, which are affected by a change of the outlet angle. The single blade can therefore change its shape according to the outlet angle. Normally, the introduced program calculates an outlet angle for a 5-bladed impeller of  $27^\circ$ . In Figure 6.9, the outlet angle is marked with  $\beta_{2B}$ . This angle is changed manually to  $23^\circ$  and  $31^\circ$  to investigate its influence. The results can be seen in Figure 6.10b. Here the already mentioned behaviour of blades with different outlet angles can be seen. For lower angles the H-Q-curve is steeper than for higher angles.

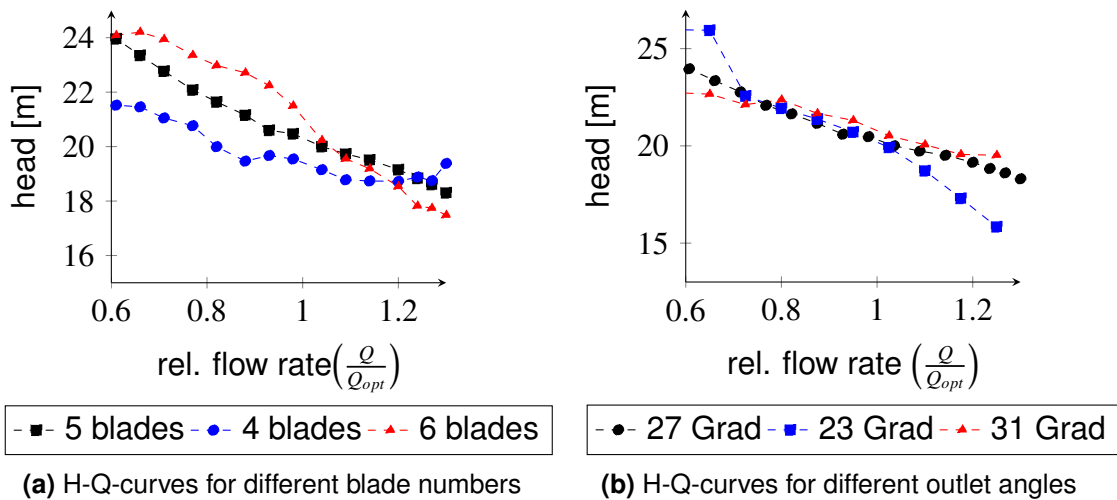
In general, H-Q-curves can be distinguished in stable curves and unstable curves. Stable curves are curves which are monotonically decreasing, in other words, steep curves are not in danger to become instable, whereas flat curves can become instable more easily and should be avoided. Curve instabilities are a sign of unwanted recirculations near the design point.

## 6.7 Influence on the Wall Shear Stress

In the sections before, the influences of different geometric parameters and fluids on the performance of the impeller were discussed, and numerical results were compared to the behavior described in literature. Hence, the simulations were in accordance with the expected behavior, and hence, it can be assumed that the flow conditions in the pump are depicted correctly. Therefore, the influence on the WSS by these parameters are discussed in the following section.



**Figure 6.9:** Geometric parameters of a pump impeller. Thickness of the blade  $e$ , the inlet angle  $\beta_{1B}$  and the outlet angle  $\beta_{2B}$  (according to Gülich (2013))



**Figure 6.10:** Comparison of H-Q-curves in regard to blade number and outlet angle.

### 6.7.1 Fluid Properties

In this section, the focus is on the influence on different fluids. The standard fluid water is compared with the heavy LM LBE. According to the investigations of chapter 6.5, centrifugal pumps, which are working with water and liquid metal pumps with the same design, would have nearly the same characteristic curve. The challenge for the pump design of LM pumps is not that the behavior of the pump changes significantly with a LM as a working fluid. In fact, the challenge is that the construction materials are affected by corrosion and erosion. These physical and chemical processes can damage the pump and lead to restrictions in the pump design. The erosion potential of a moving fluid is closely linked to the WSS. Its definition was introduced in equation 3.13, and is mentioned at this point once again:

$$\tau_w = \nu \rho \frac{\partial u_x}{\partial y} \Big|_{y=0} \quad (6.9)$$

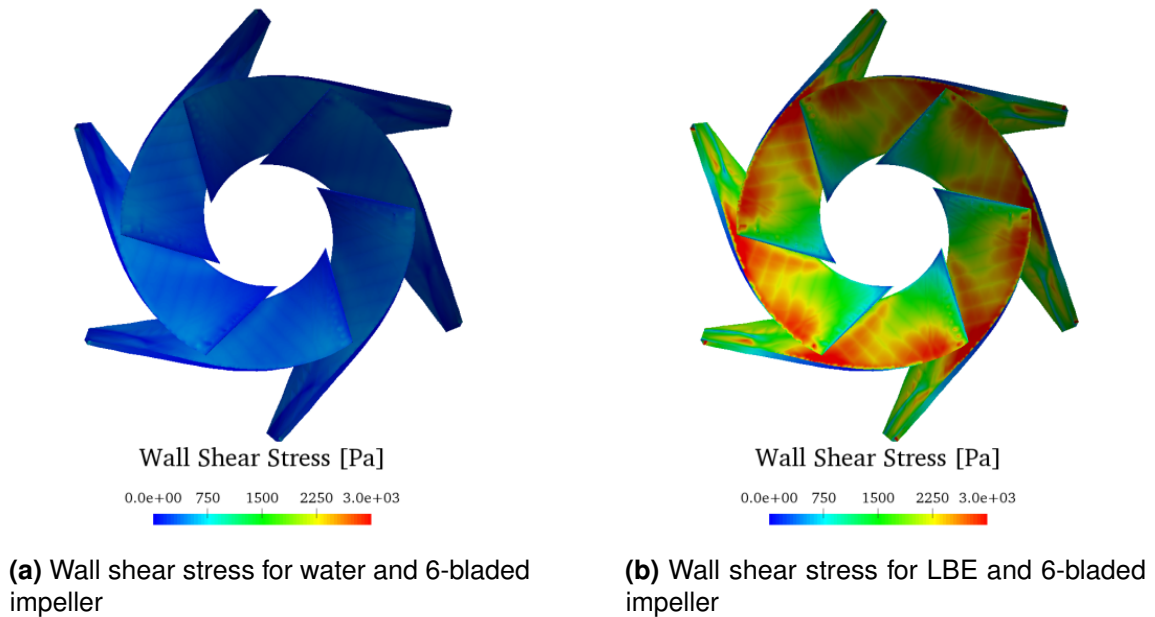
From this definition it becomes clear, that the WSS depends on the dynamic viscosity  $\nu$ , the density  $\rho$ , and the change of the flow velocity vertical to the wall. The term " $\nu \rho$ " is also known as the dynamic viscosity  $\mu$ . From the fluid properties mentioned in Table 2.2, it becomes clear that the dynamic viscosity of LBE and water are pretty close to each other. If water at 20 °C is assumed, it has a density of 998 kg/m<sup>3</sup> and a kinematic viscosity of  $10 \times 10^{-7}$  m<sup>2</sup>/s, while LBE has a density of 9960 kg/m<sup>3</sup> and a kinematic viscosity of  $1.1 \times 10^{-7}$  m<sup>2</sup>/s at 600 °C. The product of density and kinematic viscosity nearly compensate each other. Hence, water has a dynamic viscosity of 0.998 mPa s and LBE 1.09 mPa s. With nearly the same coefficient in front, the development of the WSS rely on the change of the velocity perpendicular to the wall. Figure 6.11a and 6.11b show the calculated (and post-processed) WSS distribution on a 6-bladed impeller for water and LBE. From this figure, it can be concluded that the calculated WSS for LBE is around one magnitude higher than that of water. This is qualitatively and quantitatively in good agreement with the work of Kondo et al. (2005), who investigated the erosion processes in LBE and highlighted the WSS problem for LBE. Normal construction steels and even special materials cannot withstand these forces for long. For this reason, the WSS at the blades has to be minimized as far as possible. Reducing the WSS can be done by limiting the local velocity of the flow and by design optimization. The European lead-cool reactor (ELFR), which uses a special construction material for the blades, limits the local velocity to 10 m/s for example (Alemberti, 2015). These two ways of limiting the WSS are an optimization starting point for a future work.

### 6.7.2 Influence of the Blade Number on the Wall Shear Stress

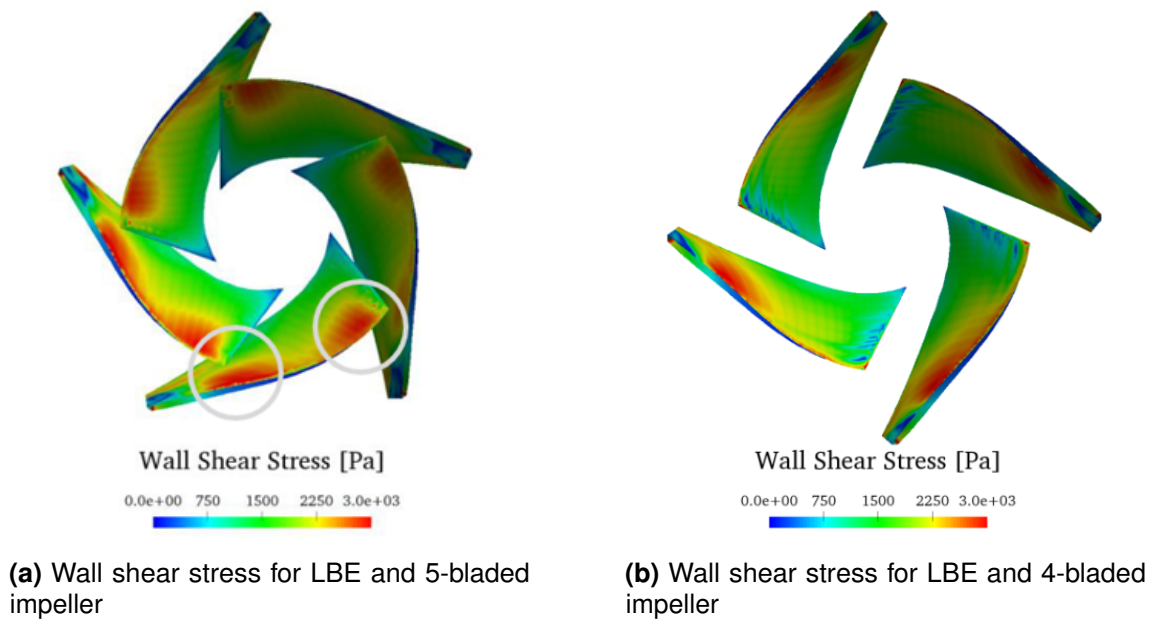
Additionally to the 5-bladed impeller, Figure 6.12a and 6.12b show the distribution for LBE with different numbers of blades but with the same flow rate  $Q_{opt}=280$  m<sup>3</sup>/h. For all images, the same color scale is used. With a closer look at the distributions, it can be already derived that for the same flow rate the impeller with six blades has larger red zones, which are an indicator for high WSS. For the different impellers,



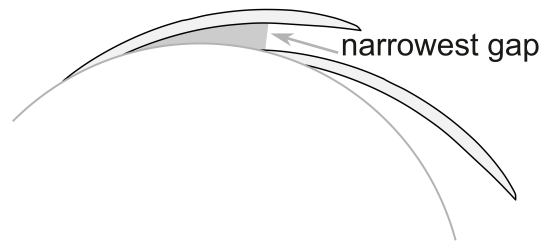
## 6. Pump Investigation in Regards of Erosion Minimization



**Figure 6.11:** Wall Shear Stress distribution of water and LBE ( $280 \text{ m}^3/\text{h}$ )



**Figure 6.12:** Wall Shear Stress distribution for a 5- and 4-bladed impeller. ( $280 \text{ m}^3/\text{h}$ )



**Figure 6.13:** Simplified depiction of two neighboring impellers (according to Gülich (2014a)).

the general patterns of the red zones are similar: one zone is located at the tip of the blade near the front shroud and one after the narrowest gap between the tip of one blade and the neighboring blade. The meant zones are highlighted in Figure 6.12a with gray circles. A simplified depiction of the geometric situation of the impeller blades can be seen in Figure 6.13. There it becomes clear where the narrowest gap between two neighboring blades is located. Due to the continuity equation, the highest velocity has to be in this gap. Naturally, this gap becomes larger for a decreasing amount of blades, and therefore, the velocity also decreases. The change of the velocity profile between two blades, due to a reduction of blades, leads to smaller and less intensive red zones for lower blade numbers at the same flow rates. To get a quantitative idea about the difference between the impellers the WSS of each blade is averaged. For comparison, the impeller with six blades is the base case. In comparison to this case, the 5-bladed impeller has to face in average 15 % less WSS and the 4-bladed 23 %. With these calculations, it can be concluded that the WSS could be reduced by lowering the blade number but, according to Figure 6.10a, at the cost of losing head, and more important, at the cost of a flatter characteristic curve.

For all different impellers, the highest WSS is calculated at the end tip of each blade.

### 6.7.3 Influence of the Outlet Angle on Wall Shear Stress

The second geometric factor covered in section 6.6 is the outlet angle. In this section, similar to the section before, the influence of the outlet angle on the WSS distribution is discussed. Figure 6.14a to 6.14c show the WSS distribution for the different outlet angles, namely 23°, 27°, and 31° degree. Figure 6.14b and 6.12a show the same impeller, a 5-bladed impeller with the default outlet angle of 27°. Here tendencies can also be derived from the figures. For small outlet angles, the areas with high WSS are much larger than for higher angles. Also, if the leading edge of the impeller is focused, it becomes clear that, for lower outlet angles, the red zone is more significant than for higher outlet angles. For the blade with an outlet angle of 31°, this area of high WSS vanishes nearly completely and only the red zone after the narrowest gap remains. To quantify this observation and get a feeling about how much lower the different WSS distributions are, the WSS per blade is averaged once again like in the section before. The result of the averaging can be seen in Figure 6.14d. The results are compared to the default case of 27°.

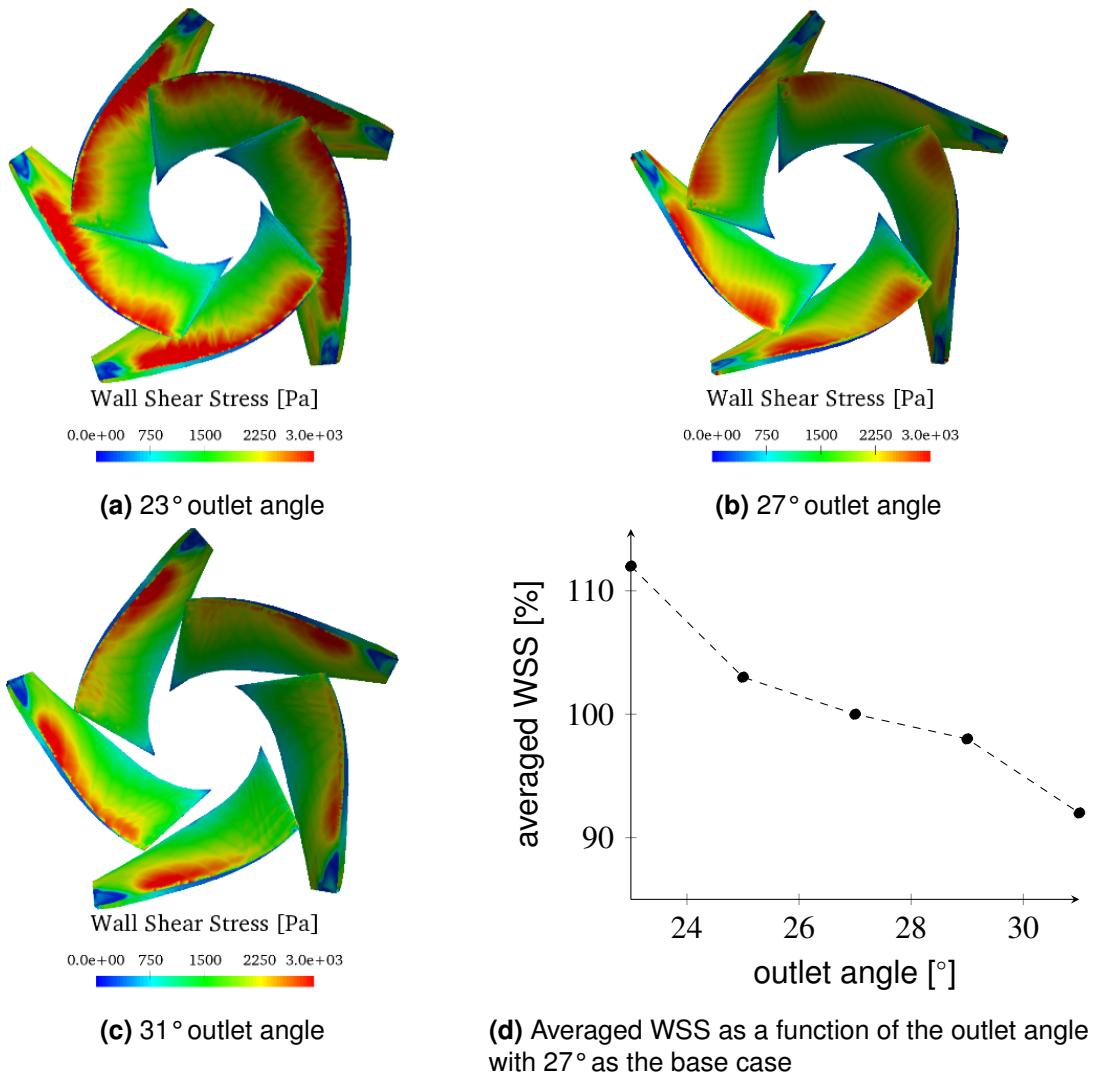


Figure 6.14: Wall shear stress distribution of different outlet angles

## ***6. Pump Investigation in Regards of Erosion Minimization***

---

Therefore, the default case is evaluated in this diagram with 100 %. In addition to the cases of 23° and 31°, which are shown in the Figure 6.14a to 6.14c, the results for 25° and 29° are also shown in this diagram. From this diagram, it becomes clear that a impeller with an 23° has to experience the highest WSS, it has to withstand around 112 % more than the base case, whereas the case with 31° has to experience 92 % WSS of this base case. It also seems that the decrease is not linear. The cases with 2° more or less, respectively, are closer to the base case than if the decrease of WSS would be linear.

# 7. Conclusion and Outlook

The focus of this study has been on the investigation of flow-driven erosion processes, namely Flow Accelerated Corrosion (FAC) and particle erosion.

The intention of this last chapter is to summarize this work, draw a conclusion, and to give a possible outlook for future works in this field.

## 7.1 Conclusion

In this study, a framework for modelling different kinds of erosion processes is presented. The fundamental idea of the framework is to combine a numerical approach with an empirical approach to predict erosion processes, and hence, to establish a method which is able to investigate the erosion progression over time. To do so, a CFD calculation is coupled with an empirical correlation, the CFD calculation provides local quantities for the correlation, and therefore, an erosion rate distribution can be calculated. This distribution of the erosion rate is then used to extrapolate the erosion in time and to deform the geometry of the computational domain in accordance with the predicted erosion. For the updated geometry, a new CFD simulation recalculates the flow conditions, and therefore, changes of the erosion behavior over time can be tracked. Self-reinforcing processes or self mitigating processes and their locations can be tracked and predicted with this timeiterative framework. Also, the framework is kept modular, therefore, the modeling can be applied to different processes, fluids and geometries.

### 7.1.1 Flow Accelerated Corrosion

First, it can be said that the so called Flow Accelerated Corrosion (FAC) process is strongly linked to the distribution of the Wall Shear Stress (WSS). Several studies can confirm that the area of high Wall Shear Stress (WSS) is in alignment with enhanced FAC. CFD studies are a powerful tool to predict the WSS distribution and give a local resolution for the WSS. This is a great addition for experimental investigations, where this information is not easily accessible. It was shown for different cases that CFD is reliably able to predict the area of high WSS. For modeling this kind of erosion process, the so called Chilton-Colburn correlation was identified as a suitable correlation with a broad application range. It can be applied for a broad range of flow conditions and also for a broad range of different

mass transfer systems. Furthermore, it uses the WSS to predict the erosion rate. Other correlations are only suitable for straight pipes or an additional geometry factor has to be added. The Chilton-Colburn correlation does not need this kind of geometry factor, due to its dependency on the WSS.

With the numerical set-up and correlation, a wall loss rate was simulated in an elbow geometry. The deformation of the geometry over time was calculated and is projected on the computational domain. A key finding of the applied framework is that it can depict changes of the erosion behavior: due to the geometry deformation, the overall erosion process is slowed down at each time step. The deformation of the geometry leads, in this case, to a mitigation of the process. The cross section of the pipe becomes larger with every time step due to the erosion. This leads to a reduction of the mean velocity, and hence, to a reduction of the mass transfer coefficient.

The investigated main case is based on an experimental set-up from the literature. The results of proposed framework were compared to the experimental results and the accompanying numerical investigations. Both theoretical investigation were able to predict the magnitude of the measured wall loss over time, but the accompanying numerical investigations showed nearly no location dependencies or time dependencies. Both dependencies can be provided by the proposed method. However, compared to the experimental measurements, qualitative discrepancies were found. These discrepancies were discussed in detail in chapter 5.1.3. Possible reasons, which could be identified, were that the experimental set-up was chosen too aggressive to speed up the erosion. In the chosen chemical regime, no protective magnetite layer could be formed. Also the pH-value was chosen in such a way, that only small variation had a huge impact on the solubility of iron. Erosion experiments are very time-consuming, therefore, set-ups are chosen which reduce the time as much as possible, but this could lead to a change of the erosion, and hence, to a misconception of the erosion under normal conditions. Erosion investigations, which were made as a byproduct of pipe failure or maintenance service, do not show these kinds of discrepancies of the qualitative behavior. In real applications, set-ups are chosen in a way that protective oxide layers can be formed and variations of the pH-value have not such an impact on the solubility.

As a second application for the framework, a Heavy Liquid Metal (HLM) set-up was chosen. For this set-up, different correlations from the literature were tested for their applicability in this framework. Due to a lack of applicability with a CFD simulation or due to a high underprediction of the erosion, none of the presented correlations were used. Therefore, the Chilton-Colburn correlation was also tested in this set-up. The correlation, together with the CFD calculation, already gave better predictions from the start than the one used in the literature. The overprediction of the Chilton-Colburn correlation at the start was 1.8. The other correlations overpredict the wall loss by a factor of 2.4. Coupled with the framework, where time dependencies can be depicted, the predicted erosion only overestimated the experimentally determined erosion rate by a factor of 1.4. Location dependencies were not relevant in this case because the investigated case was a straight pipe.

### 7.1.2 Particle erosion

Another application for the given framework is the also flow-driven process of particle erosion. There solid particles in the stream cause the wall loss due to their interaction with the construction wall. The trajectories of the particles, and hence, the impingement distribution is calculated with an Euler-Lagrangian approach. The impingement distribution can be transformed with different erosion models to an erosion rate. As before, the erosion rate can then be projected on the computational domain and the geometry is deformed.

The framework was compared to an experimental investigation found in the literature. A 90° elbow was investigated with a combination of water and sand particles. It can be said that the magnitude and location of the highest wall loss could be predicted accurately. The maximum erosion happens at the end of the bend. The general behavior of the last part of the bend was captured accurately, whereas the behavior of the first half of the bend could not be captured by the numerical investigation. An interesting key finding was that the location of the highest erosion leads to a self-reinforcing process which can be depicted by the proposed modeling framework: for the undeformed mesh, the calculated erosion rate underpredicts the wall loss at this point by a factor of 2. After the framework extrapolates the erosion, a pocket is formed at the end of the bend. This pocket enhances the erosion rate. After one day of simulated erosion time and after 34 h of experimental time, the erosion rates at this point are nearly the same with 0.12 mm/day (measured) and 0.13 mm/day (simulated).

The measured behavior of the first part of the bend is led back by the authors of the experimental investigation due to the lack of investigation time. They expected that for longer investigations this behavior would vanish.

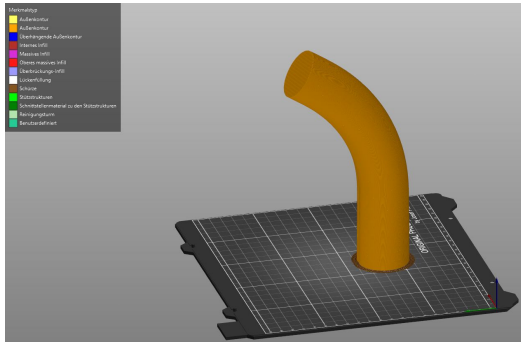
### 7.1.3 Pump Investigation

The pump investigation was done with regards to FAC minimization. A numerical pump investigation set-up was established. It was validated to a satisfying degree with experimental investigations from the literature. The focus in this section was on the behavior of centrifugal pumps with heavy liquid metals as a working fluid. For the investigation, a program was written which is able to generate the geometry of pump impellers with different parameters and properties. So, a range of different pump attributes can be tested efficiently with respect to FAC minimization.

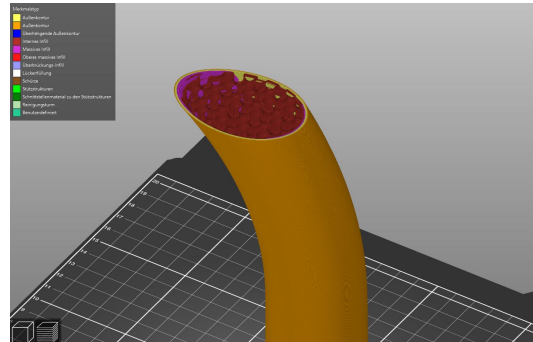
As working fluids, water and the heavy liquid metal LBE were compared. LBE has a much higher erosion potential than water. The WSS was taken as an indicator for enhanced FAC like it was shown in the previous chapters. Compared to water, the calculated WSS distribution was shifted by a factor of ten. The general pump behavior is theoretically not influenced by the different working fluids, but the high WSS demands a minimization of the erosion potential. The influence of different geometry parameters on the WSS distribution was also discussed. The parameters in question were the number of impeller blades and the outlet angle of the impeller blade. It could be shown that for higher outlet angles and fewer blades, the averaged WSS of a single blade could be reduced significantly.



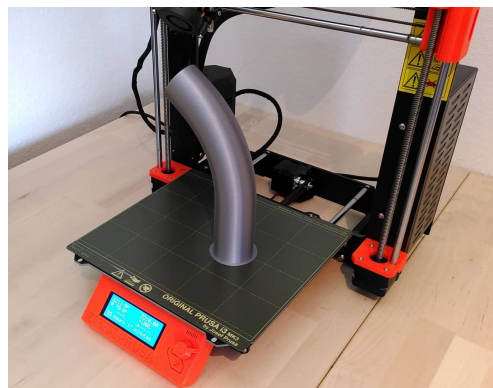
(a) Exported geometry



(b) Preview of the model and preparation for the 3D-printing



(c) Close up of the model with infill



(d) Finished 3D-printed Model

**Figure 7.1:** 3D-printed model of a deformed mesh due to erosion

A blade reduction from six to four blades could lead to a reduction of 23% and an outlet angle raise from  $27^\circ$  to  $32^\circ$  to an reduction of 8%. But this change of the geometry has to be done carefully because both arrangements lead to a flatter pump characteristic. Impellers with flatter characteristic curves have often problems with recirculation near the design points. This recirculation could also be investigated with the given numerical set-up.

The application of the proposed framework was not really possible due to the way the mesh is deformed. Only the boundary mesh points are moved and not the whole mesh, this leads to interferences of the mesh at the sharp edges or at the tips of the impellers. Therefore, only slight deformation would be allowed. With this said, this could be already a possible idea for the future work.



## **7.2 Outlook**

At this point, a possible road map for the future development of the proposed work shall be given.

- **Mesh deformation:**

In the future, the mesh deformation should be adapted. At the moment, it works well for all kinds of different elbows. For more complicated geometries like pump impellers or in general for geometries with sharp edges, the whole mesh should be deformed and not only the boundary mesh. Also, this could partially avoid the refinement problem. For this kind of deformation, a method has to be found and applied for the bulk mesh: in what kind it can be treated and deformed.

- **Team up of theoretical investigations with experimental investigations:**

During this work, it became clear that for experimental erosion investigations a lot of time is needed and that to reduce the invested time, very aggressive flow conditions and set-ups are often chosen. This problem could be reduced by combining the proposed framework with experimental investigations. A possible idea is shown in Figure 7.1. There, the deformed mesh from the simulation is exported to a 3D-printer. The idea is to print an already deformed geometry. This deformed geometry could then be a starting point for the experimental investigation. The experiments could investigate the development and behavior of the eroded geometries and less aggressive regimes could be chosen. And also, the framework could be tested further due to its prediction capabilities. In the shown figure, the fluid area was printed for better illustration. In an actual application, the negative has to be printed. Also for illustration, the print was done with a plastic material and with a private printer. The actual pipe would be printed out of metal which is also state of the art technology.



# Bibliography

- Ahlert, K. R. (1994). *Effects of particle impingement angle and surface wetting on solid particle erosion of AISI 1018 steel*. Master's thesis. Tulsa: University of Tulsa. URL: <http://www.ecrc.utulsa.edu/StudentDissertations/ECRC%20Thesis/Kevin%20R.%20Ahlert%201994.PDF> (visited on 04/01/2021).
- Alemberti, A. (2015). *ELFR - Main Systems and Components. Presentation slides of the: "Consultant's Meeting: Education Training Seminar on Fast Reactors Science and Technology"*. Ed. by Ansaldo Energia Group. ITESM Campus Santa Fe, Mexico City.
- Amy, C., D. Budenstein, M. Bagepalli, D. England, F. DeAngelis, G. Wilk, C. Jarrett, C. Kelsall, J. Hirsche, H. Wen, A. Chavan, B. Gilleland, C. Yuan, W. C. Chueh, K. H. Sandhage, Y. Kawajiri, and A. Henry (2017). "Pumping liquid metal at high temperatures up to 1,673 kelvin". eng. In: *Nature* 550.7675, pp. 199–203. DOI: [10.1038/nature24054](https://doi.org/10.1038/nature24054).
- Arabnejad, H., A. Mansouri, S. A. Shirazi, and B. S. McLaury (2015). "Development of mechanistic erosion equation for solid particles". In: *Wear* 332-333, pp. 1044–1050. DOI: [10.1016/j.wear.2015.01.031](https://doi.org/10.1016/j.wear.2015.01.031).
- Auvinen, M., H. Nilsson, D. Boger, and B. Lewis (2011). *Sig Turbomachinery Library turboPerformance*. URL: [https://openfoamwiki.net/index.php/Sig\\_Turbomachinery\\_Library\\_OpenFoamTurbo\\_turboPerformance](https://openfoamwiki.net/index.php/Sig_Turbomachinery_Library_OpenFoamTurbo_turboPerformance) (visited on 04/22/2021).
- Balbaud-Celerier, F., P. Deloffre, A. Terlain, and A. Rusanov (2002). "Corrosion of metallic materials in flowing liquid lead-bismuth". In: *Journal de Physique IV (Proceedings)* 12.8, pp. 177–190. DOI: [10.1051/jp4:20020332](https://doi.org/10.1051/jp4:20020332).
- Balbaud-Célérier, F. and F. Barbier (2001). "Investigation of models to predict the corrosion of steels in flowing liquid lead alloys". In: *Journal of Nuclear Materials* 289.3, pp. 227–242. DOI: [10.1016/S0022-3115\(01\)00431-7](https://doi.org/10.1016/S0022-3115(01)00431-7).
- Balbaud-Célérier, F. and L. Martinelli (2010). "Modeling of Fe–Cr Martensitic Steels Corrosion in Liquid Lead Alloys". In: *Journal of Engineering for Gas Turbines and Power* 132.10, pp. 102912-1–102912-9. DOI: [10.1115/1.4000865](https://doi.org/10.1115/1.4000865).
- Balbaud-Célérier, F. and A. Terlain (2004). "Influence of the Pb–Bi hydrodynamics on the corrosion of T91 martensitic steel and pure iron". In: *Journal of Nuclear Materials* 335.2, pp. 204–209. DOI: [10.1016/j.jnucmat.2004.07.009](https://doi.org/10.1016/j.jnucmat.2004.07.009).
- Becker, M. (1980). "Comparison of heat transfer fluids for use in solar thermal power stations". In: *Electric Power Systems Research* 3.3-4, pp. 139–150. DOI: [10.1016/0378-7796\(80\)90001-2](https://doi.org/10.1016/0378-7796(80)90001-2).

- Berger, F. P. and K.-F.-L. Hau (1977). "Mass transfer in turbulent pipe flow measured by the electrochemical method". In: *International Journal of Heat and Mass Transfer* 20.11, pp. 1185–1194. DOI: [10.1016/0017-9310\(77\)90127-2](https://doi.org/10.1016/0017-9310(77)90127-2).
- Bignon, M. J. (1980). "The influence of the heat transfer fluid on the receiver design". In: *Electric Power Systems Research* 3.1-2, pp. 99–109. DOI: [10.1016/0378-7796\(80\)90026-7](https://doi.org/10.1016/0378-7796(80)90026-7).
- Borreani, W., A. Alemberti, G. Lomonaco, F. Magugliani, and P. Saracco (2017). "Design and Selection of Innovative Primary Circulation Pumps for GEN-IV Lead Fast Reactors". In: *Energies* 10.12, p. 2079. DOI: [10.3390/en10122079](https://doi.org/10.3390/en10122079).
- Brauer, H. (1971). *Grundlagen der Einphasen- und Mehrphasenströmungen*. Grundlagen der chemischen Technik. Aarau u. Frankfurt/M.: Sauerländer. URL: <https://books.google.de/books?id=0phTAAAYAAJ>.
- Caretto, L. S., A. D. Gosman, S. V. Patankar, and D. B. Spalding (1973). "Two calculation procedures for steady, three-dimensional flows with recirculation". In: *Proceedings of the Third International Conference on Numerical Methods in Fluid Mechanics*. Ed. by H. Cabannes and R. Temam. Vol. 19. Lecture Notes in Physics. Berlin, Heidelberg: Springer Berlin Heidelberg, pp. 60–68. DOI: [10.1007/BFb0112677](https://doi.org/10.1007/BFb0112677).
- Chen, T. Y., A. A. Moccari, and D. D. Macdonald (1992). "Development of Controlled Hydrodynamic Techniques for Corrosion Testing". In: *CORROSION* 48.3, pp. 239–255. DOI: [10.5006/1.3315930](https://doi.org/10.5006/1.3315930).
- Chilton, T. H. and A. P. Colburn (1934). "Mass Transfer (Absorption) Coefficients Prediction from Data on Heat Transfer and Fluid Friction". In: *Industrial & Engineering Chemistry* 26.11, pp. 1183–1187. DOI: [10.1021/ie50299a012](https://doi.org/10.1021/ie50299a012).
- Constien, M. (2018). "Numerische Untersuchung des Einflusses verschiedener Flüssigmetalle auf die Charakteristik von Kreiselpumpen". Supervisor: Cheng, X.; Co-supervisor: Schenk, M.; Master Thesis. Germany: Karlsruher Institut für Technologie.
- Einstein, A. (1905). "Über die von der molekularkinetischen Theorie der Wärme geforderte Bewegung von in ruhenden Flüssigkeiten suspendierten Teilchen". In: *Annalen der Physik* 322.8, pp. 549–560. DOI: [10.1002/andp.19053220806](https://doi.org/10.1002/andp.19053220806).
- Fazio, C. et al. (2015). *Handbook on Lead-bismuth Eutectic Alloy and Lead Properties, Materials Compatibility, Thermal-hydraulics and Technologies - 2015 Edition*. Tech. rep. Nuclear Energy Agency of the OECD (NEA).
- Forder, A., M. Thew, and D. Harrison (1998). "A numerical investigation of solid particle erosion experienced within oilfield control valves". In: *Wear* 216.2, pp. 184–193. DOI: [10.1016/S0043-1648\(97\)00217-2](https://doi.org/10.1016/S0043-1648(97)00217-2).
- Fraser, W. H. (1981). *Flow Recirculation In Centrifugal Pumps*. Texas A&M University. Turbomachinery Laboratories, pp. 95–100. DOI: [10.21423/R1WH41](https://doi.org/10.21423/R1WH41).
- Fritsch, A., J. Flesch, V. Geza, C. Singer, R. Uhlig, and B. Hoffschmidt (2015). "Conceptual Study of Central Receiver Systems with Liquid Metals as Efficient Heat Transfer Fluids". In: *Energy Procedia* 69, pp. 644–653. DOI: [10.1016/j.egypro.2015.03.074](https://doi.org/10.1016/j.egypro.2015.03.074).
- Fujiwara, K., M. Domae, K. Yoneda, F. Inada, T. Ohira, and K. Hisamune (2011). "Correlation of flow accelerated corrosion rate with iron solubility". In: *Nuclear*

- Engineering and Design* 241.11, pp. 4482–4486. DOI: [10.1016/j.nucengdes.2011.04.035](https://doi.org/10.1016/j.nucengdes.2011.04.035).
- Gesellschaft für Tribologie e.V., ed. (2002). *Arbeitsblatt 7 – Tribologie*. URL: <https://www.gft-ev.de/de/arbeitsblaetter/> (visited on 09/01/2020).
- Gokcen, N. (1992). “The Bi-Pb (bismuth-lead) System”. In: *Journal of Phase Equilibria* 13.1, pp. 21–32. DOI: [10.1007/BF02645372](https://doi.org/10.1007/BF02645372).
- Grant, G. and W. Tabakoff (1975). “Erosion Prediction in Turbomachinery Resulting from Environmental Solid Particles”. In: *Journal of Aircraft* 12.5, pp. 471–478. DOI: [10.2514/3.59826](https://doi.org/10.2514/3.59826).
- Gülich, J. F. (2013). “Allgemeine strömungstechnische Grundlagen”. In: *Kreiselpumpen*. Ed. by J. F. Gülich. Berlin, Heidelberg: Springer Berlin Heidelberg, pp. 1–42. DOI: [10.1007/978-3-642-40032-2\\_1](https://doi.org/10.1007/978-3-642-40032-2_1).
- ed. (2014a). *Centrifugal Pumps*. Berlin, Heidelberg: Springer Berlin Heidelberg. DOI: [10.1007/978-3-642-40114-5](https://doi.org/10.1007/978-3-642-40114-5).
- (2014b). “Performance Characteristics”. In: *Centrifugal Pumps*. Ed. by J. F. Gülich. Berlin, Heidelberg: Springer Berlin Heidelberg, pp. 159–203. DOI: [10.1007/978-3-642-40114-5\\_4](https://doi.org/10.1007/978-3-642-40114-5_4).
- (2014c). “Pump Types and Performance Data”. In: *Centrifugal Pumps*. Ed. by J. F. Gülich. Berlin, Heidelberg: Springer Berlin Heidelberg, pp. 43–78. DOI: [10.1007/978-3-642-40114-5\\_2](https://doi.org/10.1007/978-3-642-40114-5_2).
- Harriott, P. and R. M. Hamilton (1965). “Solid-liquid mass transfer in turbulent pipe flow”. In: *Chemical Engineering Science* 20.12, pp. 1073–1078. DOI: [10.1016/0009-2509\(65\)80110-5](https://doi.org/10.1016/0009-2509(65)80110-5).
- Hewitt, G. F., G. L. Shires, and T. R. Bott (1994). *Process heat transfer*. Boca Raton: CRC Press. 1042 pp.
- Holser, R. A., G. Prentice, R. B. Pond, and R. Guanti (1990). “Use of Rotating Cylinder Electrodes to Simulate Turbulent Flow Conditions in Corroding Systems”. In: *CORROSION* 46.9, pp. 764–769. DOI: [10.5006/1.3585179](https://doi.org/10.5006/1.3585179).
- Huber, M., A. Harvey, E. Lemmon, G. Hardin, I. Bell, and M. McLinden (2018). *NIST Reference Fluid Thermodynamic and Transport Properties Database (REFPROP) Version 10 - SRD 23*. Gaithersburg: National Institute of Standards and Technology. DOI: [10.18434/T4/1502528](https://doi.org/10.18434/T4/1502528).
- Jordan, E. (1986). *Information Notice No. 86-106: Feedwater Line Break*. Washington: United States Nuclear Regulatory Commission Office of Inspection and Enforcement. URL: <https://www.nrc.gov/reading-rm/doc-collections/gen-comm/info-notices/1986/in86106.html> (visited on 04/01/2021).
- (1987). *Information Notice No. 86-106, Supplement 1: Feedwater Line Break*. Washington: United States Nuclear Regulatory Commission Office of Inspection and Enforcement. URL: <https://www.nrc.gov/reading-rm/doc-collections/gen-comm/info-notices/1986/in86106s1.html> (visited on 03/01/2021).
- Kain, V. (2014). “Flow Accelerated Corrosion: Forms, Mechanisms and Case Studies”. In: *Procedia Engineering* 86, pp. 576–588. DOI: [10.1016/j.proeng.2014.11.083](https://doi.org/10.1016/j.proeng.2014.11.083).

- Kain, V., S. Roychowdhury, P. Ahmedabadi, and D. K. Barua (2011). "Flow accelerated corrosion: Experience from examination of components from nuclear power plants". In: *Engineering Failure Analysis* 18.8, pp. 2028–2041. DOI: [10.1016/j.engfailanal.2011.06.007](https://doi.org/10.1016/j.engfailanal.2011.06.007).
- Kain, V., S. Roychowdhury, T. Mathew, and A. Bhandakkar (2008). "Flow accelerated corrosion and its control measures for the secondary circuit pipelines in Indian nuclear power plants". In: *Journal of Nuclear Materials* 383.1-2, pp. 86–91. DOI: [10.1016/j.jnucmat.2008.08.024](https://doi.org/10.1016/j.jnucmat.2008.08.024).
- Kang, D.-G. and J.-C. Jo (2008). "CFD Application To The Regulatory Assessment Of FAC-caused CANDU Feeder Pipe Wall Thinning Issue". In: *Nuclear Engineering and Technology* 40.1, pp. 37–48. DOI: [10.5516/NET.2008.40.1.037](https://doi.org/10.5516/NET.2008.40.1.037).
- Kelly, J. E. (2014). "Generation IV International Forum: A decade of progress through international cooperation". In: *Progress in Nuclear Energy* 77, pp. 240–246. DOI: [10.1016/j.pnucene.2014.02.010](https://doi.org/10.1016/j.pnucene.2014.02.010).
- Keshtkar, K., M. Nematollahi, and A. Erfaninia (2016). "CFX study of flow accelerated corrosion via mass transfer coefficient calculation in a double elbow". In: *International Journal of Hydrogen Energy* 41.17, pp. 7036–7046. DOI: [10.1016/j.ijhydene.2016.02.072](https://doi.org/10.1016/j.ijhydene.2016.02.072).
- Kikuchi, K., Y. Kurata, S. Saito, M. Futakawa, T. Sasa, H. Oigawa, E. Wakai, and K. Miura (2003). "Corrosion–erosion test of SS316 in flowing Pb–Bi". In: *Journal of Nuclear Materials* 318, pp. 348–354. DOI: [10.1016/S0022-3115\(03\)00017-5](https://doi.org/10.1016/S0022-3115(03)00017-5).
- Kleuker, H.-H., A. Laurenzis, W. Althaus, A. Steiff, and P.-M. Weinspach (1993). "Hydrodynamische Einlauflänge und Widerstandsgesetz von reibungsmindernden kationschen Tensidlösungen". In: *Forschung im Ingenieurwesen* 59.1-2, pp. 8–18. DOI: [10.1007/BF02560619](https://doi.org/10.1007/BF02560619).
- Kondo, M., M. Takahashi, T. Suzuki, K. Ishikawa, K. Hata, S. Qiu, and H. Sekimoto (2005). "Metallurgical study on erosion and corrosion behaviors of steels exposed to liquid lead–bismuth flow". In: *Journal of Nuclear Materials* 343.1-3, pp. 349–359. DOI: [10.1016/j.jnucmat.2004.08.037](https://doi.org/10.1016/j.jnucmat.2004.08.037).
- KSB SE & Co. KGaA, ed. (2019). *KSB Know-how. Auslegung von Kreiselpumpen*. Frankenthal. URL: <https://www.ksb.com/blob/52816/9af836d03845863bab17871e1357c8e9/auslegung-de-data.pdf> (visited on 04/01/2021).
- Levy, A. V. (1995). *Solid particle erosion and erosion-corrosion of materials*. eng. 1. print. Materials Park, Ohio: ASM International. 220 pp.
- Lide, D. R. and H. V. Kehiaian (1994). *CRC handbook of thermophysical and thermochemical data*. eng. Boca Raton: CRC Press. 518 pp. URL: <http://www.loc.gov/catdir/enhancements/fy0744/93036909-d.html>.
- Lomonaco, G., W. Borreani, F. Magugliani, and A. Alemberti (2016). *Theoretical and numerical investigation of three designs for a primary circulation pump evolving liquid lead for Gen-IV reactors. Conference: Innovative Designs and Technologies of Nuclear Power - IV International Scientific and Technical Conference*. Moscow. URL: [https://www.researchgate.net/publication/309488613\\_THEORETICAL\\_AND\\_NUMERICAL\\_INVESTIGATION\\_OF](https://www.researchgate.net/publication/309488613_THEORETICAL_AND_NUMERICAL_INVESTIGATION_OF)

- THREE\_DESIGNS\_FOR\_A\_PRIMARY\_CIRCULATION\_PUMP\_EVOLVING\_LIQUID\_LEAD\_FOR\_GEN-IV\_REACTORS (visited on 03/01/2021).
- Lorenzin, N. and A. Abánades (2016). “A review on the application of liquid metals as heat transfer fluid in Concentrated Solar Power technologies”. In: *International Journal of Hydrogen Energy* 41.17, pp. 6990–6995. DOI: [10.1016/j.ijhydene.2016.01.030](https://doi.org/10.1016/j.ijhydene.2016.01.030).
- Ma, X. D., X. L. Li, Z. Q. Zhu, C. J. Li, and S. Gao (2016). “The stress analysis of a heavy liquid metal pump impeller”. In: *IOP Conference Series: Materials Science and Engineering* 129, p. 012023. DOI: [10.1088/1757-899X/129/1/012023](https://doi.org/10.1088/1757-899X/129/1/012023).
- Madasamy, P., T. V. Krishna Mohan, A. Sylvanus, E. Natarajan, H. P. Rani, and S. Velmurugan (2018). “Hydrodynamic effects on flow accelerated corrosion at 120 °C and neutral pH conditions”. In: *Engineering Failure Analysis* 94, pp. 458–468. DOI: [10.1016/j.engfailanal.2018.08.021](https://doi.org/10.1016/j.engfailanal.2018.08.021).
- Menter, F. (n.d.). “Zonal Two Equation k-w Turbulence Models For Aerodynamic Flows”. In: *24th Fluid Dynamics Conference*. Orlando. DOI: [10.2514/6.1993-2906](https://doi.org/10.2514/6.1993-2906).
- Müller, T., P. Limbach, and R. Skoda (2015). “Numerical 3D RANS simulation of gas-liquid flow in a centrifugal pump with an Euler-Euler two-phase model and a dispersed phase distribution”. In: *11th European Conference on Turbomachinery Fluid dynamics & Thermodynamics*.
- Nikuradse, J. (1932). *Gesetzmäßigkeiten der turbulenten Strömung in glatten Rohren. Forschungsheft ; 356*. Berlin: VDI-Verl. URL: [http://slubdd.de/katalog?TN\\_libero\\_mab214186329%20ER%20-](http://slubdd.de/katalog?TN_libero_mab214186329%20ER%20-).
- Pacio, J. and T. Wetzel (2013). “Assessment of liquid metal technology status and research paths for their use as efficient heat transfer fluids in solar central receiver systems”. In: *Solar Energy* 93, pp. 11–22. DOI: [10.1016/j.solener.2013.03.025](https://doi.org/10.1016/j.solener.2013.03.025).
- Petukhov, B. S. (1970). “Heat Transfer and Friction in Turbulent Pipe Flow with Variable Physical Properties”. In: vol. 6. *Advances in Heat Transfer*. Elsevier, pp. 503–564. DOI: [10.1016/S0065-2717\(08\)70153-9](https://doi.org/10.1016/S0065-2717(08)70153-9).
- Pfleiderer, C. (1961). *Die Kreiselpumpen für Flüssigkeiten und Gase*. Berlin, Heidelberg: Springer Berlin Heidelberg. DOI: [10.1007/978-3-642-48170-3](https://doi.org/10.1007/978-3-642-48170-3).
- Pietralik, J. (2012). “The role of flow in flow accelerated corrosion under nuclear power plant conditions”. In: *E-Journal of Advanced Maintenance* 4. 01, pp. 63–78.
- Pinto, R. N., A. Afzal, L. V. D’Souza, Z. Ansari, and A. D. Mohammed Samee (2017). “Computational Fluid Dynamics in Turbomachinery: A Review of State of the Art”. In: *Archives of Computational Methods in Engineering* 24.3, pp. 467–479. DOI: [10.1007/s11831-016-9175-2](https://doi.org/10.1007/s11831-016-9175-2).
- Pourbaix, M. (1966). *Atlas of electrochemical equilibria in aqueous solutions*. Oxford [u.a.]: Pergamon Press [u.a.]
- Prasad, M., V. Gopika, A. Sridharan, and S. Parida (2018). “Pipe wall thickness prediction with CFD based mass transfer coefficient and degradation feedback for flow accelerated corrosion”. In: *Progress in Nuclear Energy* 107, pp. 205–214. DOI: [10.1016/j.pnucene.2018.04.024](https://doi.org/10.1016/j.pnucene.2018.04.024).



- Projectmaterials (2017). *Carbon Steel Pipe A53/A106 Gr. B, A333 Gr. 6*. URL: <https://blog.projectmaterials.com/pipes/carbon-pipe-a53-a106-a333/> (visited on 04/11/2020).
- Rani, H. P., T. Divya, R. R. Sahaya, V. Kain, and D. K. Barua (2014). "CFD study of flow accelerated corrosion in 3D elbows". In: *Annals of Nuclear Energy* 69, pp. 344–351. DOI: [10.1016/j.anucene.2014.01.031](https://doi.org/10.1016/j.anucene.2014.01.031).
- Sadegh, A. M. (2018). *Marks' standard handbook for mechanical engineers*. 12th edition. McGraw-Hill's AccessEngineering. New York: McGraw-Hill.
- Schenk, M. and X. Cheng (2018c). "CFD Analysis of centrifugal Liquid Metal Pumps". In: *49. Jahrestagung Kerntechnik / 49th Annual Meeting on Nuclear Technology (AMNT 2018) (Conference), Berlin, May 29-30, 2018*. INFORUM Verlags- und Verwaltungsgesellschaft mbH, CD-ROM.
- Sedrez, T. A., S. A. Shirazi, Y. R. Rajkumar, K. Sambath, and H. J. Subramani (2019). "Experiments and CFD simulations of erosion of a 90° elbow in liquid-dominated liquid-solid and dispersed-bubble-solid flows". In: *Wear* 426-427, pp. 570–580. DOI: [10.1016/j.wear.2019.01.015](https://doi.org/10.1016/j.wear.2019.01.015).
- Sig Turbomachinery (2009). *See the MRF development*. URL: [https://openfoamwiki.net/index.php/See\\_the\\_MRF\\_development](https://openfoamwiki.net/index.php/See_the_MRF_development) (visited on 02/12/2021).
- Silverman, D. C. (1984). "Rotating Cylinder Electrode for Velocity Sensitivity Testing". In: *CORROSION* 40.5, pp. 220–226. DOI: [10.5006/1.3581945](https://doi.org/10.5006/1.3581945).
- Slade, J. P. and T. S. Gendron (2005). "Flow Accelerated Corrosion and Cracking of Carbon Steel Piping in Primary Water-Operating Experience at the Point Lepreau Generating Station". In: *Proceedings of the 12th International Conference on Environmental Degradation of Materials in Nuclear Systems*. Salt Lake City, pp. 773–782.
- Sobolev, V. P. (2011). *Database of Thermophysical Properties of Liquid Metal Coolants for GEN-IV. Sodium, lead, lead-bismuth eutectic (and bismuth)*. Ed. by SCKCEN - Belgian Nuclear Research Centre. Mol, Belgium.
- Sommer, K., R. Heinz, and J. Schöfer (2010). *Verschleiß metallischer Werkstoffe. Erscheinungsformen sicher beurteilen*. ger. Wiesbaden: Vieweg+Teubner Verlag / Springer Fachmedien Wiesbaden GmbH Wiesbaden. DOI: [10.1007/978-3-8348-9775-6](https://doi.org/10.1007/978-3-8348-9775-6).
- Stepanoff, A. J., ed. (1957a). *Radial- und Axialpumpen*. Berlin, Heidelberg: Springer Berlin Heidelberg. DOI: [10.1007/978-3-662-25101-0](https://doi.org/10.1007/978-3-662-25101-0).
- (1957b). "Spezifische Drehzahl und Entwurfskenngrößen". In: *Radial- und Axialpumpen*. Ed. by A. J. Stepanoff. Berlin, Heidelberg: Springer Berlin Heidelberg, pp. 53–70. DOI: [10.1007/978-3-662-25101-0\\_5](https://doi.org/10.1007/978-3-662-25101-0_5).
- Suryawijaya, P. and G. Kosyna (2000). "Schaufeldruckmessungen im rotierenden System an einer Radialpumpe bei Gas/Flüssigkeitsgemischförderung". In: *Chemie Ingenieur Technik* 72.11, pp. 1366–1371. DOI: [10.1002/1522-2640\(200011\)72:11<1366::AID-CITE1366>3.0.CO;2-E](https://doi.org/10.1002/1522-2640(200011)72:11<1366::AID-CITE1366>3.0.CO;2-E).
- Sweeton, F. and C. Baes (1970). "The solubility of magnetite and hydrolysis of ferrous ion in aqueous solutions at elevated temperatures". In: *The Journal of Chemical Thermodynamics* 2.4. PII: 0021961470900984, pp. 479–500. DOI: [10.1016/0021-9614\(70\)90098-4](https://doi.org/10.1016/0021-9614(70)90098-4).



- U.S. Nuclear Energy Research Advisory Committee (NERAC) and the Generation IV International Forum (GIF) (2002). *A Technology Roadmap for Generation IV Nuclear Energy Systems*. Tech. rep. Technical Roadmap Report (pp. 1 - 163).
- Uhlig, H. H. and R. W. Revie, eds. (2000). *Uhlig's corrosion handbook. Chapter 6*. eng. 2. ed. Electrochemical Society series. New York, NY: Wiley. 1302 pp.
- VDI-Wärmeatlas* (2013). 11., bearb. und erw. Aufl. Berlin: Springer Vieweg.
- Wesche, W. (2016a). "Grundlagen für die Berechnung und Konstruktion der hydrodynamischen Komponenten". In: *Radiale Kreiselpumpen*. Ed. by W. Wesche. Berlin, Heidelberg: Springer Berlin Heidelberg, pp. 63–278. DOI: [10.1007/978-3-662-48912-3\\_3](https://doi.org/10.1007/978-3-662-48912-3_3).
- (2016b). *Radiale Kreiselpumpen*. Berlin, Heidelberg: Springer Berlin Heidelberg. DOI: [10.1007/978-3-662-48912-3](https://doi.org/10.1007/978-3-662-48912-3).
- Wilcox, D. C. (1993). *Turbulence modeling for CFD*. eng. La Cañada, Calif.: DCW Industries Inc.
- Wilke, C. R. and P. Chang (1955). "Correlation of diffusion coefficients in dilute solutions". In: *American Institute of Chemical Engineers* 1.2, pp. 264–270. DOI: [10.1002/aic.690010222](https://doi.org/10.1002/aic.690010222).
- Zhang, J. and N. Li (2008). "Review of the studies on fundamental issues in LBE corrosion". In: *Journal of Nuclear Materials* 373.1-3, pp. 351–377. DOI: [10.1016/j.jnucmat.2007.06.019](https://doi.org/10.1016/j.jnucmat.2007.06.019).
- Zhexin, F. (2018). "Einfluss des Gasanteils auf die Pumpencharakteristik von Flüssigmetall-Pumpen". Supervisor: Cheng, X.; Co-supervisor: Schenk, M. ; Master Thesis. Germany: Karlsruher Institut für Technologie.



# Own Publications-Conferences

- Schenk, M. and X. Cheng (2018a). "CFD Analysis of Wall Shear Stress and Recirculation in Centrifugal Liquid Metal Pumps". In: *12th International Topical Meeting on Reactor Thermal-Hydraulics, Operation, and Safety (NUTHOS-12) (Conference), Qingdao, China.*
- Schenk, M. and X. Cheng (2018b). "CFD Analysis of Liquid Metal Pumps". In: *German CFD Meeting (Conference), Munich, Germany.*
- Schenk, M. and X. Cheng (2018c). "CFD Analysis of centrifugal Liquid Metal Pumps". In: *49. Jahrestagung Kerntechnik / 49th Annual Meeting on Nuclear Technology (AMNT 2018) (Conference), Berlin, May 29-30, 2018.* INFORUM Verlags- und Verwaltungsgesellschaft mbH, CD-ROM.



# Supervised Theses

- Constien, M. (2018). "Numerische Untersuchung des Einflusses verschiedener Flüssigmetalle auf die Charakteristik von Kreiselpumpen". Supervisor: Cheng, X.; Co-supervisor: Schenk, M. ; Master Thesis. Germany: Karlsruher Institut für Technologie.
- Zhexin, F. (2018). "Einfluss des Gasanteils auf die Pumpencharakteristik von Flüssigmetall-Pumpen". Supervisor: Cheng, X.; Co-supervisor: Schenk, M. ; Master Thesis. Germany: Karlsruher Institut für Technologie.